

# Laser Flash Photolysis and EPR Spectroscopy Investigations of Bare and Lanthanum Doped NaTaO<sub>3</sub> Powders

Der Naturwissenschaftlichen Fakultät der Gottfried Wilhelm Leibniz  
Universität Hannover

zur Erlangung des Grades

Doktorin der Naturwissenschaften

Dr.rer.nat.

genehmigte Dissertation von

Maria del Pilar Esteban Mollá, Licenciada en Química (Spanien)

geboren am 08.02.1985 in Valencia (Spanien)

2016

Referent: Prof. Dr. rer. nat. Detlef W. Bahnemann

Korreferent: Prof. Dr. rer. nat. Thomas Scheper

Tag der Promotion: 15. Dezember 2016

A mi hijo Alexander...

*"Yes, my friends, I believe that water will one day be employed as fuel, that hydrogen and oxygen which constitute it will furnish an inexhaustible source of heat and light. Water will be the coal of our future".*

Jules Verne, *The Mysterious Island* (1874)

## Acknowledgements

At this point I would like to thank all the people that have helped and supported me during my PhD and made in some way this thesis possible.

First I would like to express my deepest gratitude to Prof. Dr. Detlef Bahnemann for the incredible opportunity to work under his supervision in such an interesting field, for his valuable guidance and inspiring reviews.

I thank Prof. Dr. Thomas Scheper for very kindly accepting me as a PhD student in the Institute of Technical Chemistry.

Thanks to Dr. Nadja Bigall for kindly accepting the position as my third examiner.

My sincere thanks to Dr. Ralph Dillert for the numerous stimulating and interesting scientific discussions and help during the writing process.

I would like to thank Dr. Tarek Kandiel for the supervision at the early stages of my work. My sincere thanks to all the members of Prof. Bahnemann's work group for their assistance in laboratory related issues, for the good atmosphere at work and for the good times at conferences.

Special thanks to Ana, Irina, Jenny, Maryam and Faycal for the always funny times at the Mensa.

A huge thanks to Ana T. Blanco for helping me and for becoming a friend from the very beginning.

For the financial support in the Project called „Neue Katalysatoren und Technologien für die solar-chemische Wasserstoffherzeugung“ („Hycats“), I thank the Bundesministerium für Forschung und Bildung (BMBF).

Lastly I would like to express my gratitude to my family, who have always helped me during my studies in Spain and the PhD in Germany and for always being there at all times.

Special thanks to my husband Mathias who has always believed in me no matter what. For his unconditional support, motivation and encouragement in all aspects of my life.

To my son Alexander, for giving sense to all what I do and for being the ultimate reason for finishing this project.

## Kurzzusammenfassung

Um beunruhigende Energie- und Umweltprobleme der heutigen Zeit angehen zu können, werden höchst effiziente Systeme zur Umwandlung und Speicherung von Sonnenenergie benötigt. Ein solches stellt die photokatalytische Spaltung von Wasser in Wasserstoff und Sauerstoff mithilfe von Sonnenlicht dar. Als Katalysatoren für die dabei ablaufenden Prozesse werden halbleitende Metalloxide benutzt. Die zukünftige Herstellung solcher Photokatalysatoren erfordert ein tiefes Verständnis der zugrundeliegenden Mechanismen. Ein Ziel dieser Arbeit war es daher, die photodynamischen Prozesse von  $\text{NaTaO}_3$  mithilfe von Laser-Blitz-Photolyse-Experimenten und EPR Spektroskopie zu untersuchen. Das Material wurde chemisch und physikalisch charakterisiert, um die Energieniveaus des Leitungs- und Valenzbandes zu bestimmen. Der Einfluss einer Dotierung mit Lanthan auf deren Position wurde mithilfe elektrochemischer Messungen untersucht. Hierbei wurde eine photoelektrische Zelle mit einer Drei-Elektroden-Konfiguration verwendet. Die Präparierung der Arbeitselektroden mit  $\text{NaTaO}_3$  wird beschrieben.

Bei den Laser-Blitz-Photolyse-Experimenten zeigten sich Signale, welche charakterisiert werden mussten. Hierzu wurden Experimente mit verschiedenen Elektronen- und Löcherfängern durchgeführt. Als Elektronenfänger dienten Luft, reiner Sauerstoff und Platin, als Löcherfänger verschiedene Alkohole. Alle Untersuchungen wurden sowohl für undotiertes  $\text{NaTaO}_3$  als auch für unterschiedlich starke Dotierungen mit Lanthan (0.57, 0.83 und 1.11 wt. % La) durchgeführt.

Bei Bestrahlung mit einer Wellenlänge, die ausreichend zur Überwindung der Bandlücke bei 248 nm ist, konnte ein Signal bei 310 nm gemessen werden. Um die Ursachen dieses Signals zu untersuchen, wurde eine Reihe von Experimenten durchgeführt, bei denen die Proben mit einer Wellenlänge unterhalb der Bandlücke bei 351 nm bestrahlt wurden. Dabei zeigten sich im Vergleich zu den vorherigen Messungen um den Faktor zehn schwächere Signale.

Aus den Experimenten kann geschlossen werden, dass die Bestrahlung mit der Wellenlänge 248 nm photogenerierte Löcher erzeugte, die Bestrahlung mit der Wellenlänge 351 nm hingegen zur Bildung photogenerierter Elektronen führte. Diese Schlussfolgerungen werden von den durchgeführten EPR-Messungen gestützt, bei denen ebenfalls  $\text{Ta}^{\text{IV}}$  beobachtet wurde.

Die  $\text{H}_2$ -Bildung unter Bestrahlung bei 350 nm wurde gemessen, um die Quantenausbeute bestimmen zu können (0.97%).

**Stichwörter:** Natriumtantalat, Photokatalyse, Laser Blitz Photolyse, getrappe Ladungsträger, EPR.

## Abstract

In order to solve the most concerning global energy and environmental issues, highly efficient systems for solar energy conversion and storage are needed. One of them is the photocatalytic conversion of solar energy into molecular hydrogen and oxygen in a process called water splitting. For this purpose, metal oxide semiconductors are used as catalysts for this process.

In order to design and develop efficient photocatalysts that can split water, a deep understanding of the mechanistical aspects is required. In this thesis, the photodynamics of NaTaO<sub>3</sub> have been investigated by means of laser flash photolysis and EPR spectroscopy. Some characterization of the material has been performed as well in order to establish the energetic positions of the conduction and valence bands.

The influence of the lanthanum doping on the conduction band position was evaluated by means of flatband potential measurements. A photoelectrochemical cell was employed with a three-electrode configuration. The preparation of the working electrodes with NaTaO<sub>3</sub> is explained as well.

The laser flash photolysis measurements and the EPR spectroscopy delivered some signals that needed to be characterized. For that purpose, experiments using different electron and hole scavengers were carried out. As electron scavengers, air, O<sub>2</sub>, and Pt were used whilst different alcohols were employed as hole scavengers. All investigations were performed for undoped NaTaO<sub>3</sub> and for the material with different lanthanum dopings (0.57, 0.83 and 1.11 wt.% of La).

When the material was irradiated with a band gap excitation wavelength of 248 nm a signal at 310 nm was measured. In order to evaluate the nature of that signal, a series of experiments were performed with a sub-band gap irradiation wavelength of 351 nm, which delivered signals ten times lower in intensity.

From the experiments it can be concluded that the signal observed with the 248 nm irradiation belongs to the photogenerated holes and when the 351 nm wavelength was used, signals belonging to the photogenerated electrons can be measured.

These observations correlate with the performed EPR measurements where Ta<sup>IV</sup> species could be detected as well.

The formation of molecular hydrogen using 350 nm was measured in order to calculate the quantum yield (0.97%).

**Keywords:** sodium tantalate, photocatalysis, laser flash photolysis, trapped charge carriers, EPR.

# Contents

<b>1.</b>	<b>Introduction and aim of the work.....</b>	<b>1</b>
1.1	General background.....	1
1.2	Photoelectrochemical Water Splitting .....	2
1.2.1	Photoelectrochemical Cells .....	2
1.2.2	Photocatalytic Systems .....	4
1.3	Objectives .....	6
<b>2.</b>	<b>Theoretical background .....</b>	<b>9</b>
2.1	Band bending and formation of Schottky barriers.....	9
2.2	Photoelectrochemical water splitting .....	15
2.3	Photocatalytic water splitting.....	17
2.4	Photocatalyst surface modification .....	18
2.5	Laser flash photolysis.....	18
2.5.1	Dynamics of charge carrier trapping and recombination.....	19
2.5.2	Trapped and free charge carriers in semiconductor particles.....	20
2.5.2.1	Hole trapping.....	21
2.5.2.2	Electron trapping.....	24
2.5.3	Photoinduced electron transfer processes .....	25
2.5.3.1	Photoinduced reduction reactions .....	26
2.5.3.2	Photoinduced oxidation reactions .....	26
2.5.4	Laser flash photolysis studies on tantalates.....	27
2.6	Electron paramagnetic resonance (EPR) .....	32
<b>3.</b>	<b>Materials and methods .....</b>	<b>35</b>
3.1	Materials.....	35
3.2	Photodeposition experiments .....	35
3.3	Material characterization methods.....	35
3.3.1	Specific surface area measurements (BET).....	35
3.3.2	Scanning electron microscopy.....	36
3.3.3	Raman spectroscopy .....	36



3.3.4 Diffuse reflectance spectroscopy.....	36
3.4 Electrode preparation.....	36
3.4.1 Screen printing paste preparation.....	36
3.4.2 Electrode coating.....	37
3.5 Flatband potential measurements.....	37
3.6 Photocatalytic H <sub>2</sub> production.....	38
3.6.1 Determination of the quantum yield .....	39
3.7 Laser flash photolysis measurements.....	41
3.8 Electron paramagnetic resonance (EPR).....	43
<b>4. Material characterization.....</b>	<b>45</b>
4.1 Scanning electron microscopy .....	45
4.1.1 Powders.....	45
4.1.2 Electrodes.....	46
4.2 Specific surface area.....	46
4.3 Raman spectroscopy .....	47
4.3.1 Powders.....	47
4.3.2 Electrodes.....	49
4.4 Diffuse reflectance.....	49
4.4.1 Powders.....	49
4.4.2 Electrodes.....	50
4.4.3 Absorption coefficient.....	51
4.5 Flatband potential measurements.....	52
4.6 Quantum yield determination.....	54
<b>5. Results.....</b>	<b>55</b>
5.1 Photocatalytic H <sub>2</sub> evolution upon sub-band gap irradiation.....	57
5.2 Determination of free radicals by EPR.....	58
5.3 Laser flash photolysis.....	61
5.3.1 Band gap excitation with UV(C) light.....	62
5.3.1.1 Excitation in the absence of sacrificial reagent.....	62
5.3.1.2 Excitation in the presence of electron scavengers.....	65
5.3.1.2.1 Bare NaTaO <sub>3</sub> in air .....	65

5.3.1.2.2 Lanthanum doped tantalates in air.....	67
5.3.1.2.3 Bare NaTaO <sub>3</sub> in a molecular O <sub>2</sub> purged atmosphere.....	69
5.3.1.2.4 Platinum photodeposition .....	70
5.3.1.3 Excitation in the presence of hole scavengers .....	74
5.3.1.3.1 Methanol.....	74
5.3.1.3.2 Other alcohols .....	76
5.3.1.4 Excitation in the simultaneous presence of electron and hole scavengers .....	78
5.3.2 Sub-band gap excitation with UV(A) light .....	80
5.3.2.1 Excitation in the absence of sacrificial reagents.....	81
5.3.2.2 Excitation in the presence of electron scavengers .....	83
5.3.2.2.1 Bare NaTaO <sub>3</sub> in air and in a molecular O <sub>2</sub> purged atmosphere .....	83
5.3.2.2.2 Lanthanum doped NaTaO <sub>3</sub> in air.....	85
5.3.2.2.3 Lanthanum doped NaTaO <sub>3</sub> in a molecular oxygen purged atmosphere .....	89
5.3.2.3 Excitation in the presence of hole scavengers .....	91

## **6. Discussion ..... 95**

6.1 Optical and morphological properties .....	95
6.1.1 Band gap energy determination.....	95
6.1.2 Effect of lanthanum doping.....	96
6.2 Energetic position of conduction and valence band .....	98
6.3 Photocatalytic H <sub>2</sub> formation .....	100
6.4 Electron paramagnetic resonance.....	101
6.5 Laser Flash Photolysis .....	103
6.5.1 Band gap excitation with UV(C) light.....	103
6.5.1.1 No sacrificial reagents .....	103
6.5.1.2 Effect of electron scavengers .....	104
6.5.1.2.1 Bare NaTaO <sub>3</sub> in presence of air and molecular oxygen .....	104
6.5.1.2.2 Lanthanum doped NaTaO <sub>3</sub> in air.....	105
6.5.1.2.3 Effect of Pt photodeposition.....	106
6.5.1.3 Effect of hole scavengers .....	111
6.4.1.4 Effect of electron and hole scavengers.....	115
6.5.2 Sub-band gap excitation with UV(A) light .....	115

6.5.2.1 No sacrificial reagents .....	115
6.5.2.2 Electron scavengers .....	117
6.5.2.3 Hole scavengers .....	117
6.5.2.4 Electron trapping in mid-gap states.....	118
6.5.2.5 Two-photon absorption process .....	120
<b>7. Conclusions .....</b>	<b>123</b>
<b>Bibliography .....</b>	<b>127</b>

# Glossary

## Abbreviations

BET	Specific Surface Area (Brunauer Emmett Teller)
XRD	X-Ray Diffraction
SEM	Scanning Electron Microscopy
UV	Ultraviolet
Vis	Visible
NHE	Normal Hydrogen Electrode
ESR	Electron Spin Resonance
EPR	Electron Paramagnetic Resonance
QMS	Quadrupole Mass Spectrometer
QE	Quantum Yield
SG	Sol-Gel Synthesis

## Symbols

$E_g$	Band Gap Energy
$\alpha$	Absorption Coefficient
$\nu$	Oscillation Frequency
$h$	Planck's Constant
$c$	Speed of Light
$\lambda$	Wavelength
$N_A$	Avogadro Constant
$\phi$	Work Function
$A$	Area
$I_0$	Number of Absorbed Photons
$\pi$	Mathematic Constant
$\Delta G_0$	Gibbs Free Energy

## Units

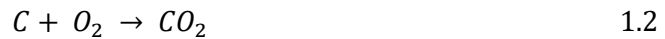
a.u.	Arbitrary Units
%	Percentage
°C	Grad Celsius
wt%	Percentage by Weight
m	Mass
g	Gramm
L	Liter
M	Molar Mass (mol/L)
V	Volume
s	Second
h	Hour
W	Watt
V	Volt
eV	Electron Volt
Å	Angstrom
cm	Centimeter
m	Meter
nm	Nanometer
J	Joule



# 1. Introduction and aim of the work

## 1.1 General background

In the next decades an increase in the worldwide energy demand is projected, with the developing countries being the largest group of energy consumers. Fossil fuels including oil, coal and gas will remain the dominant energy sources being today responsible for approximately 88 % of the world's energy supply. However, combustion of fossil fuels contributes to the so called greenhouse effect, increasing the air pollution by producing CO<sub>2</sub> as can be seen in eq. 1.1 and eq. 1.2 <sup>1,2</sup>.



Due to the depletion of the world's fossil fuel reserves, it becomes inevitable to search for new energy sources that are clean, renewable, cheap and safe. Therefore, solar energy conversion has been receiving more attention in the last decades. The sun provides the earth with a staggering amount of energy but actually only a very small portion is used to directly power human activities <sup>3</sup>. Many researchers have centered their investigation into developing efficient systems to convert solar light into chemical energy. To reduce air pollution and greenhouse gas emission, molecular hydrogen (H<sub>2</sub>) is considered to be an ideal energy alternative in the future <sup>4</sup>. Therefore, H<sub>2</sub> has received considerable attention as a next-generation energy carrier being used in the industrial synthesis of ammonia and other chemicals. The most common method of producing commercial bulk hydrogen is the steam reforming of natural gas:



However, over the last few decades, photocatalytic overall water splitting using sunlight has been studied as a potential method for hydrogen production from clean and renewable sources <sup>5</sup>.



Catalytic splitting of water into H<sub>2</sub> and O<sub>2</sub> is an uphill reaction, involving a positive change in the Gibbs free energy ( $\Delta G_0 = 238 \text{ kJ} \cdot \text{mol}^{-1}$ ). Molecular hydrogen produced

from water splitting using a renewable energy source such as solar light can be considered a green alternative capable of power everything from laptops to submarines<sup>6</sup>.

## 1.2 Photoelectrochemical Water Splitting

### 1.2.1 Photoelectrochemical Cells

Ever since the scientist Edmond Becquerel<sup>7</sup> discovered the photoelectric effect, researchers and engineers have been trying to capture the energy that is freely available from sunlight and turn it into electric power or use it to generate fuels such as hydrogen. Thanks to the innovative work of Fujishima and Honda in 1972, it could be demonstrated that overall water splitting can be achieved using a photoelectrochemical cell (PEC) in which a single-crystal TiO<sub>2</sub> electrode under ultraviolet irradiation is connected with a platinum electrode and an external power supply<sup>8</sup>. The main component of the PEC cell is the semiconductor, which converts incident photons into electron/hole pairs. These electron/hole pairs are spatially separated from each other due to the presence of an electric field inside the semiconductor. The photogenerated electrons are swept toward the conducting back-contact, and are transported to the metal counter electrode via an external wire. At the metal, the electrons reduce water to form hydrogen gas. The photogenerated holes are swept toward the semiconductor/electrolyte interface, where they oxidize water to form oxygen gas<sup>9</sup> as it is illustrated in Fig. 1.1. Since then, many PEC cells have been developed, many of which are designed specifically for the efficient utilization of solar energy. The requirements for solar water splitting materials can be summarized as follows:

- Good (visible) light absorption.
- High chemical stability in the dark and under illumination.
- Band edge positions that straddle the water reduction and oxidation potentials.
- Efficient charge transport in the semiconductor.
- Low overpotentials for reduction/oxidation of water.
- Abundant and cheap synthesis.
- Non-toxic.



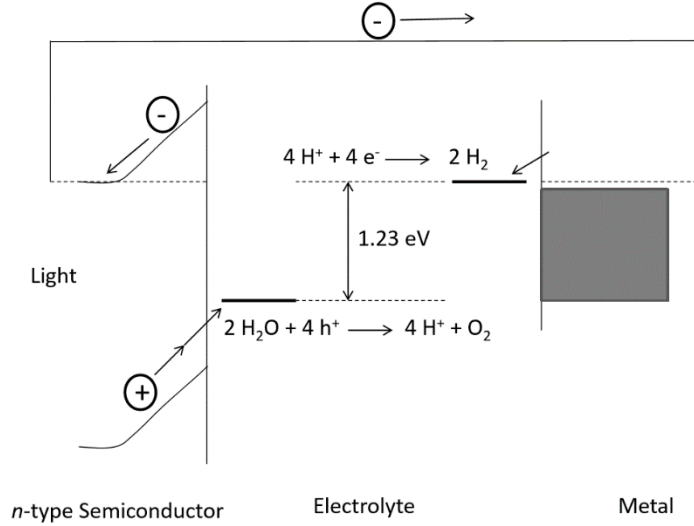


**Figure 1.1:** Illustration of a photoelectrochemical cell that consists of a semiconducting photoanode and a metal cathode.

In semiconductors, the orbitals are merged into a nearly filled valence band and a nearly vacant conduction band separated by a band gap  $E_g$ . When a semiconductor is immersed in a solution, charge transfer occurs at the interface until the electrochemical potential ( $\mu_e$ ) of the electron in both phases are equal. The net result is the formation of an electrical field at the surface of the semiconductor. The direction of this electric field depends on the relative electron affinities of the semiconductors and the solution. For an *n*-type semiconductor, which is one that is doped with a donor species so that some electrons are in the conduction band, the field frequently forms in the direction from the bulk of the semiconductor toward the interface <sup>10</sup> (see Fig. 1.1). A *p*-type semiconductor is one that is doped with an acceptor impurity to produce holes in the valence band. In this case equilibration occurs by electron transfer from the semiconductor to the electrolyte, causing the semiconductor to become positively charged with respect to the electrolyte <sup>11</sup>.

The spectral region in which the semiconductor absorbs light is determined by the band gap of the material. It is necessary for water splitting by semiconductor photocatalysis that the conduction band levels of the material are more negative than the reduction potential of  $\text{H}_2\text{O}$  to produce  $\text{H}_2$  and their valence band levels are more positive than the oxidation potential of  $\text{H}_2\text{O}$  to produce  $\text{O}_2$ . Therefore, the minimum band gap required to split water is 1.23 eV plus the thermodynamic losses (0.3-0.4 eV) and the overpotentials that are required at various points in the system to ensure sufficiently fast reaction kinetics <sup>12</sup>. Hence, the optimum band gap should be between 1.9 and 3.1 eV, which is within the visible range of the solar spectrum.

The chemical stability is a requirement that limits the use of several semiconductor materials. Most non-oxide semiconductors suffer from photocorrosion forming a thin oxide layer that prevents charge transfer across the semiconductor/electrolyte interface. Oxide semiconductors are more stable, but may be prone to anodic or cathodic decomposition. The general trend is that the stability against (photo)corrosion increases with increasing band gap<sup>13</sup>. Although this conflicts with the requirement of visible light absorption.

Titanium dioxide has been the semiconductor favored for the photoelectrochemical studies. Unfortunately, because of its large band gap (3-3.2 eV), TiO<sub>2</sub> only absorbs the ultraviolet part of the solar spectrum. However, due to the lack of suitable photoelectrode materials with appropriate band gap structures and stability, the systems proposed to date have been rather expensive and complicated<sup>14</sup>. The work of Bard and co-workers extended the concept of developing systems for overall water splitting by using semiconductor particles or powders instead of PEC cells<sup>10,11,15</sup>. In comparison with PEC systems, these particulate systems have the advantage of being much simpler and less expensive to construct and use. Moreover, the efficiency of light absorption in suspensions can be very high. Another advantage is that a variety of materials can be used in particulate systems that may not be available as single crystals<sup>11</sup>. However, some challenges such as separation of the products and recombination of the photogenerated charge carriers must be taken into account.

### 1.2.2 Photocatalytic Systems

As early as 1929 it became known that the pigment "titanium white" *i.e.* TiO<sub>2</sub>, is responsible for fading in paints, and major studies into the photosensitizing action of TiO<sub>2</sub> followed<sup>16</sup>. Since then, TiO<sub>2</sub> has been one of the most studied semiconductor materials. Although, other *n*-type oxide semiconductors have been employed as photocatalysts for water splitting, the inappropriate distribution of the conduction and valence bands and / or a too large band gap makes these materials less than ideal for use in photoelectrochemical cells or as particulate systems. Therefore, the need of further investigation of suitable semiconductor photocatalysts is needed.

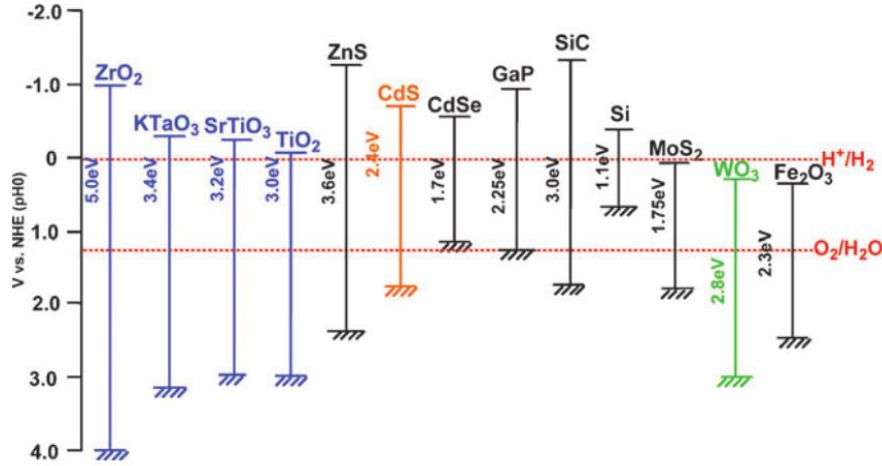
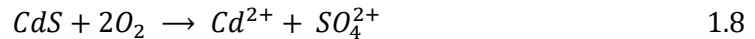


**Figure 1.2:** Energy level diagram indicating the energy positions of the conduction and valence bands of several semiconductors in aqueous media at pH 0<sup>17</sup>.

Band levels of various semiconductor materials are shown in Fig. 1.2. Hereby the metal oxides  $\text{KTaO}_3$ ,  $\text{SrTaO}_3$  and  $\text{TiO}_2$  possess suitable band structures for water splitting under UV irradiation when they are suitably modified with co-catalysts. The two main roles of an efficient co-catalyst are (a) to extract photogenerated electrons or holes from the photocatalyst bulk and (b) to create reaction sites decreasing the activation of energy for gas evolution<sup>18</sup>. Although CdS seems to have an ideal band structure and a band gap within the visible light response (2.4 eV), it is not active for water splitting into  $\text{H}_2$  and  $\text{O}_2$  since  $\text{S}^{2-}$  in CdS is oxidized by the photogenerated electrons rather than  $\text{H}_2\text{O}$ . This is accompanied with the anodic dissolution of the semiconductor and the formation of  $\text{Cd}^{2+}$  according to the following equations<sup>19</sup>:



In the presence of molecular oxygen, the overall process will be:



Semiconducting electrodes often have to be doped to improve their properties. In most cases the aim is to enhance the  $n$ - or  $p$ -type conductivity. Certain dopants may enhance the optical absorption of wide band gap semiconductors<sup>20</sup>, increase the minority carrier diffusion length<sup>21,22</sup> or enhance the photocatalytic activity at the surface of the semiconductor<sup>23</sup>. Other dopants introduce mid gap states or can adversely react as recombination centers<sup>24</sup>. In addition of foreign cation and anion dopants, native point defects are also present in the material such as vacancies, interstitials or substituents<sup>9</sup>. Furthermore,  $\text{KTaO}_3$ ,  $\text{SrTaO}_3$  and  $\text{TiO}_2$  are considered to be the most stable materials for photocatalytic redox reactions since they do not undergo photocorrosion (which is the case of CdS).  $\text{WO}_3$  is a good photocatalyst for oxygen evolution under visible light

irradiation in the presence of electron acceptors such as  $\text{Ag}^+$  and  $\text{Fe}^{3+}$  but is not active for hydrogen evolution because of its low conduction band level. The band edge position is a thermodynamic requirement but not a sufficient condition. The band gap of a visible light driven photocatalyst should be narrower than 3.0 eV ( $>415$  nm). Therefore, suitable band engineering is necessary for the design of photocatalysts with visible light response.

### 1.3 Objectives

Due to the inherent complexity of the photoelectrochemical systems, details of the underlying reaction mechanisms are still far from being understood. The reaction rate of the overall process will be limited by the slowest reaction step, which in most cases is not known. Therefore, a better understanding of the mechanistic details of the photocatalytic process is required before several basic problems such as the preparation of catalysts with improved photocatalytic activity can be addressed in a systematic way.

From the scientific point of view, the focus of this thesis is the elucidation of the fundamental processes that take place during water splitting after light excitation using laser flash photolysis as the chosen method. Based on the work of Kudo *et. al* in 2003, sodium tantalate  $\text{NaTaO}_3$ , has been chosen as a model semiconductor for this work<sup>25</sup>. To this day, lanthanum doped sodium tantalates modified with NiO as co-catalyst have shown the highest apparent quantum yield for water splitting (56 %) when the material was irradiated with a wavelength of 270 nm<sup>25</sup>. The sodium tantalate materials used in this thesis have been synthesized by solid state reactions by the H.C. Starck Company (Goslar) and delivered to the Leibniz University of Hannover. This took place within the framework of a joint BMBF Project called “Neue Katalysatoren und Technologien für die solar-chemische Wasserstoffherzeugung” (“Hycats”). Although these materials do not receive special interest as photocatalysts for possible future solar energy applications because of their wide band gap (4.0 eV), they constitute a suitable model for research. In the first part of this work, characterization of the materials has been done using different techniques such as scanning electron microscopy, specific surface area measurements, Raman spectroscopy, diffuse reflectance, photocatalytic hydrogen evolution and electron paramagnetic resonance.

The central objective of the present thesis, however, is to investigate the photogenerated charge carrier dynamics of the sodium tantalate materials using laser flash photolysis measurements. A deeper understanding of the mechanisms of these materials will lead to optimization and a better design of novel semiconductor materials suitable for overall water splitting. In this work different aspects are studied, *i.e.*, lanthanum doping and in particular, photodeposition or loading of sacrificial reagents in order to investigate their impact on the charge carrier dynamics. As was reported from A. Kudo and H. Kato<sup>25,26</sup>, the activities of tantalates for water splitting were improved after doping with lanthanides, with lanthanum being the most effective dopant. Only few works<sup>18,27</sup> can

be found that study  $\text{NaTaO}_3$  using laser flash photolysis. It has to be noted that some laser flash studies done to date were performed with colloidal solutions whilst in this thesis the measurements were done directly to the powders using a diffuse reflectance accessory.

The photocatalytic activity can be improved by loading different co-catalysts on the host surface due to the trapping of photogenerated charge carriers and / or creation of active sites. In this work, the sodium tantalate powders were modified by photodeposition of Pt nanoparticles on the surface of the photocatalyst, in order to study the importance of the presence of small noble metal islands in the kinetics of the photogenerated charge carriers.

Several alcohols have shown different photocatalytic activities for  $\text{H}_2$  evolution using different photocatalysts including  $\text{TiO}_2$ . These alcohols act as electron donors, trapping the photogenerated holes and hindering the recombination reaction. However, systematic study of the effect of alcohols on the dynamics of the photogenerated charge carriers using sodium tantalate materials has not been carried out yet. Only a few mechanistic studies have been published (mainly on  $\text{TiO}_2$ ) dealing with the fundamental understanding of the photocatalytical processes occurring in the presence of such sacrificial reagents.

It has to be noted that all measurements in this work have been performed employing two different laser excitation wavelengths (248 and 351 nm), in order to evaluate the behavior of the different photogenerated charge carriers when light with sub-band gap and super-band gap is used to excite the sample.



## 2. Theoretical background

### 2.1 Band bending and formation of Schottky barriers

The properties of semiconductors depend strongly on their electronic structure. Due to the essentially infinite number of atoms that must be considered, the electronic structure of these solids is typically discussed in terms of energy bands. There are two atomic levels, which are of considerable importance: the highest occupied and the lowest unoccupied by electrons. These two atomic levels give rise to two different bands in the solid. The band resulting from the lowest occupied level is called the valence band ( $E_{\text{VB}}$ ) and that resulting from the unoccupied level is the conduction band ( $E_{\text{CB}}$ ). Thus, the valence band will be totally occupied by electrons, whereas the conduction band will be partially or totally free of electrons. The metallic, semiconductor or dielectric properties of a solid are determined by the factor how the two bands are filled by electrons. The difference between the top of the valence band and the bottom of the conduction band is called the electronic band gap ( $E_{\text{g}}$ ). Usually if the band gap is in the range of 1 to 4 eV, the material is considered a semiconductor<sup>28</sup>. Thus, in the semiconductors, the band gap is not so large and the electrons can be transferred from the valence band to the conduction band *e.g.* by thermal excitation when the semiconductor is irradiated with light of an energy equal or greater than the band gap. The excitation of electrons leaves positively charged vacancies in the valence band of the semiconductor, that are mobile and usually called "holes". A hole is an empty level in the valence band, or in other words, a valence bond with a missing electron. As a result, the current in semiconductors is made up by two components: the mobile electrons in the conduction band and the mobile holes in the valence band<sup>29</sup>.

It is clear that the positions of the band edges have a crucial influence on the photoactivity of the semiconductors. This is due to the fact that the band edge positions will normally depend on surface charging. This will be highly dependent not only on the ionic conditions in a concrete electrolyte (pH, specific absorption of ions), but also on the surface structure and composition of the material, which in turn, will depend on the particular synthetic strategy used for the fabrication<sup>30</sup>.  $\text{NaTaO}_3$  is a *n*-type semiconductor. This means that its Fermi level ( $E_{\text{F}}$ ) is typically right below the conduction band edge. From the thermodynamic point of view, the Fermi level is the electrochemical potential of the electron in the solid. Equivalently, from the statistical point of view, the Fermi level is the energy at which the probability of an energy level of being occupied by an electron (the Fermi function) is 0.5 (note, however, that this not implies that the level at the Fermi level is populated by electrons because the population depends upon the product of the Fermi function and the electron density of states). Hence, the Fermi level describes the occupation of energy levels in a semiconductor in thermodynamic equilibrium<sup>30</sup>. However, the condition of thermodynamic equilibrium is not always fulfilled (particularly when excess electrons and holes are photogenerated under illumination or injected under electric bias).

Accordingly, the electron and hole densities in the conduction and valence bands are not described by the same Fermi level but by a quasi-Fermi level of electrons ( $*E_{Fn}$ ) and a quasi-Fermi level of holes ( $*E_{Fp}$ ) respectively<sup>13,29,31</sup>. It should be also noted that the generation of electron/hole pairs usually occurs near the semiconductor surface due to the small penetration of light, which leads to variations in the quasi-Fermi level of holes with the distance from the surface. Importantly, in case of *n*-doped semiconductors such as TiO<sub>2</sub> and NaTaO<sub>3</sub>, the lower conduction band edge practically merges with the quasi-Fermi level of the electrons ( $E_{CB} - *E_{Fn} < 0.1$  V).

The determination of the conduction band edge often translates into the measurement of the position of the quasi-Fermi level of the electrons. Once this is known, the position of the valence band edge can be simply calculated by adding the value of the band gap energy, that is, typically determined by optical<sup>13,32-34</sup> or photoelectrochemical methods<sup>35,36</sup>. Another important concept is the flatband potential ( $E_{FB}$ ). After the contact of the semiconductor surface with the electrolyte, the thermodynamic equilibrium of both sides must be established<sup>13,29,37</sup>. This equilibration happens through electron transfer across the interface, which results in the formation of a space charge layer (also called depletion layer since the surface region of the semiconductor is depleted of its majority charge carriers). It is important to realize that in the case of *n*-type semiconductors, this interfacial transfer process produces an excess of positive charges in the semiconductor and an excess of negative charges in the electrolyte. With more electrons exchanged, the electric field of the negative charges on the solution side hinders further electron transfer so that the equilibrium is established and no net charge flow occurs<sup>30</sup>. As a consequence the bands are bent upwards, which can be understood in terms of a continuously growing barrier for interfacial electron transfer when moving from the bulk of the semiconductor to the interface due to the continuously less efficient screening of the negative charges in the solution by the positive charges in the depletion layer<sup>30</sup>. The height of the barrier is the energy difference between the conduction band edge in the bulk semiconductor and the conduction band edge at the surface and correspond to the potential drop in the space charge layer  $U_s$ .

In Fig. 2.1 are illustrated two possibilities of the semiconductor/electrolyte contact (the figure only illustrates the possibilities of an *n*-type semiconductor). When the Fermi level of the semiconductor lies higher in energy than the redox potential of the electrolyte solution Fig. 2.1(a), electrons will be transferred from the semiconductor to the electrolyte. This is reflected in an upward bending of the band edges<sup>38</sup>. Since the majority charge carriers of the semiconductor has been removed (electrons for an *n*-type semiconductor) a region called depletion layer is formed. The Fig. 2.1 (b) shows a semiconductor with a Fermi level lower in energy than the redox potential of the electrolyte. In this case, electrons flow from the electrolyte solution to the semiconductor and an accumulation layer is formed. This band bending phenomenon is by no means exclusively for the semiconductor/electrolyte interface. Analogous electrostatic adjustments occur whenever two different phases are in contact (*e.g.* semiconductor/gas, semiconductor/metal)<sup>28</sup>. An important



distinction from the correspondent metal case now becomes apparent. For a metal, the charge, and thus the associated potential drop, is concentrated at the surface penetrating at most a few angstroms into the interior. The high conductivity of a metal cannot support an electric field within it. Thus, when a metal electrode comes in contact with an electrolyte, almost all the potential drop at the interface occurs at the Helmholtz region in the electrolyte phase.

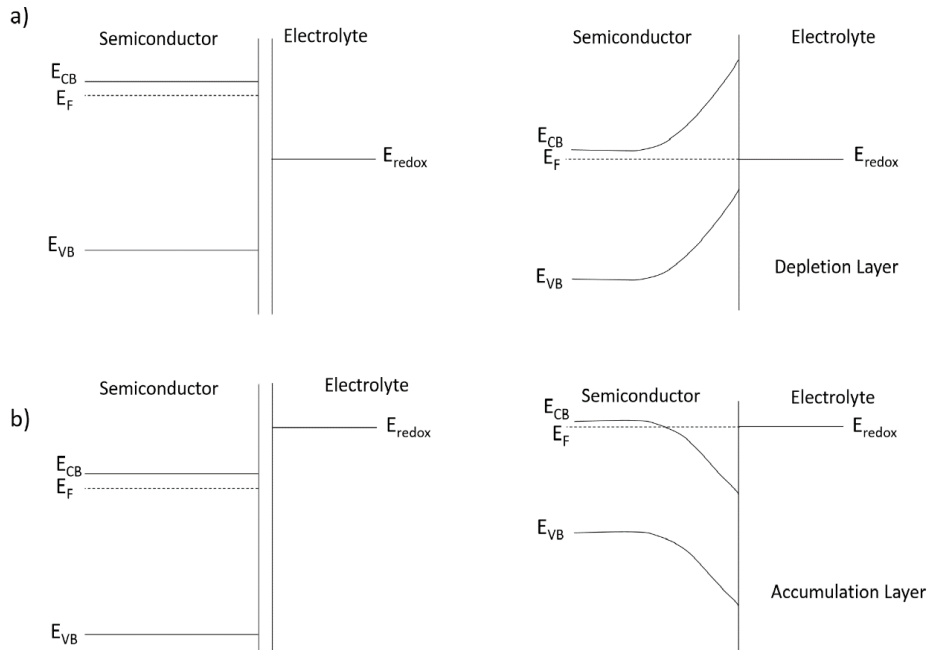


**Figure 2.1:** Scheme of the *n*-type semiconductor/electrolyte contact. (a) semiconductor with a Fermi level higher in energy than the redox potential of the electrolyte. After equilibrium a depletion layer is formed. (b) semiconductor with a Fermi level lower in energy than the redox potential of the electrolyte. After contact, an accumulation layer is formed.

In general, at a metal/semiconductor interface an ohmic contact and a Schottky contact can be differentiated. At an ohmic contact, a metal/semiconductor contact with a low electric resistance is formed. The main difference with the Schottky contact is that due to the low resistance, a continuous flow of charge carriers between the metal and the semiconductor as well as from the semiconductor to the metal is observed. Therefore, it is considered a linear transition. The formation of an ohmic contact depends of the band gap ( $E_g$ ) and the Fermi level ( $E_F$ ) of the metal and the semiconductor. If the difference between the Fermi level of the semiconductor and the metal is small, the band bending will be small as well. In Fig. 2.2 a current/voltage diagram of an ohmic contact is represented.

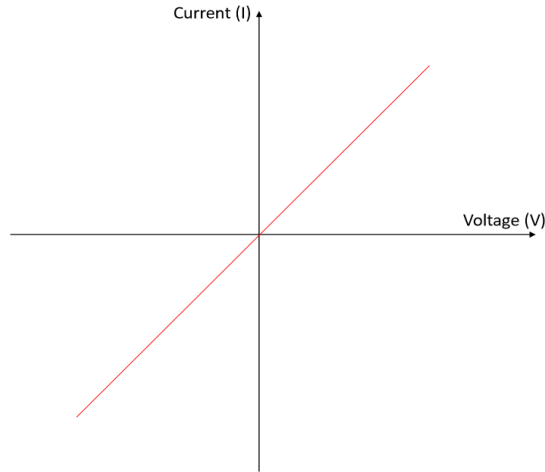


**Figure 2.2:** Illustration of a current/voltage diagram of an ohmic contact.

In the case of a Schottky contact, the difference between the Fermi levels of the metal and the semiconductor is higher than for an ohmic contact and therefore, the band bending is more pronounced and a higher electric resistance is obtained. This resistance leads to a potential barrier that forces the electric flow only in one direction through the metal/semiconductor interface. In Fig. 2.3 a current/voltage curve of a Schottky contact is illustrated. The red area in the figure corresponds to a blocking area where no transport of charge carriers occurs. This is the main difference between ohmic and Schottky contact. If a voltage higher than the potential barrier is applied an electric flow results, which is represented in the green area from the Fig. 2.3. For illustrate completely the photocatalytic process, the semiconductor/electrolyte interface has to be taken into account as well. In Fig. 2.4 is represented a contact between metal/semiconductor/electrolyte under semiconductor illumination.

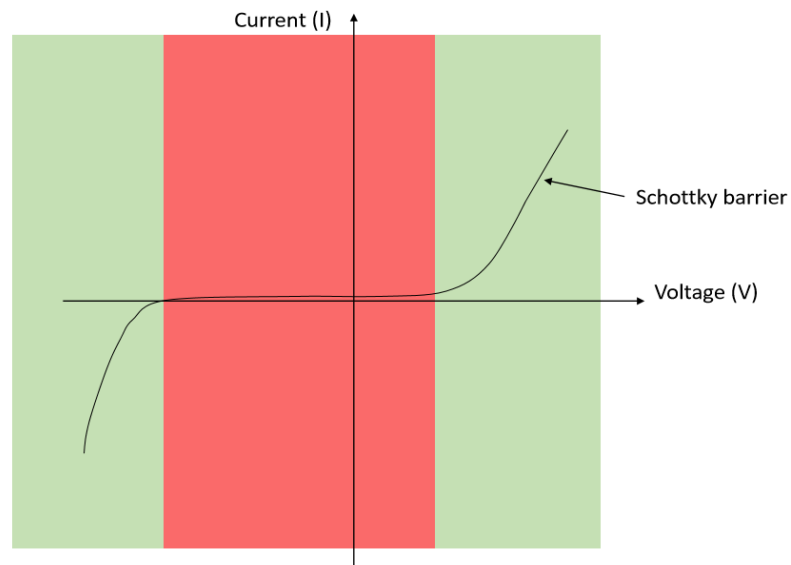


**Figure 2.3:** Illustration of a current/voltage diagram of a Schottky contact.

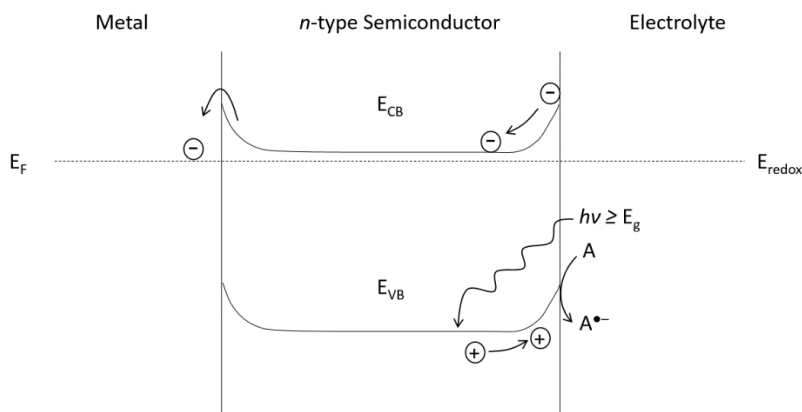


**Figure 2.4:** Metal/semiconductor/electrolyte contact under semiconductor irradiation.

As it has already been explained, the Fermi levels and the redox potentials of the different materials have to align. This results in a band bending in the semiconductor at the metal/semiconductor and semiconductor/electrolyte interfaces. The potential barriers at the metal/semiconductor and semiconductor/electrolyte interfaces are responsible for the separation of the charge carriers. The barrier formed at the metal-semiconductor interface is called the Schottky barrier and can serve as an efficient barrier to prevent the undesired electron migration back to the semiconductor<sup>39</sup>. While the electrons are trapped at the noble metal surface, the holes remain at the host photocatalyst and migrate to its free surface ensuring an efficient charge separation<sup>40</sup>.

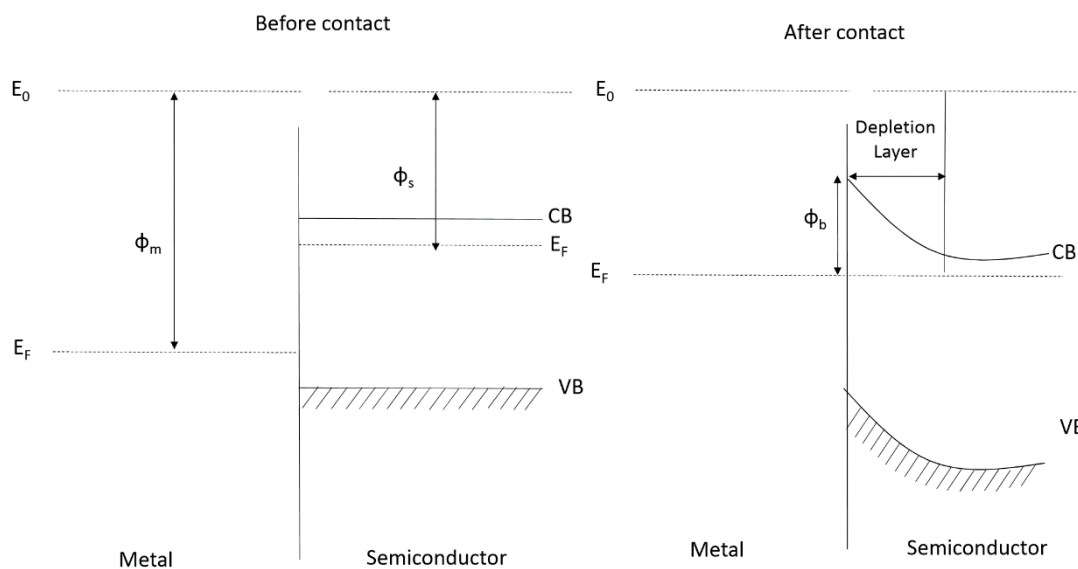


**Figure 2.5:** Scheme of the metal/semiconductor interface.  $E_0$ : vacuum level,  $E_F$ : Fermi level,  $\phi_m$ : work function of the metal,  $\phi_s$ : work function of the semiconductor,  $\phi_b$ : barrier height.

The effect of different metals like Pt, Au and Ag after the deposition on titanium dioxide have been extensively studied <sup>41</sup>. The difference in their photocatalytic activity can be related to their work function values ( $\phi$ ), which can be defined as the energy required to promote an electron from the Fermi level into the level of energy where the electron can move freely in the space (vacuum) <sup>42</sup>. The higher the work function value, the lower the Fermi level and the bigger the difference between work function of metal and semiconductor <sup>43</sup> (see Fig. 2.5). Therefore, the Schottky barrier will be increased leading to a more efficient electron trapping by the loaded metal, an efficient charge separation and higher photocatalytic activity for hydrogen evolution. There is a characteristic region near the semiconductor surface from which the charge is removed by the equilibration process. Beyond this boundary in the bulk of the semiconductor, the ionized donors (for an  $n$ -type semiconductor) have their compensating charge (electrons), and the semiconductor as a whole is electrically neutral. This layer near the surface is called space charge layer or depletion layer, so termed because the layer is depleted of the majority charge carriers <sup>28</sup>. The potential distribution in this interfacial region can be quantified by relating the charge density and the electric field strength  $\Delta\phi$  as embodied by the Poisson equation eq. (2.1) <sup>28</sup>:

$$\Delta\phi (X) = \left( \frac{qN_D}{2\varepsilon\varepsilon_0} \right)^2 (0 \leq x \leq W) \quad 2.1$$

Where  $q$  is the electronic charge,  $\varepsilon$  and  $\varepsilon_0$  are the relative permittivity of the semiconductor and the relative permittivity of vacuum respectively,  $N_D$  is the semiconductor doping level and  $W$  is the width of the space charge layer. The thickness of the space charge layer is related to the potential drop between the bulk and the surface of the semiconductor, by the following expression <sup>28</sup>:

$$W = \left| \frac{2\varepsilon\varepsilon_0}{qN_D} \left( U_s - \frac{kT}{q} \right) \right|^{1/2} \quad 2.2$$

where  $U_s$  is the potential drop in the space charge layer. It is obvious that the magnitude of  $W$  depends on the semiconductor doping level  $N_D$ . Consider two cases of a semiconductor, one that is lightly doped ( $N_D \sim 10^{16} \text{ cm}^{-3}$ ) and another that is heavily doped ( $N_D \sim 10^{18} \text{ cm}^{-3}$ ) <sup>28</sup>. Obviously, in the former case, the charge needed for Fermi level equilibration has to come from deeper inside the solid and so the magnitude of  $W$  will be larger <sup>28</sup>. Nominal dimensions of  $W$  are in the 10-1000 nm range. This may be compared with the correspondent Helmholtz layer width, typically 0.4-0.6 nm <sup>28</sup>. The value of  $U_s$  can be obtained as:

$$U_S = E_{appl} - E_{FB} \quad 2.3$$

where  $E_{appl}$  is the externally applied potential and  $E_{FB}$  is the potential at which  $U_s = 0$  and the bands in the semiconductor are flat (flatband potential). It is therefore clear that the value of  $E_{FB}$  is of fundamental significance since it gives a direct information of the position of the conduction band edge at the  $n$ -type semiconductor's surface, assuming that the

difference between  $E_{FB}$  and  $E_C$  is very small for doped semiconductors. In other words, the determination of the conduction band edge often translates into the measurement of the flatband potential.

The study of the band edge placement can be done through differential capacitance measurements on the semiconductor/redox electrolyte interface. For this purpose, the Mott-Schottky relation is employed <sup>28</sup>:

$$\frac{1}{C_{SC}^2} = \frac{2}{N_D e_0 \epsilon_{SC} \epsilon_0} \left| (E - E_{FB}) - \frac{kT}{e_0} \right| \quad 2.4$$

Where  $C_{SC}$  is the depletion layer capacitance and  $E_{FB}$  is the so called flatband potential. Therefore, a plot of  $1/C^2$  against  $E$  should yield a straight line from which  $E_{FB}$  can be determined from the intercept with the X-axis.

## 2.2 Photoelectrochemical water splitting

Although Bequerel with his measurement of photovoltaic effect an illuminated silver chloride electrode <sup>7</sup> (*ca.* 1839) can be viewed as the founder of photoelectrochemistry, it is the measurements by Honda and Fujishima published in 1972 that really showed the potential of photoelectrochemical systems to harvest and store solar energy <sup>8</sup>. In the Honda-Fujishima experiment, titanium dioxide ( $TiO_2$ ) was used as the photoanode material to produce hydrogen from water using the energy of light.

The principle of a photoelectrochemical cell (PEC) is shown in Fig. 2.6, where a *n*-type semiconductor is irradiated with light. The absorption of a photon creates an electron/hole pair that can either recombine or separate through the semiconductor/electrolyte interface. The photogenerated electrons on the conduction band wander to the counter electrode to reduce water to form molecular hydrogen. The photogenerated holes oxidize water to form molecular oxygen on the semiconductor electrode. This is possible only when the electron/hole pairs have the adequate redox potentials (including overpotentials). If that is not the case, the reaction has to be supported by applying an external bias (as in the case of the Honda-Fujishima experiment).

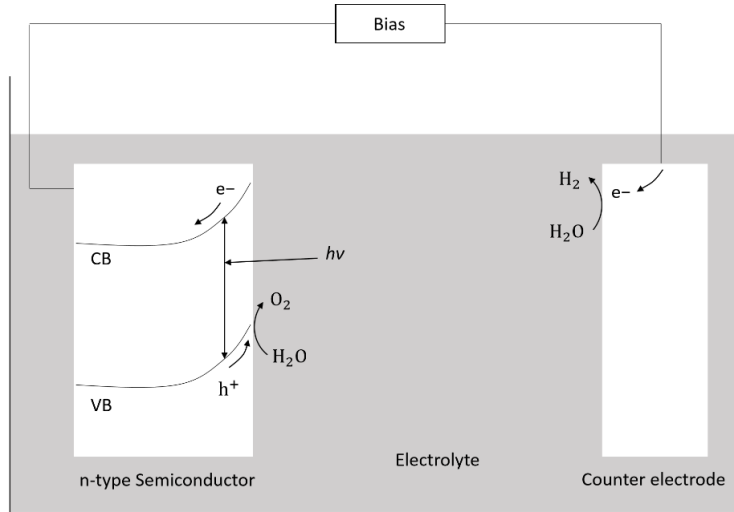


**Figure 2.6:** Principle of the photoelectrochemical water splitting using *n*-type semiconductors <sup>17</sup>.

The photoelectrochemical water splitting reactions can be explained using the next half-reactions:

Generation of an electron/hole pair:



Anodic reaction (oxidation):



Cathodic reaction (reduction):



Overall:



In order to initiate the redox reaction, the highest level of the valence band should be more positive than the water oxidation level ( $E(O_2/H_2O) = 1.23 \text{ V vs. the normal hydrogen electrode; NHE}$ ), while the lowest level of the conduction band should be more negative than the hydrogen evolution potential ( $E(H_2/H_2O) = 0 \text{ V vs. NHE}$ ).

### 2.3 Photocatalytic water splitting

Photocatalytic water splitting has been extensively studied from a point of view of photon energy conversion, for the production of molecular hydrogen and oxygen using particulate photocatalyst systems<sup>44</sup>. The general principle of the conversion of light into chemical energy is illustrated in Fig. 2.7. It is commonly accepted that the reaction progresses via a multi-step route. The absorption of a photon (1) with an energy equal or greater than the band gap energy leads to the formation of an electron/hole pair in the bulk.

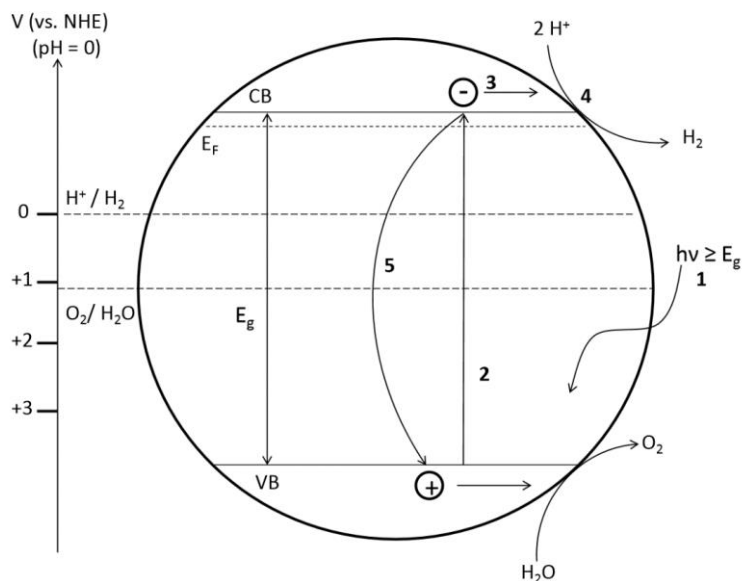


**Figure 2.7:** Illustration of the overall water splitting processes at a heterogeneous particulate system.

The photogenerated electrons are transferred to the conduction band (CB) whilst the photogenerated holes remain in the valence band (VB) (2). Thereafter, the photogenerated charge carriers migrate to the surface (3) without recombination, they are reduced and oxidized by the electrons and holes to produce molecular  $\text{H}_2$  and  $\text{O}_2$  (4). The first three steps are strongly dependent on the structural and electronic properties of the photocatalyst. In general, high crystallinity should have a positive effect on the activity since the density of defects, which act as recombination centers between photogenerated charge carriers (5) decreases with increasing crystallinity<sup>17</sup>. The fourth step on the other hand, is promoted by the presence of a solid co-catalyst. The co-catalyst is usually a noble metal or a metal oxide and is loaded at the photocatalyst surface to produce active sites and reduce the activation energy for gas evolution. To achieve overall water splitting, the bottom of the conduction band must be more negative than the reduction potential of  $\text{H}^+$  to  $\text{H}_2$  (0 V vs. NHE), while the top of the valence band must be more positive than the oxidation potential of  $\text{H}_2\text{O}$  to  $\text{O}_2$  (1.23 V vs. NHE). Therefore, the positions of the band edges are determined in this thesis for bare and La-doped  $\text{NaTaO}_3$  in order to evaluate if the electron transfer in the system is possible. In contrast to a photoelectrochemical cell,

the spatial separation between oxidative and reductive sites in a particulate system is very low, thus increasing the undesired back reaction, *i.e.*, water formation to a great extent <sup>15</sup>.

### 2.4 Photocatalyst surface modification

One of the most important challenges of the photocatalytic water splitting process is the separation of the photogenerated charge carriers to inhibit the recombination reaction. One of the used methods to achieve this purpose is the loading of different co-catalysts on the semiconductor surface. Noble metals are widely used and are well known effective co-catalysts for improving the efficiency of water splitting, particularly increasing molecular hydrogen evolution <sup>45-48</sup>. It is known that in the presence of noble metal islands on the surface of a semiconductor photocatalyst, a more efficient charge separation and transfer can be achieved by suppressing the electron/hole recombination. Noble metal particles loaded on the semiconductor surface are very effective electron traps due to the formation of a Schottky barrier at the metal-semiconductor contact <sup>49,50</sup>. It is widely believed that lattice defects in crystalline photocatalysts particles are responsible for the electron/hole recombination, although no direct observation of the recombination has been performed <sup>51</sup>. However, one of the most significant problems may be the misconception that the recombination centers must be crystal lattice defects <sup>51</sup>. Most photocatalysts are categorized as *n*-type semiconductors. It is known that metal oxides tend to release oxygen, leaving electrons in the lattice that may be the origin of the *n*-type semiconductor property of metal oxides. Actually, titania turns blue-black when heated under a reduced atmosphere due to the release of oxygen and leading to the formation of reduced titanium species (Ti<sup>III</sup>). In an electrochemical sense, this phenomenon corresponds to the formation of electron-filled donor levels located below the conduction band. The Fermi level is located between the conduction band and those donor levels <sup>51</sup>.

### 2.5 Laser flash photolysis

The principle of the catalyzed reactions on semiconductor nanoparticles has been widely investigated over the last years <sup>52-55</sup>. Once electron/hole pairs are generated upon light irradiation, the majority of them recombine, generating heat. Only a small fraction transfers to the interface and takes place in successful redox reactions. The timescale of the interfacial electron transfer and the lifetime of the photogenerated charge carriers determine the efficiency of the photocatalytic process. Electron photogeneration and recombination and electron transport are the elementary processes accounting for the conversion of light into useful charge carriers. Hence, increasing the efficiency of charge separation/transport in semiconductors nanoparticles is one of the major problems in photocatalysis to be addressed.

The fundamental study of the dynamics of the charge transfer processes is very important for designing new photocatalysts as well as for the industrialization process. The use of time resolved spectroscopy covering different time scales and spectral ranges is a powerful



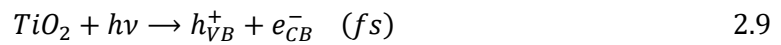
tool to study the light induced electron transfer processes and provide valuable mechanistic information <sup>56</sup>. Extensive investigations have been performed concerning the study of the kinetics and of mechanistic information of the interfacial electron transfer processes at the semiconductor/water interface using laser flash photolysis <sup>57,58</sup>. It has to be noted that transient absorption spectra of electrons and holes in TiO<sub>2</sub> are very broad, extending from the UV to the IR region <sup>59,60</sup>.

Most of the early research concerning the electron/hole dynamics in titanium dioxide by transient absorption spectroscopy was performed with colloidal TiO<sub>2</sub> nanoparticle samples <sup>59,61-63</sup>. The assignments of electrons and holes were made by measuring the transient absorption spectra in the presence of electron and hole scavengers in the colloidal solution. According to these studies, trapped holes absorb light at around 500 nm and electrons around 700 nm <sup>59,63,64</sup>. However, the use of colloidal solutions can present some problems because its stability is only achieved at certain pHs. Therefore, there is a difference between the work done in colloidal solutions and in nanocrystalline TiO<sub>2</sub> films <sup>60</sup>. The use of films avoids the limitations of the colloidal solutions because they are prepared by fixing the semiconductor powder directly onto a substrate.

### 2.5.1 Dynamics of charge carrier trapping and recombination

Exciting a semiconductor with any light source produces different transitions. If the photon energy is equal or greater than the band gap, interband transitions dominate and the electrons are excited from the valence band to the conduction band. This process takes place in the femtosecond (fs) time scale <sup>60,65</sup>. According to the work of Tamaki et al. <sup>60</sup>, the photogenerated electrons and holes migrate to the surface of the semiconductor and can get trapped there, which is a process that occurs at the sub-ps time scale. At the same time, the electrons and holes can be trapped in the bulk as well. At the surface of the photocatalyst, the trapped electrons and holes can recombine or can be transferred to acceptor or donor molecules, respectively, and react with them. Hoffmann et al. <sup>54</sup> summarized a general mechanism of heterogeneous photocatalysis on TiO<sub>2</sub> as follows:

Charge carrier generation:



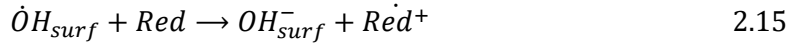
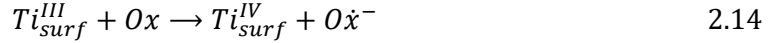
Charge carrier trapping:



Charge carrier recombination:



Interfacial charge transfer:



where  $e_{CB}$  is a conduction band electron,  $h_{VB}^+$  is a valence band hole, Red is a reductant (*i.e.*, an electron donor) and Ox is an oxidant (*i.e.*, an electron acceptor). According to the previous mechanism the interfacial charge transfer efficiency is limited by two factors: the competition between charge carrier recombination and trapping followed by the competition between charge carrier recombination and interfacial charge transfer. The overall quantum efficiency for interfacial charge transfer is determined by two critical processes: the competition between charge carrier recombination and trapping (that happens in the picoseconds to nanoseconds time scale), and the interfacial charge transfer (that takes place in microseconds to milliseconds). An increase in either the lifetime of charge carriers or the interfacial electron transfer rate constant is expected to result in higher quantum efficiencies. Time resolved laser flash photolysis technique is one of the most frequently employed methods for the measurement of the charge carrier transfer dynamics at semiconductor nanoparticles<sup>55,57,58</sup>. The basic approach is to excite the semiconductor nanoparticles with short femtosecond to nanosecond laser pulses generated from an ultrafast laser system. The excited charge carriers are then monitored with a continuous light beam. The change in the absorption of the continuous light reflects the change in the population of the excited charge carriers.

### 2.5.2 Trapped and free charge carriers in semiconductor particles

Heterogeneous photochemical charge transfer reactions are often performed with semiconductor nanoparticles that have trapping sites in the bulk and at the surface. After charge separation in absence of hole scavengers but in presence of oxygen which act as an electron scavenger, the remaining photogenerated holes oxidize water to produce adsorbed hydroxyl radicals that can take place in subsequent oxidation reactions. However, in presence of hole scavengers such as alcohols and in the absence of oxygen (electron scavenger), the fate of the photogenerated electrons is not clear. The work of Bahnemann *et al.*<sup>59</sup>, showed that the excess of electrons are trapped close to the surface of colloidal particles forming  $Ti^{III}$  which has a broad absorption spectra with maximum at 650 nm. On the other hand, trapped holes oxidize the water at the surface producing the surface hydroxyl radicals exhibit transient absorption signals at 430 nm.

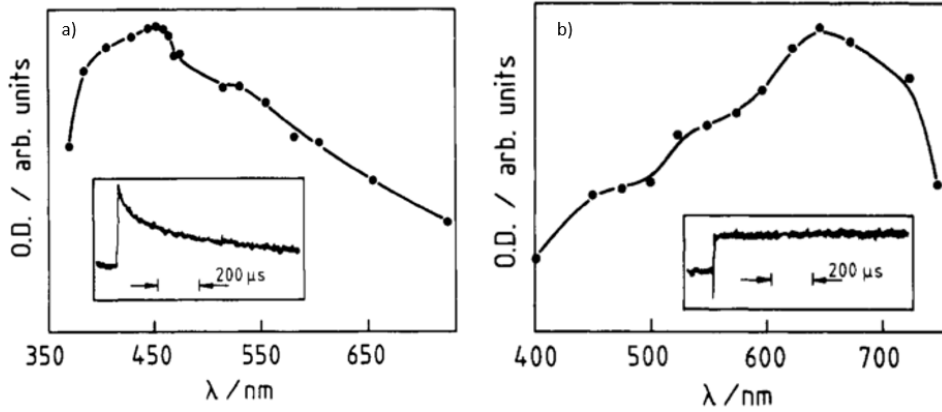
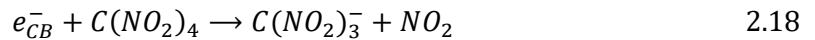


**Figure 2.8:** a) Optical absorption of a  $\text{TiO}_2$  sol containing colloidal Pt and the time profile of the absorption at 472 (inset). b) Optical absorption of polyvinyl alcohol containing  $\text{TiO}_2$  sol and the time profile of the absorption at 625 nm (inset).<sup>59</sup>

In Fig. 2.8 (a) the transient absorption spectrum of a  $\text{TiO}_2$  sol containing colloidal Pt can be observed. It has been reported that Pt loaded on titanium dioxide surfaces act as an electron scavenger. In absence of platinum, the absorption with a maximum at 430 nm could not be seen. This means that the spectrum showed belongs to positive holes which are trapped close to the surface of the colloidal particles<sup>59</sup>. In the part b of the Fig. 2.8 the transient absorption spectrum of a  $\text{TiO}_2$  sol containing polyvinyl alcohol as electron donor is observed. After irradiation, an absorption was present immediately after the laser pulse which did not disappear in the time of observation of several milliseconds. This spectrum is attributed to long-lived reducing intermediates from the photolysis of  $\text{TiO}_2$ <sup>59</sup>.

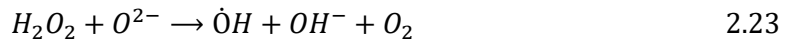
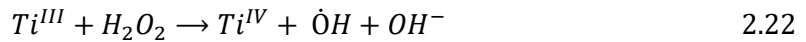


### 2.5.2.1 Hole trapping

Besides the recombination reaction, different possibilities for the charge carrier exist at the semiconductor surface such as trapping (although the recombination process is very fast). There have been studies that tried to identify the nature of the trapping sites for the photogenerated holes in  $\text{TiO}_2$ <sup>66</sup>. Usually, it is assumed that holes can be trapped either at bridging oxygens ( $\text{O}^{2-}$ ) or can be transferred to  $\cdot\text{OH}$  anions bound to the surface which will lead the formation of  $\text{O}^{\bullet-}$  and/or  $\cdot\text{OH}$  centers respectively<sup>67</sup>. To investigate if hydroxyl groups superficially adsorbed onto the titanium dioxide can actually trap photogenerated charge carriers, some groups have performed EPR studies that show that the oxidation of water on the titanium dioxide surface through valence band holes, leads to the formation

of  $\cdot\text{OH}$  radicals<sup>68,69</sup>. The standard redox potentials  $E^0(-\text{OH}_{\text{aq}}/\cdot\text{OH}_{\text{aq}}) = 1.9 \text{ V}$  (*vs.* NHE) and  $E_0(\text{H}_2\text{O}_{\text{aq}}/\cdot\text{OH}_{\text{aq}} + \text{H}^+_{\text{aq}}) = 2.73 \text{ V}$  (*vs.* NHE) are located at a less positive potential than the valence band edge of  $\text{TiO}_2$  and therefore the photogenerated holes are able to produce such species<sup>70</sup>.

The work of Bredow *et al.*<sup>71</sup> however, showed in their model calculations that the potential barriers for the desorption of  $\cdot\text{OH}$  radicals are too high, and therefore the formation of free hydroxyl radicals on the surface of titanium dioxide is considered rather unlikely. Nevertheless, Imanishi *et al.*<sup>72</sup> estimated the energy levels of the O 2p orbitals for  $\text{H}_2\text{O}_{\text{aq}}$  and  $-\text{OH}_{\text{aq}}$  at the  $\text{TiO}_2/\text{water}$  interface. These effective O 2p levels were found to be far below the valence band of titanium dioxide; thus the oxidation of adsorbed water molecules to  $\cdot\text{OH}$  radicals through the photogenerated holes was excluded. The formation of  $\cdot\text{OH}$  radicals during the photocatalytic process cannot be excluded as it is shown in the mechanism proposed by Salvador *et al.*<sup>73</sup> in which the  $\cdot\text{OH}$  radicals are formed through subsequent  $\text{O}_2$  reductions:



Although  $\text{H}_2\text{O}_2$  is a very poor UV radiation absorbent (absorption at  $\lambda \leq 365 \text{ nm}$  is practically inexistent)<sup>73</sup>.



with  $\text{O}_s$  being lattice bound oxygen atoms. At room temperature, the holes will be trapped at different locations and distributed over a certain radius within the surface layer. Therefore, the trapped holes do not stay localized at certain surface sites but rather delocalized over the entire surface region. Shapovalov and co-workers<sup>74</sup> suggest that the holes can be delocalized over at least two oxygen atoms and both  $\text{O}^- - \text{Ti}(\text{IV}) - \text{OH}$  and  $\cdot\text{OH}$  can be formed. The concentration of these species however, will depend on the surrounding. For example, hydroxyl radical scavengers would shift the equilibrium toward  $\cdot\text{OH}$  formation. On the other hand, strong acids and bases could shift the equilibrium away from generation of hydroxyl radicals. These results are supported by theoretical calculations performed by Ji *et al.*<sup>75</sup>, in which they reported that in the presence of a water

molecule the electron can be transferred from water to a bridging oxygen through the formation of a hydroxyl radical.

The transient absorption spectroscopy is a very useful technique to study reaction dynamics and the formation of trapped states at the surface. For example, free  $\cdot\text{OH}$  and free  $\text{O}\cdot^-$  exhibit a transient absorption with a maximum at 260 nm <sup>76</sup>. When these free radical groups are however, located at superficial Ti sites, usually a substantial red shift of the transient absorption measurements can be observed <sup>77</sup>. The transient spectra of the trapped holes can slightly change when comparing the results of different researchers. This can be an indicator of the existence of different trapped states coexisting in the  $\text{TiO}_2$  particles (or different  $\text{TiO}_2$  particles).

Bahnemann *et al.* <sup>63</sup> performed a laser flash photolysis study using colloidal titanium dioxide suspensions and found that at least two different types of holes have to be taken into consideration. Holes which are trapped in energetically deep traps can be characterized by their transient absorption at 450 nm and shallowly trapped holes, which exist in a thermally activated equilibrium with free holes and possess a very high oxidation potential. Moreover, these shallowly trapped holes do not exhibit any transient absorption between 450 and 600 nm. These differences of the transient absorption spectra can also be attributed to the fact that the charge carriers are delocalized over different trapping sites resulting in a broad transient spectrum. The analysis of the decay of these transient absorption signals allows the determination of the trapped charge carrier lifetimes. It is a real challenge to assign the optical transitions derived from the transient absorption spectra to individually excited electronic states and to determine the individual chemical identity. This can be hindered by different factors such as the broadness or the overlap of the transient absorption spectra, the simultaneous generation and trapping of holes and electrons, the different trapping sites and the sensitivity of transient absorption spectra to the experimental conditions.

However, some studies predict that the  $\cdot\text{OH}_{\text{aq}}$  radicals exhibit different transient absorption features than the  $\text{O}\cdot^-_{\text{s}}$  radicals <sup>77</sup>, with the former absorbing primarily in the ultraviolet range and the latter in the visible range. Therefore, the transient absorption in the visible range (2.5 - 2.8 eV) can be attributed to the transition from a trapped state to the conduction band forming unstable O atoms in the lattice. This would correspond to the transition  $(\text{Ti}^{\text{IV}} - \text{O}\cdot^-_{\text{s}}) - (\text{Ti}^{\text{III}} \cdot \cdot \cdot \text{O})$ . Alternatively, the observed optical transition can also be due to the electron transfer from the valence band to the trap state forming  $\text{O}\cdot^-_{\text{s}}$  radicals. Henderson *et al.* reported, however, that the latter transition may not be allowed <sup>66</sup>. Zawadzki calculated the transient absorption spectra of trapped holes in bulk anatase  $\text{TiO}_2$  and on its 001 and 101 surfaces <sup>78</sup>. According to these calculations, the transient absorption can be assigned to the  $(\text{O}^{2-} - \text{O}^-)$  transition. Depending on the distance of neighboring O atoms, the transition energy will vary, with higher transition energies corresponding to longer distances. As a result, the absorption spectra of trapped holes extend from 300 to 800 nm. Bulk trapped holes exhibit longer wavelength transient absorptions due to the fact that the difference between the strength of the hole trapping

at oxygen lattice sites in the bulk is zero while on the surface it is high, because the surface exhibits different oxygen lattice sites. Hence, no difference of the transient absorption spectra of trapped holes can be expected for different metal oxide semiconductors.

### 2.5.2.2 Electron trapping

As explained before, on *n*-type TiO<sub>2</sub>, the electrons are forced to move from the semiconductor surface to the bulk, where they can be delocalized over different Ti sites. There are many theoretical and experimental studies that favor bulk trapping over surface trapping<sup>24,74,75,79,80</sup>. However, alternative studies exist that demonstrate that Ti<sup>IV</sup> OH groups located on the surface can act as trapping centers for electrons and lead to the formation of Ti<sup>III</sup>OH species, that can attract holes and behave as recombination centers<sup>69,81</sup>. When debating if the trapping of the electrons occurs in the bulk or at the surface, the particle size must be taken into account. The upward band bending will decrease with the particle size according to the following relation<sup>82</sup>:

$$V_{BB} = \frac{kT}{6e} \left( \frac{r^0}{L_D} \right)^2 \quad 2.26$$

where  $r_0$  is the radius of the particle and  $L_D$  is the Debye length.

$$L_D = \sqrt{\frac{\epsilon kT}{en_0q}} \quad 2.27$$

In small particles, where  $r^0 \ll d_{sc}$  ( $d_{sc}$ : thickness of the space charge layer), no space charge layer or band bending exist and both electrons and holes are readily available at the surface. This results in a very broad transient absorption spectrum as can be observed in Fig. 2.9, where the transient absorption bands of electrons and holes overlap. This broad transient absorption spectrum with maximum at 650 nm is usually associated with the excitation of a trapped electron from the trapping site to the conduction band<sup>63</sup>. Peiro *et al.* studied the lifetime of trapped electrons in nanocrystalline titanium dioxide films using transient absorption spectroscopy and reported in the absence of ethanol (electron donor) and O<sub>2</sub> (electron acceptor), a half-life of its absorption signal of aprox. 25  $\mu$ s<sup>83</sup>. The corresponding decay has been attributed to:



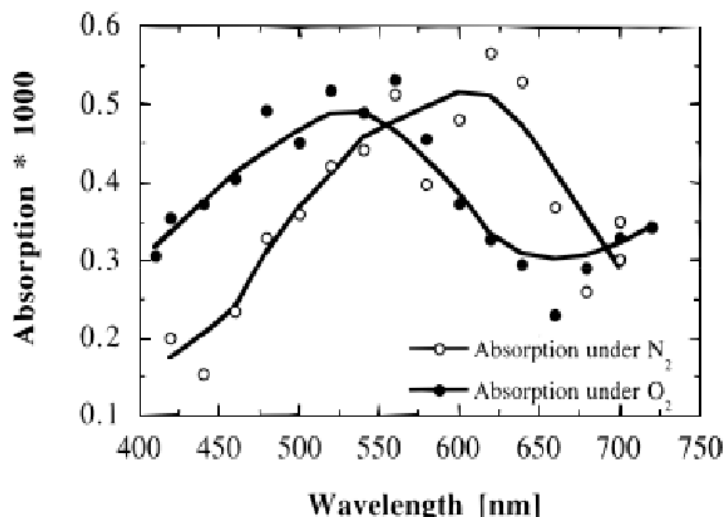


**Figure 2.9:** Transient absorption spectra measured 20 ns after laser excitation ( $\lambda_{\text{ex}}=350$  nm) in  $\text{O}_2$  saturated and  $\text{N}_2$  saturated solutions respectively:  $\text{pH} = 2.3 \cdot 10^4$  mol/L colloidal  $\text{TiO}_2$  particles, absorbed photon concentration per pulse  $9 \cdot 10^{-7}$  mol/L. <sup>63</sup>

In the presence of ethanol, the lifetime of the photogenerated electrons was found to increase up to 500 ms. The remaining  $\text{Ti}^{\text{III}}/\text{e}^-$  do not react with each other. The organic radicals formed upon the oxidation of hole scavengers are also not likely to act as acceptor for the electrons. The most likely fate of the  $\beta$ -hydroxyalkyl radicals is to inject an additional electron into the conduction band forming the respective aldehyde as product in a process called current-doubling effect (explained in detail in the discussion section). Therefore, the slow decay of  $\text{Ti}(\text{III})$  observed by Peiro *et al.* may be due to the reaction of the trapped electrons with electron acceptors that might have been already present in the  $\text{TiO}_2$  matrix, such as impurities.

### 2.5.3 Photoinduced electron transfer processes

After the formation of electron and holes by light, they can be transferred to electron and hole acceptors, provided that the energy requirements are fulfilled. The efficiency of these reactions depends on the charge-transfer rate at the interface, the recombination rate in the particle and on the transit time of the photogenerated charge carriers to the surface <sup>67</sup>. One of the firsts studies that dealt with the charge-transfer dynamics was performed by Rothenberger *et al.* using colloidal  $\text{TiO}_2$  nanoparticles <sup>84</sup>. The respective time for the electron transfer to the respective surface trap was found to be  $> 30$  ps, while the hole trapping time was around 250 ns. There is, however, discrepancy concerning electron trapping time. Furube *et al.* supposed the reason for this discrepancy to be that free electrons generated upon 355 nm excitation still contain part of the excess energy and may therefore have a higher diffusion coefficient <sup>60</sup>. Tamaki *et al.* have also shown that after reaching the surface, the photogenerated electrons migrate between surface and shallow

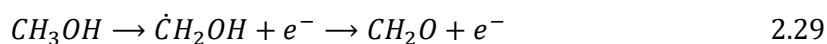
bulk trap sites that are in equilibrium <sup>60</sup>. These shallowly trapped electrons relax into deeper sites within 500 ps through hopping processes.

### 2.5.3.1 Photoinduced reduction reactions

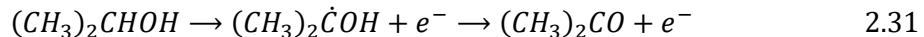
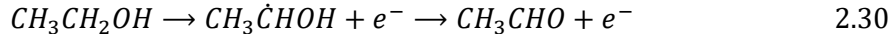
Photogenerated electrons are not directly available at the surface for the desired reactions, but TiO<sub>2</sub> could be modified to activate the photogenerated electrons for reduction reactions. This can be achieved by loading noble metal particles on the semiconductor using a photodeposition method. Noble metal modified titanium dioxide exhibits enhanced photocatalytic activity that results from an improved charge carrier separation. According to the Schottky barrier model, this enhanced charge separation can be attributed to the transfer of the photogenerated holes to the surface induced by the electric field in the space charge layer. It has been observed, that the decay rate of the transient absorption at 600 nm increases with increasing Pt-loading, indicating that a higher Pt coverage on the surface of TiO<sub>2</sub> enhances the probability of electron migration from TiO<sub>2</sub> to the surface <sup>85</sup>. These results are in good agreement with the EPR measurements, evidencing the transfer of electrons from titanium dioxide to Pt <sup>86</sup>. The electron transfer depends upon the thermodynamic driving force because the electrons have to overcome the Schottky barrier. However, it has to be said that not all electrons are transferred to the Pt and a certain number of photogenerated electrons remain in the TiO<sub>2</sub> particle <sup>86</sup>.

### 2.5.3.2 Photoinduced oxidation reactions

Organic compounds such as alcohols (methanol, ethanol, etc.), organic acids (formic acid, acetic acid, etc.) and aldehydes (formaldehyde, acetaldehyde, etc.) have been used as hole scavengers, *i.e.*, electron donors for enhancing the photocatalytic hydrogen formation <sup>6</sup>. Among different alcohols, methanol is widely used as sacrificial reagent for the photocatalytic H<sub>2</sub> formation. Methanol reacts with the photogenerated holes located in the valence band and undergoes relatively rapid and irreversible oxidation reactions <sup>87</sup>. To date, there are, however, only few studies dealing with the mechanistic aspects of the photocatalytic methanol oxidation pathway <sup>88,89</sup>. Some authors describe the photocatalytic H<sub>2</sub> evolution from aqueous methanol solutions as water splitting <sup>90-92</sup>, while others qualify the process as dehydrogenation of methanol to formaldehyde or as the reforming of methanol to carbon dioxide <sup>93-95</sup>. Tamaki *et al.* studied the reaction dynamics of the trapped holes using transient absorption spectroscopy and found that in the presence of alcohols, the transient absorption of the trapped holes presented a more rapid decay, evidencing that the trapped holes can react with the alcohols <sup>96</sup>. The lifetime of the trapped holes was found to increase with the alcohol chain length and the charge transfer rate was reported to be affected by the adsorption behavior of the alcohol to the TiO<sub>2</sub> surface. Generally, it is assumed that the hole or the •OH-induced alcohol oxidation process occurs via two reaction steps according to the following mechanism <sup>97</sup>:







The first step includes breaking a C-H bond and results in the formation of a  $\alpha$ -hydroxyalkyl radical, while the formation of the respective aldehyde occurs in the second step through the injection of an electron into the conduction band of  $\text{TiO}_2$  in a process called current doubling<sup>98-100</sup>. Morris *et al.* proposed a mechanism for the overall photooxidation of methanol<sup>101</sup> in which methanol adsorbs predominantly via a dissociative pathway at the surface of rutile  $\text{TiO}_2$  to produce surface methoxy and hydroxyl groups. These surface methoxy groups act as effective hole trapping sites upon irradiation with UV light. The hole trapping by methoxy groups lead to an effective charge separation. A two-electron transfer process involving the initial formation of a radical anion through the direct hole oxidation of a methanol molecule, followed by an electron injection from this radical anion into the  $\text{TiO}_2$  is suggested as well (current doubling process). Furthermore, the studies by Morris *et al.*<sup>101</sup> showed that the role of  $\text{O}_2$  in promoting methanol photodecomposition is to act as free electron scavenger, which opens acceptor sites for the injection of new electrons during the methoxy group oxidation.

In conclusion, the photooxidation of methanol leads to the relocation of the trapped holes and to the accumulation of electrons on the surface of  $\text{TiO}_2$  causing a downward band bending. In the absence of molecular oxygen as an effective electron scavenger, titanium dioxide changes its color from white to blue, indicating the formation of  $\text{Ti}^{\text{III}}$  centers<sup>67</sup>. The photogenerated electrons are located in the respective traps located at the surface and are available for different reduction reactions<sup>102,103</sup>. While a fast reaction of the trapped holes with different alcohol molecules on the time scale of several picoseconds has been observed, it was shown that the holes that manage to survive until the nanosecond time scale exhibit lower reactivity<sup>67</sup>. These deeply trapped holes exhibit a transient absorption maximum at 450 nm and are unable to oxidize dichloroacetate,  $\text{DCA}^-$ , nor thiocyanate,  $\text{SCN}^-$  anions. Bahnemann *et al.* concluded from these results, that only shallowly trapped holes in a thermal equilibrium with free holes are able to initiate such oxidation reactions.

#### 2.5.4 Laser flash photolysis studies on tantalates

Among the catalysts examined to date,  $\text{NaTaO}_3$  doped with lanthanum exhibited the highest quantum yield for water splitting, exceeding 50% when irradiated by UV light<sup>25,104,105</sup>. However, only little is known about the mechanisms concerning these types of semiconductors. As shown in the sections before, the photodynamics of  $\text{TiO}_2$ -based catalysts have been widely studied. Although some of the knowledge accumulated for titanium dioxide can be transferred to other catalysts, the dynamics of the photogenerated charge carriers should be studied employing the catalyst itself to promote further development towards designing and optimizing the systems.

Yamakata<sup>106</sup> studied the photodynamics of NaTaO<sub>3</sub> catalysts with different amounts of Na/Ta ratio and doped with lanthanum. In this work, impregnation with NiO was performed as well. Transient IR absorption was performed using a Q-switched Nd:YAG laser with a 266 nm pulse. A transient absorption signal was observed as can be seen in Fig. 2.10.

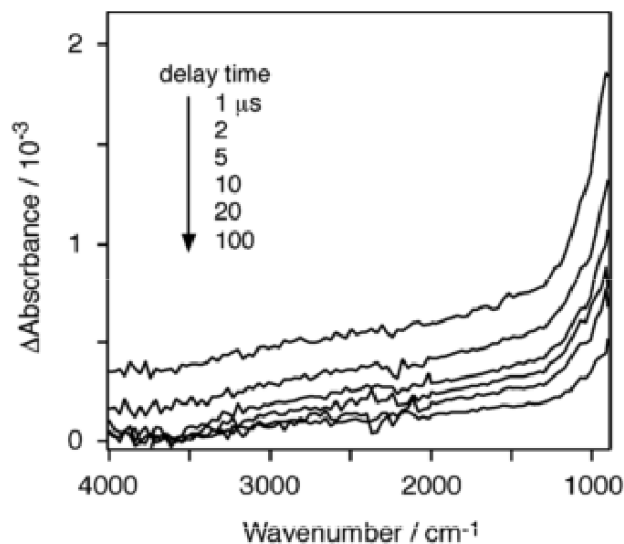


**Figure 2.10:** Transient IR absorption of NaTaO<sub>3</sub> (Na/Ta = 1.05) irradiated by a 266 nm UV pulse at 1 mJ.<sup>106</sup>

This transient absorption signal was attributed to optical transitions of electrons excited in the conduction band and then trapped in shallow mid-gap states. To evidence the assignment to the electrons in NaTaO<sub>3</sub>, the decay of the IR absorption was investigated in the presence of electron and hole scavengers, such as O<sub>2</sub> and methanol, respectively. Fig. 2.11 shows the decay of the transient absorbance at a fixed wavenumber, *i.e.*, 2000 cm<sup>-1</sup>.

The decay observed in vacuum simply reflects the recombination of the electrons and complementary holes. The decay was accelerated starting 1 μs after the laser pulse by exposure to an O<sub>2</sub> atmosphere of 10 Torr. The accelerated decay was ascribed to the electron capture by O<sub>2</sub>.



where (g) and (a) represent gas phase and adsorbed phase respectively.

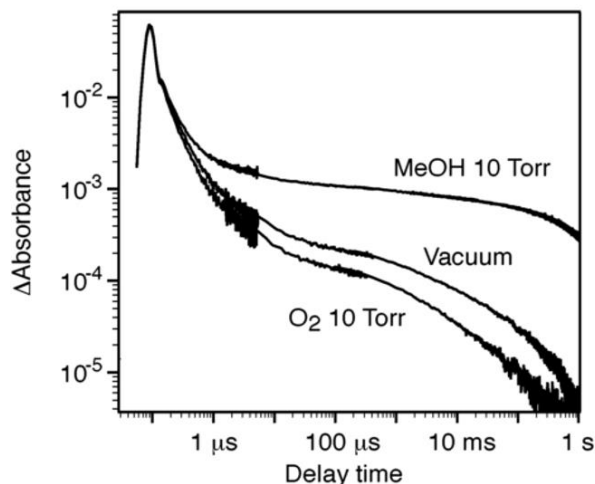


**Figure 2.11:** Temporal profiles of the transient IR absorption at  $2000\text{ cm}^{-1}$  by the irradiation of a  $266\text{ nm}$  UV pulse at  $1\text{ mJ}$ . These decay curves were obtained in vacuum and in the presence of  $10\text{ Torr O}_2$  or  $10\text{ Torr CH}_3\text{OH}$  gas. <sup>106</sup>

When the catalyst was exposed to methanol vapor of  $10\text{ Torr}$ , the decay was retarded. Holes that could otherwise recombine with the electrons were captured by a methanol-derived adsorbate (probably adsorbed methoxy).



The fact that the absorbance was nearly constant  $10\text{ }\mu\text{s}$  after the laser pulse and later indicated that the holes were exhausted within the first  $10\text{ }\mu\text{s}$ . The IR absorption responded to the composition of the reactant vapor as expected upon the assignment of the transition at  $2000\text{ cm}^{-1}$  to the excited electrons. This assignment claimed, on the other hand, that holes photogenerated in the valence band (VB) do not absorb mid-IR light. The absence of any hole-induced transient absorption is rationalized when the mid-gap states trapping the holes are energetically deep as in the case of  $\text{TiO}_2$  catalysts. Holes trapped at such deep mid-gap states can neither be thermally excited to the VB nor absorb mid-IR light via any direct optical transitions. Therefore, the absorbance at  $2000\text{ cm}^{-1}$  is interpreted to be the relative number of excited electrons in  $\text{NaTaO}_3$ -based catalysts.

Another aspect investigated in this work was the doping of  $\text{NaTaO}_3$  with lanthanum. When the catalyst with a  $\text{Na}/\text{Ta}$  ratio =  $1.05$  was doped with La of  $1$  and  $2\text{ mol}\%$  its  $\text{H}_2$  production activity was improved by  $3.3$  and  $2.6$  times. Further doping reduced the activity to almost the original value of the undoped photocatalyst.

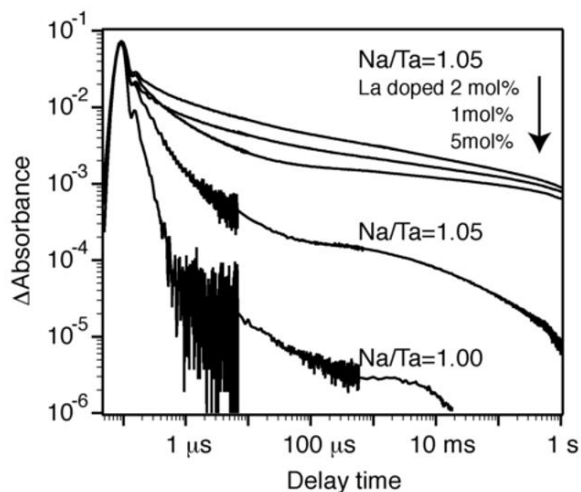


**Figure 2.12:** The decay of photogenerated electrons on  $\text{NaTaO}_3$  ( $\text{Na}/\text{Ta} = 1.00$ ),  $\text{NaTaO}_3$  ( $\text{Na}/\text{Ta} = 1.05$ ) and La-doped  $\text{NaTaO}_3$  ( $\text{Na}/\text{Ta} = 1.05$ ) in vacuum. A 266 nm UV pulse was used to irradiate the photocatalyst and the transient absorption was observed at  $2000 \text{ cm}^{-1}$ .<sup>106</sup>

As Fig. 2.12 shows, the La doping with 1 and 2 mol% enhanced the IR absorption, while doping with 5 mol% partially reduced the absorbance. The optimized doping of La hindered the recombination and increased the population of excited electrons.

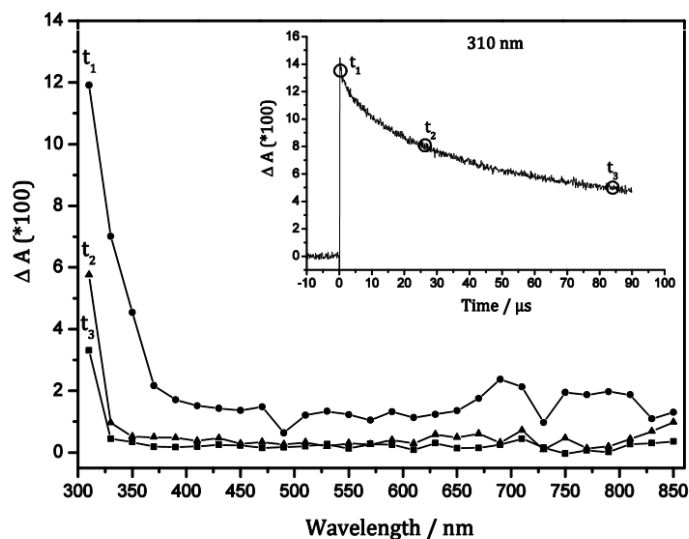


**Figure 2.13:** Transient absorption spectra of pure  $\text{NaTaO}_3$  taken at three different times ( $t_1=0.34 \mu\text{s}$ ,  $t_2=25 \mu\text{s}$  and  $t_3=85 \mu\text{s}$ ) after band-gap excitation at laser  $\lambda_{\text{ex}}=248 \text{ nm}$ . The inset shows the transient absorption measured at the absorption maximum at 310 nm indicating  $t_1$ ,  $t_2$  and  $t_3$ . The powder was purged for  $\frac{1}{2} \text{ h}$  with  $\text{N}_2$  prior to the measurement

18.

More recently in the work of Ivanova<sup>18</sup>, results of laser flash photolysis of undoped and 0.83 wt.% La doped NaTaO<sub>3</sub> can be found. The inset of Fig. 2.13 illustrates the decay of the transient absorption signal at 310 nm of bare NaTaO<sub>3</sub> after band gap excitation with a laser irradiation wavelength of 248 nm. The signal at 310 nm does not reach zero within measured period of time, indicating stable and long-lived species<sup>18</sup>. Fig. 2.13 shows the transient absorption spectra of bare NaTaO<sub>3</sub> taken at three different times ( $t_1=0.34 \mu\text{s}$ ,  $t_2=25 \mu\text{s}$  and  $t_3=85 \mu\text{s}$ ).

By analogy to the well-investigated TiO<sub>2</sub> the highest absorption value at 310 nm could be attributed to the trapped holes of undoped NaTaO<sub>3</sub>. In order to verify this assumption, methanol acting as hole scavenger was added to the system. Fig. 2.14 shows the decay of the signals at 310 nm after addition of different amounts of methanol. Obviously, with increasing methanol amount in the system, the signals decay faster. After addition of 100  $\mu\text{l}$  of methanol, the signal at 310 nm disappears after 40  $\mu\text{s}$ . These results confirm the fact that the detected signal at 310 nm can really be attributed to the trapped holes of bare NaTaO<sub>3</sub><sup>18</sup>. Moreover, it is obvious that in the case of NaTaO<sub>3</sub> the photogenerated holes are first trapped and do not immediately react with adsorbed methanol molecules since the initial intensity of the signal stays constant in the case of different amounts of methanol added to the system (see Figure 2.14).

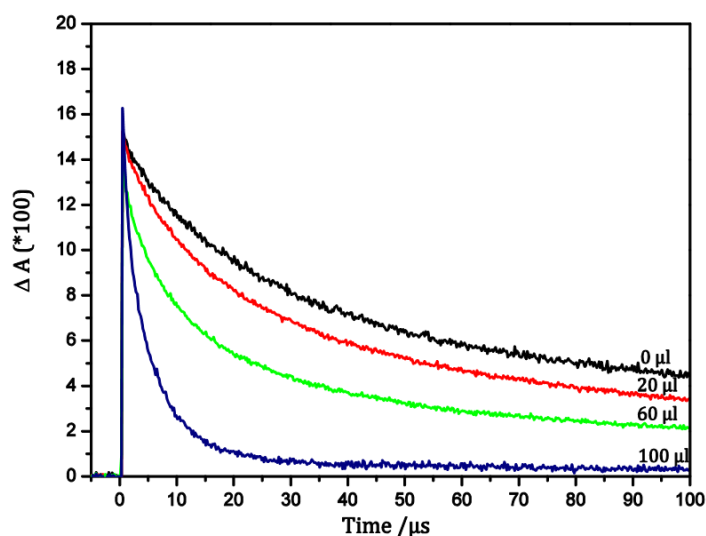


**Figure 2.14:** Transient absorption of the photogenerated holes at  $\lambda=310 \text{ nm}$  of pure NaTaO<sub>3</sub> in the absence and presence of different amounts of methanol (20, 60 and 100  $\mu\text{l}$ ) after laser irradiation at 248 nm. All powders were purged for  $\frac{1}{2}\text{h}$  with N<sub>2</sub> prior to the measurement<sup>18</sup>.

Fig 2.15 shows the transient absorption spectra of La-doped NaTaO<sub>3</sub> (0.83 wt.% La) at three different times ( $t_1=0.34 \mu\text{s}$ ,  $t_2=25 \mu\text{s}$  and  $t_3=85 \mu\text{s}$ ) after band-gap excitation with a laser irradiation wavelength of 248 nm. The inset of Fig. 2.15 demonstrates the transient absorption signal at 310 nm indicating  $t_1$ ,  $t_2$  and  $t_3$ <sup>18</sup>.

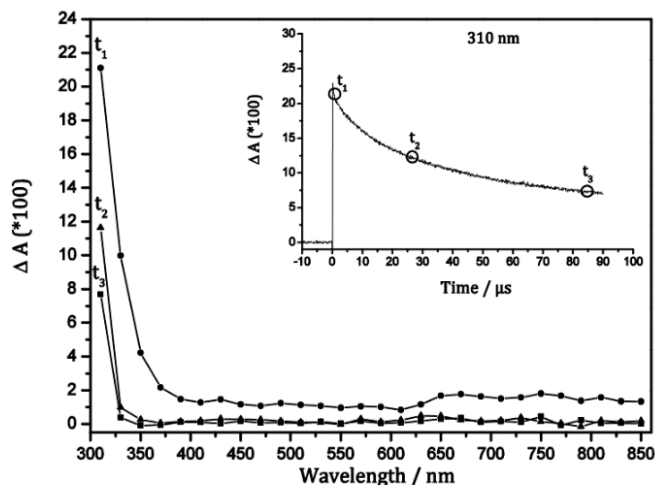


**Figure 2.15:** Transient absorption spectra of La-doped  $\text{NaTaO}_3$  (0.83 wt% La) taken at three different times ( $t_1=0.34 \mu\text{s}$ ,  $t_2=25 \mu\text{s}$  and  $t_3=85 \mu\text{s}$ ) after band-gap excitation at laser  $\lambda_{\text{ex}}=248 \text{ nm}$ . The inset shows transient absorption measured at the absorption maximum at 310 nm indicating  $t_1$ ,  $t_2$  and  $t_3$ . The powder was purged for  $\frac{1}{2} \text{ h}$  with  $\text{N}_2$  prior to the measurement<sup>18</sup>.

Both the transient absorption spectra and the decay of the signal at 310 nm are very similar to those measured in the case of undoped  $\text{NaTaO}_3$ . By analogy to the bare  $\text{NaTaO}_3$  the highest absorption value at 310 nm can also be attributed to the photogenerated holes. The initial intensity of the transient absorption signals shown in Fig. 2.15 is higher as that detected in the case of undoped  $\text{NaTaO}_3$  under identical conditions. Apparently, the higher intensity of the signals correlates with a higher density of the photogenerated charge carriers (holes) in the system<sup>18</sup>.

## 2.6 Electron paramagnetic resonance (EPR)

Electron paramagnetic resonance (EPR) is a widely used spectroscopic technique to study paramagnetic centers on various oxide surfaces, which are frequently encountered in heterogeneous catalysis. These observable paramagnetic centers may include surface defects, inorganic or organic radicals, metal cations or supported metal complexes or clusters. Each of these paramagnetic species will produce a characteristic EPR signature with well-defined spin Hamiltonian parameters. However, the magnetic properties, stability and reactivity of these centers may vary dramatically depending on the nature of the support or the measurement conditions<sup>107</sup>. The existence of two Zeeman levels and the possibility of inducing transitions from the lower energy level to the higher energy level is the basis of EPR spectroscopy. The resonance experiment can be conducted in two ways; either the magnetic field is kept constant and the applied frequency varied or the applied frequency is held constant and the magnetic field is varied. In EPR spectroscopy, the latter case is usually used since it is easier to vary the magnetic field over a wide range than the frequency<sup>107</sup>.

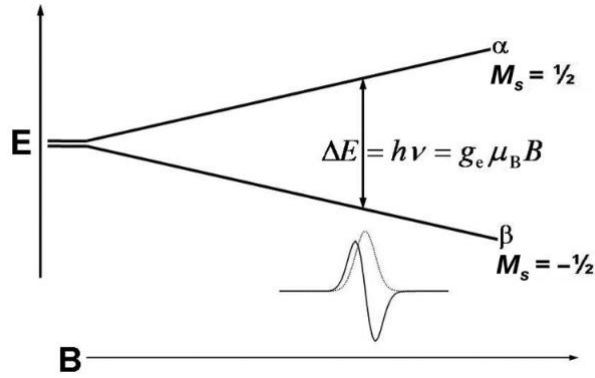


**Figure 2.16:** Energy levels for an electron spin ( $S = \pm 1/2$ ) in an applied magnetic field  $B$

At thermal equilibrium and under the influence of external applied magnetic field, the spin population is split between the two Zeeman levels (see Fig. 2.16) according to the Maxwell-Boltzmann law:

$$\frac{n_1}{n_2} = e^{\frac{-\Delta E}{kT}} \quad 2.34$$

where  $k$  is the Boltzmann constant,  $T$  the absolute temperature and  $n_1$  and  $n_2$  the spin populations characterized by the  $M_s$  values of  $+1/2$  and  $-1/2$  respectively. At 298 K in a field of about 3000 G the distribution shows that:

$$\frac{n_1}{n_2} = e^{\frac{-\Delta E}{kT}} = e^{\frac{-g_e \mu_e B}{kT}} \quad 2.35$$

This gives a value of  $n_1/n_2 = 0.9986$ . The populations of the two Zeeman levels are therefore, almost equal, but the slight excess in the lower level gives rise to a net absorption. However, this would very quickly lead to the disappearance of the EPR signal as the absorption of energy would equalize these two states. Consequently, there has to be a mechanism for energy to be lost from the system. Such mechanisms are known as relaxation processes.





## 3. Materials and methods

### 3.1 Materials

In this work NaTaO<sub>3</sub> powders, bare and with different lanthanum doping (0.57, 0.83 and 1.11 wt.% La) were investigated. The materials were synthesized by the company H.C. Starck located in Goslar (Germany). The chosen synthetic route was a solid-state reaction as described by A. Kudo<sup>25</sup>. For preparing the bare material, Ta(OH)<sub>5</sub> and Na<sub>2</sub>CO<sub>3</sub> were mixed together and for the synthesis of the lanthanum doped powders, addition of La<sub>2</sub>(CO<sub>3</sub>)<sub>3</sub> · 5H<sub>2</sub>O was carried out. The products were dried at 105°C for 16h. Next, the educts were thoroughly grinded and calcinated at 800°C for 3h and a second grinding was performed. The delivered materials contained different amounts of lanthanum doping (0.57, 0.83 and 1.11 wt.% La). The lanthanum content in the powders was determined using a fusion process with K<sub>2</sub>S<sub>2</sub>O<sub>7</sub>. The final determination of lanthanum doping was made by means of inductively coupled plasma atomic emission spectroscopy (IPC-OES, Ultima 2, Horiba Jobin Yvon) against a cross calibration. The solvents were all purchased from the company Sigma-Aldrich and were used without further purification.

### 3.2 Photodeposition experiments

For the introduction of small noble metal islands in the system, the photodeposition method described by Kato *et al.* in<sup>25</sup> was employed. A 0.5 M aqueous suspension of NaTaO<sub>3</sub> was prepared. The suspension was sonicated for approx. 20 min, until all the material was homogeneously distributed. The solution was then transferred to a 100 cm<sup>3</sup> double jacket quartz glass reactor. Methanol (2 ml) and an aqueous solution of H<sub>2</sub>PtCl<sub>6</sub> · H<sub>2</sub>O 0.01 M (7.7 ml) were added into the reactor. The inside of the reactor was purged with a continuous flow of argon (35 ml / min) for 15 min. Subsequently, the Ar flow was reduced to 10 ml / min while the suspension was magnetically stirred during 1 h in the dark to establish adsorption equilibrium. The sample was irradiated afterwards for 3 h with a 1000 W xenon arc lamp. To maintain the desired temperature of 25°C the double jacket quartz reactor was cooled with water. The Pt-modified NaTaO<sub>3</sub> was separated by centrifugation, washed with distilled water repetitively and dried in a dry chamber overnight. The powders were stored in closed glass containers at ambient conditions. The amount of Pt photodeposited was 0.1 wt.% for all experiments showed in this work. Higher amounts of loading have been investigated but as the powders became grey with increasing loading percentage, the results cannot be compared with the bare powders which have a white color.

### 3.3 Material characterization methods

#### 3.3.1 Specific surface area measurements (BET)

Single-point standard BET measurements were performed using a Flowsorb II 2300 instrument (Micrometrics, USA). The gas mixture used for the adsorption determinations was composed of 30 % N<sub>2</sub> and 70 % He. The samples were previously heated to 120 °C

during 1 h, ensuring a water and organic free surface for the measurements. The determination of the BET surface area of the materials is based on the multi-layer absorption model developed by Brunauer-Emmett-Teller <sup>108</sup>.

#### 3.3.2 Scanning electron microscopy

Scanning electron microscopy (SEM) measurements were carried out with a JEOL JSM6700F emission instrument operated at an acceleration voltage of 2.0 kV and using a secondary electron detector (SE). A tungsten single crystal filament was used as an electron source. In order to prevent distortions due to the accumulation of charge in the sample, it is important that electrical contact is maintained between the sample surface and the sample holder. For this reason, the samples were prepared by deposition of NaTaO<sub>3</sub> powders onto electrically conducting glass FTO (details concerning the deposition method can be found in the chapter about electrode preparation.)

#### 3.3.3 Raman spectroscopy

Raman spectroscopic measurements were performed using a Bruker Optics IFS66v/s FTIR spectrometer equipped with a FRA-106 Raman attachment. The Raman laser power was 5 mW. For each spectrum, 10 scans were measured and accumulated for a better resolution.

#### 3.3.4 Diffuse reflectance spectroscopy

Diffuse reflectance spectroscopy of the powders and films was performed on a Varian Cary 100 Scan UV-Vis spectrophotometer equipped with a diffuse reflectance accessory. The measurements were performed in a wavelength range from 200 nm to 800 nm using an integrating sphere. Barium sulfate was employed as a reference material to provide a nominal 100% reflectance measurement. Reflectance was converted by the instrument software to F(R) values according to the Kubelka-Munk equation. The band gap was obtained by a plot of the modified Kubelka-Munk function versus the energy of the exciting light.

$$E = \frac{hc}{\lambda} \quad 3.1$$

with  $c = 3 \cdot 10^8$  m/s being the light speed in vacuum and  $h = 4.136 \cdot 10^{-15}$  eV · s Planck's constant.

### 3.4 Electrode preparation

#### 3.4.1 Screen printing paste preparation

0.5 g of the semiconductor powder (bare or La-doped NaTaO<sub>3</sub>) were thoroughly grinded in a mortar. Additions of small amounts of distilled water and ethanol were performed whilst grinding. The mixture was then transferred to a round flask and  $\alpha$ -terpineol was added before the introduction in an ultrasonic bath for 15 min. Next, an ethyl cellulose solution was incorporated and left to sonicate again for another 15 min. To ensure that the paste is really smooth and no agglomerations of material are present, it was sonicated for another

15 min before evaporating the ethanol using a rotary evaporator. The prepared paste was stored in closed glass containers at ambient conditions.

#### 3.4.2 Electrode coating

Once the paste has been prepared, the electrodes have to be coated. As support material, fluorine doped tin oxide (FTO) glass was employed. The FTO glass was purchased from Sigma-Aldrich and has a surface sheet resistance of  $\sim 0.75 \Omega/\text{m}^2$ . The glass plates were cut to 3 x 3 cm pieces in order to fit the window of the electrochemical cell. The FTO glass was coated on the conductive side using a screen printing frame that has attached a mesh of 80T (medium thread diameter) and that has a stencil of 2 x 2 cm for coating. The mesh was placed on top of the FTO glass ensuring that the stencil was in the middle of the glass piece. It is important that the electrodes have a frame around without coating for better contact with the electrochemical cell. A close-up of the contact between the working electrode and the photoelectrochemical cell can be seen in Fig. 3.1.

A small amount of paste was added to the top section of the stencil and using a thick rubber squeegee the paste was dragged down until the electrode was coated trying to keep a constant pressure in the process. Next, the electrode was separated from the mesh very carefully and the squeegee and mesh were cleaned with some isopropanol in order to remove the excess paste. The electrode was placed onto a heat plate and calcinated at  $400^\circ\text{C}$ . During calcination, the electrode dried to a very dark brown color and after it became white again, was left to cool down. The process of coating and calcination on the heat plate was carried out three times for each electrode, to ensure that the coatings were completely opaque. After the three coatings were done, the electrode was calcinated in an oven at  $500^\circ\text{C}$  for 1h.

#### 3.5 Flatband potential measurements

The flatband potentials were measured by means of impedance spectroscopy using Mott-Schottky plots. The photoelectrochemical measurements were performed using a Zahner IM6 electrochemical workstation and a xenon arc lamp (100 Watt) as light source. A Zahner PP211 potentiostat was connected to the electrochemical workstation and the photoelectrochemical cell. The electrodes were placed inside the photoelectrochemical cell consisting of an Ag / AgCl (KCl 3.0 M) reference electrode ( $-0.20 \text{ V vs. NHE}$ ), a  $\text{NaTaO}_3$  electrode as the working electrode, and a platinum coil as the counter electrode. An illustration of the photoelectrochemical cell can be seen in Fig. 3.1. The cell body was made from polychlorotrifluoroethylene (PCTFE) and was equipped with a transparent quartz window with a diameter of 18 mm. The Pt coil was already inserted inside the cell body around the window and the working electrode was placed in the back side. The measurements were performed in aqueous KCl 0.1 M solutions at pH 7.0. The potential was systematically varied from  $-1.0$  to  $+1.0 \text{ V}$  with the frequency being modulated from 10 to 1000 Hz.

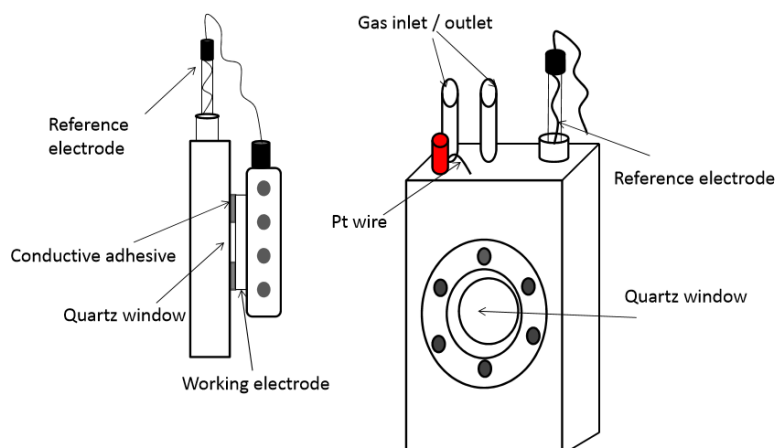


**Figure 3.1:** Photoelectrochemical cell (PEC) front and side view.

### 3.6 Photocatalytic H<sub>2</sub> production

The photocatalytic reactions were performed in a 100 cm<sup>3</sup> double jacket quartz glass photoreactor. The used setup consisted of a gas supply connected to a mass flow controller (MFC) which allowed to control the Ar flow that was continuously purged through the system. For gas analysis a quadrupole mass spectrometer (QMS) (Hidden HPR-20) was employed. A schematic presentation of the experimental setup can be observed in Fig. 3.2.

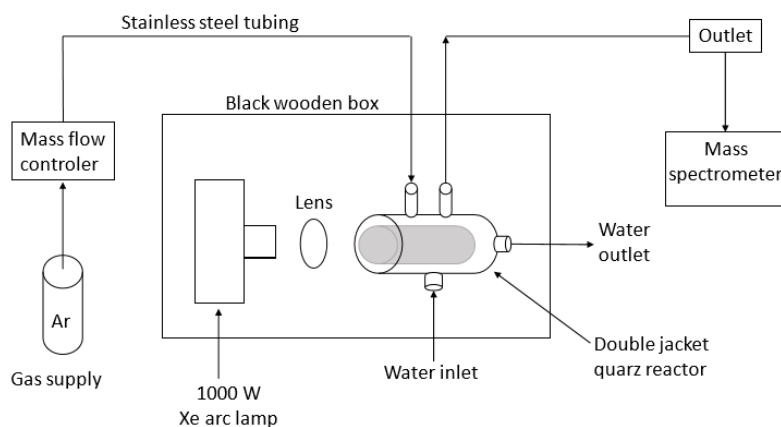


**Figure 3.2:** Experimental setup for the measurement of molecular hydrogen evolution.

For the experiments, 50 mg of the photocatalyst was suspended in 50 ml of an aqueous methanol solution (0.03 M) by sonication. The suspension was transferred into the photoreactor and purged with Ar for 20 min to remove any dissolved O<sub>2</sub>. Afterwards, the reactor was connected to the mass flow controller and the QMS through metal flanges. To

remove air in the headspace of the photoreactor, an Ar gas stream of 50 cm<sup>3</sup>/min was continuously purged through the reactor before illumination, until no traces of molecular oxygen and nitrogen could be detected. The inlet flow rate/gas consumption by the QMS is 1 cm<sup>3</sup>/min and the excess gas is directed towards the exhaust. The sampling rate of the QMS is in the millisecond range, thus allowing a fast tracking of the reaction. During the photocatalytic test the Ar flow was adjusted to 10 cm<sup>3</sup>/min. Before starting the illumination, the system was left in the dark for 40 min to ensure the stabilization of the system background and to record the baseline. Afterwards, the reactor was irradiated during 5-6 h from the outside using an Osram XBO 1000 W xenon lamp in a Müller LAX 1000 lamp housing. A 320 nm cut off filter was placed between the lamp and the photoreactor in order to let monochromatic light through. During the irradiation time the photocatalytically formed gases were monitored continuously in time intervals of approx. 30 s. After the irradiation the lamp was switched off allowing the system to reach the baseline again. The temperature of the reaction was kept constant during the whole experiment using a thermostatic bath (Julabo Company). For the quantitative analysis of molecular hydrogen, the QMS was calibrated employing standard diluted H<sub>2</sub> in Ar (Linde Gas Company, Germany).

### 3.6.1 Determination of the quantum yield

The photocatalytic activity of bare and modified La-doped NaTaO<sub>3</sub> was assessed by the determination of the quantum yield,  $\phi$ , of hydrogen and oxygen evolution from water, aqueous methanol, and silver nitrate solutions. Accordingly the quantum yield  $\phi$  is defined as <sup>109</sup>:

$$\phi = \frac{r}{I_a} \quad 3.2$$

$$I_a = I_0 \cdot F_s \quad 3.3$$

where  $r$  is the photocatalytic H<sub>2</sub> or O<sub>2</sub> evolution rate.  $I_a$  and  $I_0$  are the absorbed and the incident photon fluxes, respectively.  $I_0$  was determined by integration of irradiance of the lamp in the range of 250-400 nm.  $F_s$  is the integrated absorption fraction of the semiconductor particles over the range from  $\lambda_1 = 250$  to  $\lambda_2 = 400$  nm:

$$F_s = \frac{\int_{\lambda_1}^{\lambda_2} I_\lambda T_\lambda^f f_\lambda^s d\lambda}{\int_{\lambda_1}^{\lambda_2} I_\lambda T_\lambda^f d\lambda} \quad 3.4$$

where  $I_\lambda$  is the irradiance in the wavelength range  $d\lambda$ ,  $T_\lambda^f$  is the transmittance of the media between the light source and the reaction suspension. Since no filter was used and the reactor was made from quartz,  $T_\lambda^f$  was assumed to be unity:

$$f_\lambda^s = 1 - T_\lambda^s = 1 - 10^{-A_\lambda^s} \quad 3.5$$

where  $f_\lambda^s$  is the fraction of light absorbed at the wavelength  $\lambda$ .  $T_\lambda^s$  and  $A_\lambda^s$  are the transmittance and absorbance respectively of the sample at the wavelength  $\lambda$ .

Fig. 3.3 (left axis) shows the absorbance  $A_{\lambda}^s$  of suspended La-doped NaTaO<sub>3</sub> particles in the wavelength range from 250 to 400 nm measured by means of an UV-vis spectrophotometer (Cary 1000) equipped with an integrating sphere. The irradiance  $I_{\lambda}$  of the 1000 W Xe arc lamp (right axis) used for the photocatalytic tests was measured by a radiometer (BW Tek Company) and the obtained spectrum is also shown in Figure 3.3 (right axis) <sup>18</sup>.

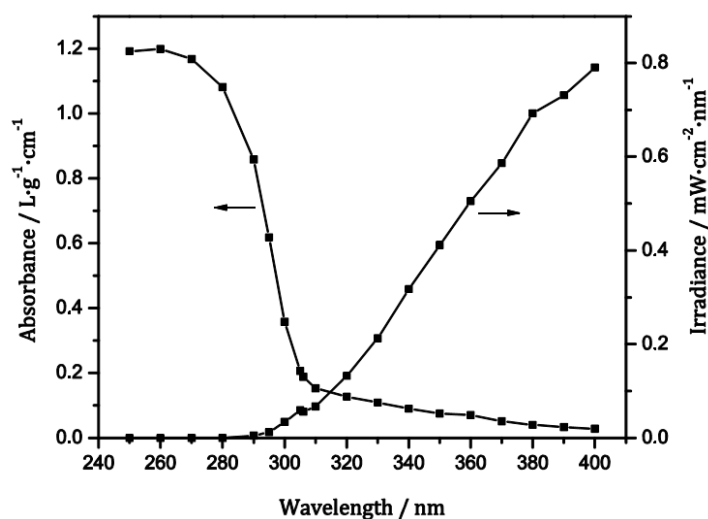


**Figure 3.3:** Absorption spectrum of suspended La-doped NaTaO<sub>3</sub> particles in water (left) and irradiance of a 1000 W Xe arc lamp (right) in the range of 250 to 400 nm <sup>18</sup>.

The absorption property of suspended La-doped NaTaO<sub>3</sub> particles was examined in the wavelength range from 250 to 400 nm. For this purpose, the absorption of several La-doped NaTaO<sub>3</sub> suspensions prepared in different concentrations was measured. The obtained absorption values at appropriate wavelengths were plotted versus the different concentrations of the suspensions. After linear regression the determined slopes of these curves were plotted versus the corresponding wavelengths (Fig. 3.3 left axis). Fig. 3.3 clearly shows that a rather small part of the light provided by the employed xenon lamp can be absorbed by the investigated La-doped NaTaO<sub>3</sub> particles <sup>18</sup>.

The absorption property of suspended TiO<sub>2</sub>-P25 particles as a reference material was examined in the wavelength range from 295 to 450 nm (Fig. 3.4). The quantum yields were determined by analogy to the La-doped NaTaO<sub>3</sub> system in the wavelength range from 295 to 450 nm <sup>18</sup>.

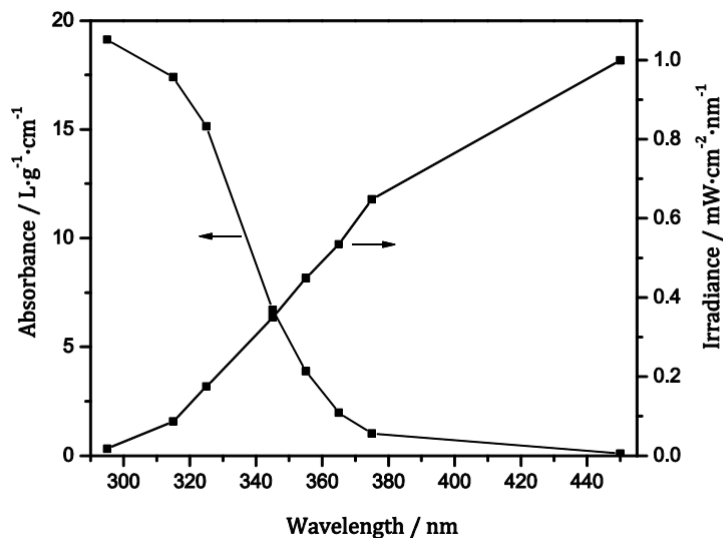


**Figure 3.4:** Absorption spectrum of suspended TiO<sub>2</sub> -P25 particles in water (left) and irradiance of a 1000 W Xe arc lamp (right) in the range of 295 to 450 nm<sup>18</sup>.

### 3.7 Laser flash photolysis measurements

For the time-resolved transient diffuse absorption study of the photogenerated charge carriers, their recombination and trapping laser flash photolysis investigations were carried out using a laser flash photolysis spectrometer LKS 80 (Applied Photophysics). The system used and illustrated in Fig. 3.5, was composed of an excimer laser head (LPX 200 from Lambda Physik), which can work at different wavelengths depending of the gas mixture used to fill the laser. The laser beam has to be redirectioned in order to achieve the correct angle to hit the sample and for this purpose a Pellin-Broca prism steering module was used. As analyzing light source, a 150 Watt xenon arc lamp mounted in a convection cooling housing, was used which directly illuminated the sample holder. In the front and back of the sample holder light filters were employed in order to protect the detector. In this work, the laser flash photolysis measurements were performed directly with powders, therefore, a diffuse reflectance accessory was used. This accessory consisted of a sample holder and an optical beam steering module with the function of redirecting the incoming xenon light beam (via two plane folding mirrors) so that is parallel to the main optical axis. A Spectrosil lens then focuses the optical beam onto the solid sample. The function of the second lens mounted on the optical module is to collect diffused reflected light and to generate a converging beam, which is redirectioned by the third folding mirror back onto the main optical axis within the sample housing. This converging beam is redirectioned to the monochromator. Finally, for signal detection a photomultiplier (Hamamatsu R928) housing is attached to the exit light port of the monochromator. The photometric light level reaching the photomultiplier has to be constant and was kept at 100 mV for all measurements. The

current output was terminated by a variable signal terminator (set to  $100\ \Omega$ ) inserted onto the signal input socket of the digital oscilloscope.

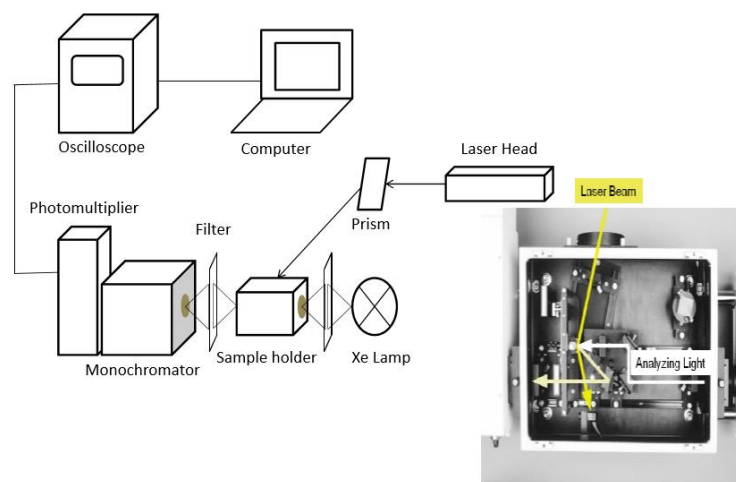


**Figure 3.5:** Experimental setup for the laser flash photolysis investigations.

In this thesis, laser flash measurements were performed using two different exciting wavelengths ( $\lambda$ ) such as 248 nm in which a KrF gas mixture was used, and 351 nm which can be achieved filling the laser with a mixture of XeF. The laser repetition frequency was 10 Hz and the pulse duration was 20 ns. After a ferrioxalate actinometry<sup>110</sup> was performed for both wavelengths, a laser beam energy of 16 mJ was calculated for 248 nm and 2.7 mJ for 351 nm, using 1.15 as the quantum yield for  $\text{Fe}^{\text{II}}$  formation<sup>111</sup>. The experiments were performed using directly the provided powders and using a quartz cuvette with an area of  $1\ \text{cm}^2$ . The samples were purged with different gases to investigate the effect of different atmospheres on the photogenerated charge carriers.

In order to convert the voltage signal that describes the transient absorption into absorbance against time, the amplitude of the analyzing light is required together with a baseline trace (obtained under identical conditions as for the transient data record but with the laser prevented from reaching the sample). The data set holding the baseline information is usually subtracted from the data set that describes the transient change. Therefore, the data points are converted into absorbance values according to eq. 3.6:

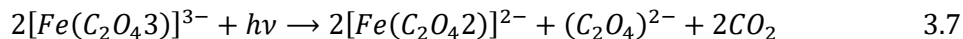
$$J = \log \frac{I_0}{I_t} \quad 3.6$$

with  $J$  being the absorbance (arbitrary units),  $I_0$  the analyzing light level, and  $I_t$  light transmitted by an absorbing sample.

The photon flux has been determined using a chemical ferrioxalate actinometer<sup>110,111</sup>. Briefly, freshly prepared 100 ml iron (III) sulphate aqueous solution (0.15 M) and 100 ml potassium oxalate aqueous solution (0.15 M) have been mixed in the dark. Afterwards, 0.5 ml of  $\text{H}_2\text{SO}_4$  aqueous solution (0.05 M) has been added to the flask. The final volume was adjusted to 200 ml. Under these conditions the green colour of the ferrioxalate complex is formed. Aliquots of 10 ml were taken and introduced in different volumetric flasks. Addition



of the developers: 0.05 % phenantroline (2 ml), sodium acetate (0.75 M) and 1.2 ml of  $H_2SO_4$  (0.2 M) was carried out in the dark. Next, irradiation of 3 ml of the prepared mixture with the laser using 15 shots each time was carried out. For each cuvette a different laser energy was used. The ferrioxalate complex absorbs all photons of the incident light and is reduced to an iron (II) complex, according to the following equation <sup>112</sup>:



After irradiation, 1 ml of NaF was added and the rate of iron (II) complex formation was calculated by determining the amount of iron (II) ions after irradiation with different laser energies using UV-Vis spectroscopy. The photon flux was calculated by dividing the rate of iron (II) formation by the quantum yield of the iron (II) (1.15 <sup>110</sup>) at the applied conditions.

### 3.8 Electron paramagnetic resonance (EPR)

The EPR measurements were performed at the University of Aberdeen using a JEOL JES-FA 200 ESR spectrometer equipped with a JEOL X-band microwave unit operating at 9.1 GHz. The samples were cooled to 80 K with Oxford instruments ESR 900 cryostat running with liquid nitrogen. The samples were irradiated with a 450 W LOT-Oriel GmbH light source, equipped with a water filter to remove infrared irradiation from the broadband irradiation (approximately 200-900 nm). For some experiments a pyrex filter to cut off the hard UV light was used (cut off at 320 nm). 100 mg of sample was used for each measurement and all the samples were studied at high vacuum, with a minimum of 1h evacuation in a high vacuum EPR cell, using an Edwards  $\chi$ DS5 turbomolecular pump in an organic molecule free vacuum line. In order to ensure no interference from atmospheric gases, the evacuation pressure was always less than  $3 \cdot 10^{-6}$  mbar prior to the sample measurement by measuring the pressure of the vacuum line with a Kurt J Lesker Company, KPDR900 pressure meter. The same type of meter was also used for adding known quantities of molecular oxygen into the sample. For the experiments with methanol, a glass vacuum line with grease fittings was used. The vacuum line is used for many organic experiments and hence perfect absence of interfering organic molecules cannot be ensured. 100 mg of sample were introduced into a quartz EPR tube with grease fittings instead of free o-rings, and evacuated overnight. The next morning, it was subjected to saturated vapor pressure of freeze pumped methanol for 2h prior to the measurement. The g-values were calculated from the observed field strength of the signal according to:

$$g = \frac{hv}{\mu_B B_0} \quad 3.8$$

With  $h$  being the Planck constant,  $\nu$  the frequency,  $\mu_B$  Bohr's magneton and  $B_0$  the applied magnetic field.



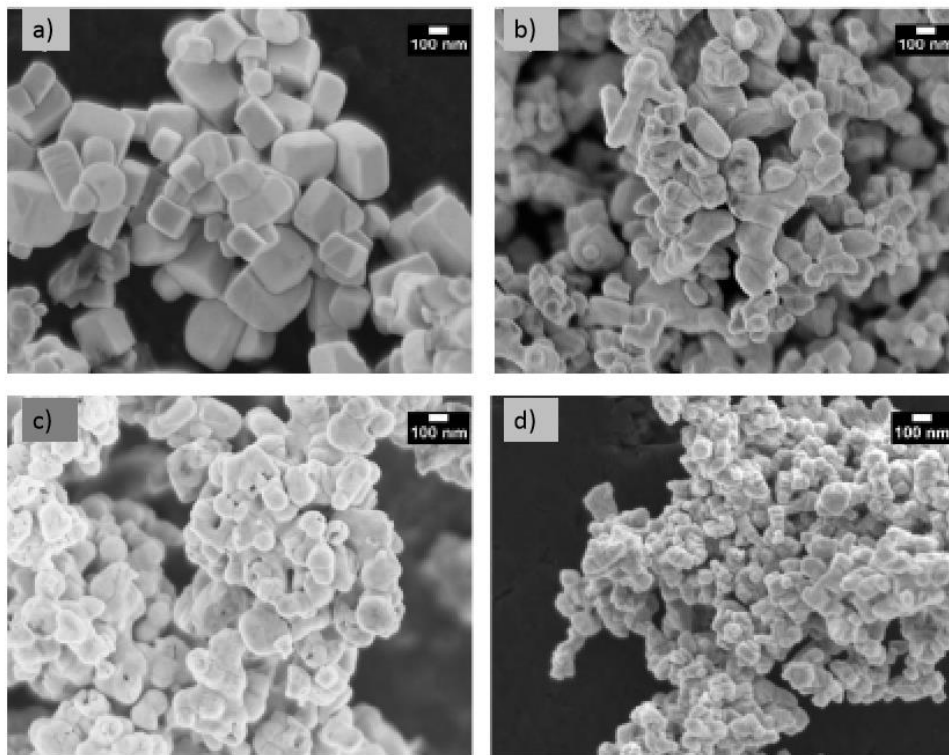
## 4. Material characterization

In this chapter, the characterization of the investigated materials is shown. Different methods and techniques have been employed in order to study the properties of the undoped and of the lanthanum doped  $\text{NaTaO}_3$  both as powder and as film.

### 4.1 Scanning electron microscopy

#### 4.1.1 Powders

The surface morphology of bare and lanthanum doped  $\text{NaTaO}_3$  powders was investigated by scanning electron microscopy.



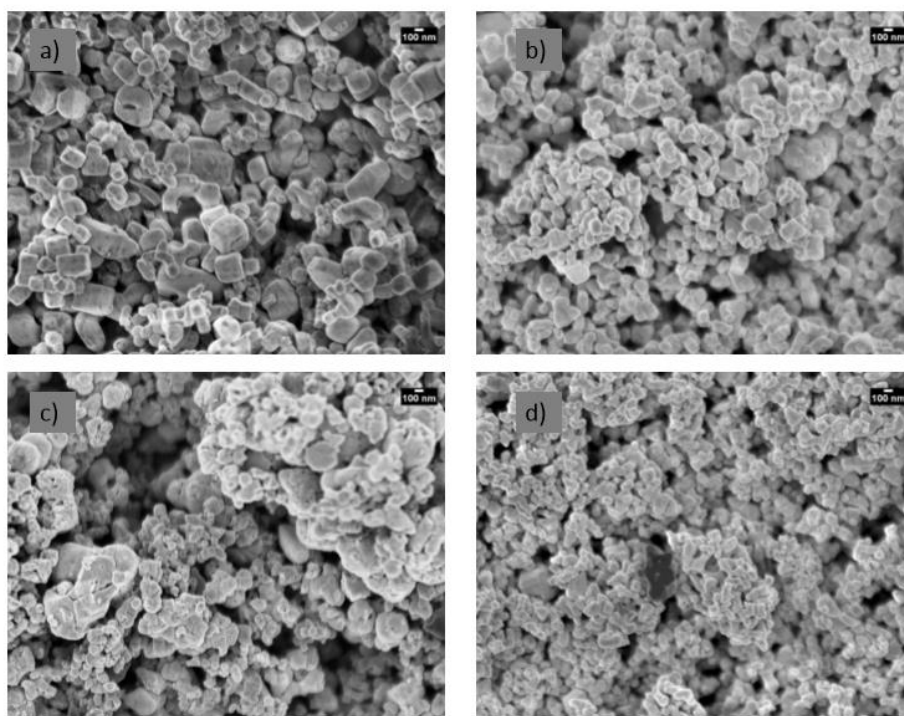
**Figure 4.1:** Scanning electron micrographs (SEM) for the (a) Bare  $\text{NaTaO}_3$ , (b) 0.57 wt.% La, (c) 0.83 wt.% La and (d) 1.11 wt.% La powders.

Fig. 4.1 shows the results of SEM measurements of the powders taken with a 50.000x resolution. As it can be seen, the structure of bare  $\text{NaTaO}_3$  exhibits an inhomogeneous distribution of particles of different shapes and sizes (from 100 to 250 nm) showing in some cases a very defined rectangular shape. It is obvious that La-doping has a huge impact on the particle morphology and affects both shape and size of the particles. A 0.57 wt.% La-doping leads to an increase in the particle irregularities and no particles with rectangular shape can be observed anymore. A higher La-doping of 0.83 wt.% La increases these

irregularities even further. Lastly, with 1.11 wt.% La-doping the irregularity decreases and particles with more defined shape can be observed. La-doped  $\text{NaTaO}_3$  shows a broad particle size distribution with smaller particles than the bare material (80 to 150 nm).

### 4.1.2 Electrodes

The obtained SEM micrographs for the electrodes prepared using bare and lanthanum doped  $\text{NaTaO}_3$  are shown in Fig. 4.2.



**Figure 4.2:** Scanning electron micrographs (SEM) of the prepared electrodes. (a) Bare  $\text{NaTaO}_3$ , (b) 0.57 wt.% La, (c) 0.83 wt.% La, and (d) 1.11 wt.% La.

The images were taken with a 25.000x resolution. The paste preparation does not have an effect on the particle size or shape. Bare  $\text{NaTaO}_3$  presents an inhomogeneous distribution of particle shape and sizes, but still the different particles can be differentiated in the image. However, with increasing lanthanum doping, the particles start to accumulate and form aggregates, losing their original shape and size, with the material doped with 1.11 wt.% La being the one that presents the most distorted surface.

## 4.2 Specific surface area

The determination of the specific surface area (BET) of bare and lanthanum doped  $\text{NaTaO}_3$  powders was done by means of nitrogen absorption measurements. Table 4.1 summarizes the data obtained from the measurements of all investigated materials. It is obvious that the lanthanum doping induces an increase in the specific surface area from 2.7 to 5.4  $\text{m}^2/\text{g}$  as expected from the SEM images.

**Table 4.1:** Specific surface area (BET) of bare and La-doped NaTaO<sub>3</sub> powders.

Material	Specific surface area (BET) (m <sup>2</sup> /g)
NaTaO <sub>3</sub>	2.7
NaTaO <sub>3</sub> 0.57 wt.% La	4.0
NaTaO <sub>3</sub> 0.83 wt.% La	5.2
NaTaO <sub>3</sub> 1.11 wt.% La	5.4

### 4.3 Raman spectroscopy

#### 4.3.1 Powders

Raman spectroscopic analysis was performed for bare and lanthanum doped powders in order to obtain additional structural information. The respective spectra are shown in Fig. 4.3. It has been reported by R. Krishnan<sup>113</sup> and P. S. Dobal<sup>114</sup> that the mid-energy Raman bands from 100 to 450 cm<sup>-1</sup> generally correspond to O-Ta-O bending vibrations in the TaO<sub>6</sub> octahedra. Pure skeletal modes involving Ta-O-Ta bending coordinates in different types of polyhedra might contribute to several of these bending modes. The higher energy bands from 450 to 900 cm<sup>-1</sup> could be associated with the coupled modes involving mainly the stretching of the various Ta-O bonds present in the structure with different magnitudes of bond order. Because both, the corner and the edge-shared octahedra are present in the structure, multiple bands due to the stretching vibrations of specific Ta-O bonds are possible. However, the differentiation between various types of edge-shared polyhedra is difficult.

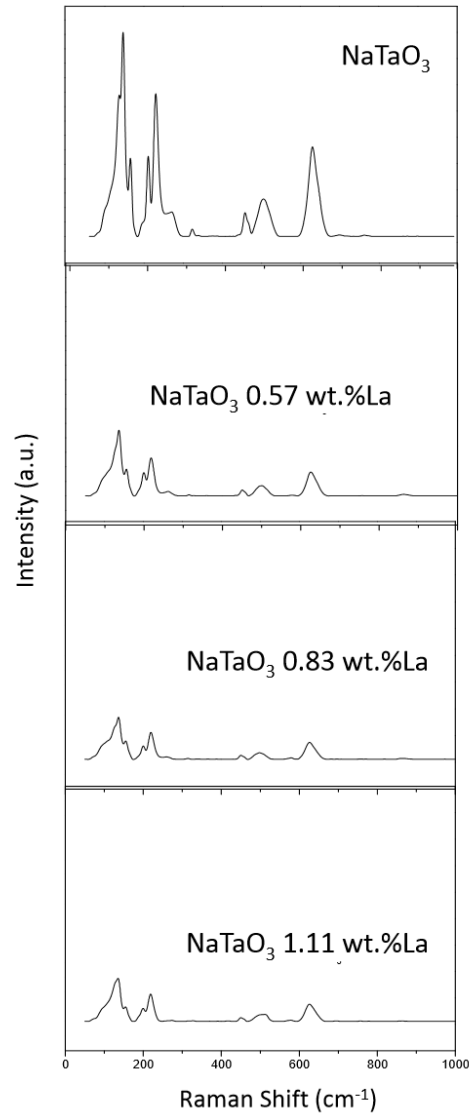


**Figure 4.3:** Raman spectra of bare and lanthanum doped  $\text{NaTaO}_3$  powders.

As can be clearly seen from the Raman spectra, with increasing lanthanum doping the bands mentioned before suffer a drastic decrease in intensity and shape. The decrease of intensity and the loss of shape of the signals can be attributed to particle accumulation forming aggregates. This correlates well with the scanning electron micrographs presented in the subsection before.

### 4.3.2 Electrodes

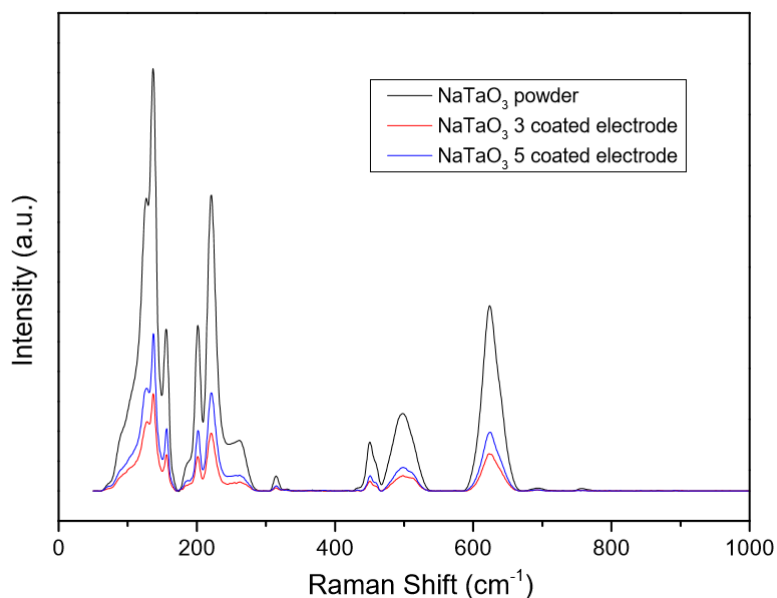


**Figure 4.4:** Raman spectra comparing the prepared electrodes using bare NaTaO<sub>3</sub> with three and five coating layers and the unmodified powders.

For obtaining structural information of the particles after the paste preparation process, Raman spectroscopy was used as well. In this case, the films prepared using bare NaTaO<sub>3</sub> were compared with the unmodified powders. Fig. 4.4 compares bare and unmodified NaTaO<sub>3</sub> powders and the prepared electrodes with three and five coating layers. The electrode calcination does not change the structural properties of the material, as no new signals were observed for the films. However, an intensity difference in the Raman signals was observed when different amount of paste was deposited on the glass.

## 4.4 Diffuse reflectance

### 4.4.1 Powders

The optical properties of bare and lanthanum doped NaTaO<sub>3</sub> were determined using UV-Vis diffuse reflectance spectroscopy. The band gap of the materials was evaluated with and without lanthanum in the system. Fig. 4.5 shows the diffuse reflectance spectra obtained

for bare and La-doped NaTaO<sub>3</sub> with different amounts of lanthanum, *i.e.*, 0.57, 0.83 and 1.11 wt.% of La.

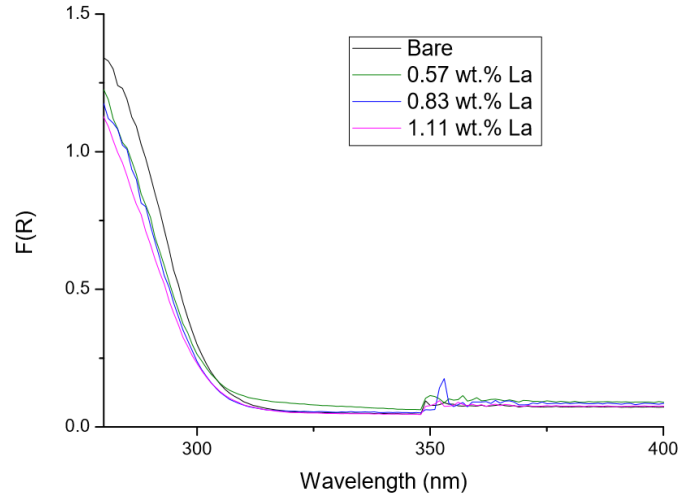


**Figure 4.5:** Diffuse reflectance spectra for bare and La-doped NaTaO<sub>3</sub>.

Fig. 4.5 shows a plot of the Kubelka-Munk function  $F(R)$  *vs.* the wavelength. The material starts absorbing light below 310 nm. The small distortion at 350 nm may be caused because of the change in the lamp.  $F(R)$  which is defined in eq. 4.1, is the measured reflectance with respect to a standard which in this case is BaSO<sub>4</sub> powder. This  $F(R)$  according to the Kubelka-Munk theory depends of the wavelength.

$$f(R) = \frac{(1 - R)^2}{2R} \quad 4.1$$

As the Kubelka-Munk function  $F(R)$  is equivalent to the absorption it is clear from the figure that the lanthanum doping does not have any impact in the optical properties of the material. The optical band gap was determined by plotting the modified Kubelka Munk Function *vs.* the energy ( $E$ ) of the exciting light (see discussion chapter). The intercept at 310 nm which corresponds to a band gap of approx. 4.0 eV according to eq. 3.1 for all materials. This result is in good agreement with the value found in the literature<sup>105</sup>.

#### 4.4.2 Electrodes

Diffuse reflectance spectroscopy measurements were carried out for the prepared electrodes in order to compare the optical properties of the latter with the optical properties of the powders. Fig. 4.6 presents the light absorption in terms of the Kubelka-Munk function  $F(R)$  of undoped NaTaO<sub>3</sub> powders and electrodes coated with three layers of paste prepared with bare material.



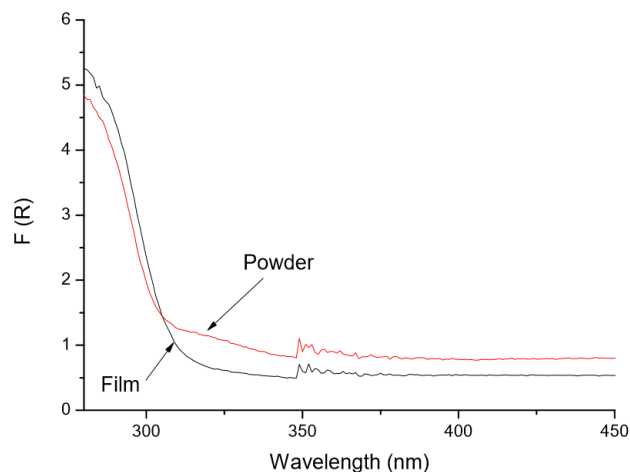


**Figure 4.6:** Diffuse reflectance spectra of bare  $\text{NaTaO}_3$  powder and film.

No significant difference can be observed between powder and films. It is important to note that as the Raman spectroscopy measurements already showed, no changes in the optical absorption were expected for the films. The SEM measurements showed that the morphology of the particles remained the same and therefore, the light absorption should also take place at the same wavelengths.

#### 4.4.3 Absorption coefficient

In the work of Ivanova<sup>18</sup> the absorption coefficient of bare and La-doped  $\text{NaTaO}_3$  was examined in the range of 250 to 600 nm. For this purpose, the absorption of several photocatalyst suspensions prepared at different concentrations was measured. The obtained values are shown in Fig. 4.7.

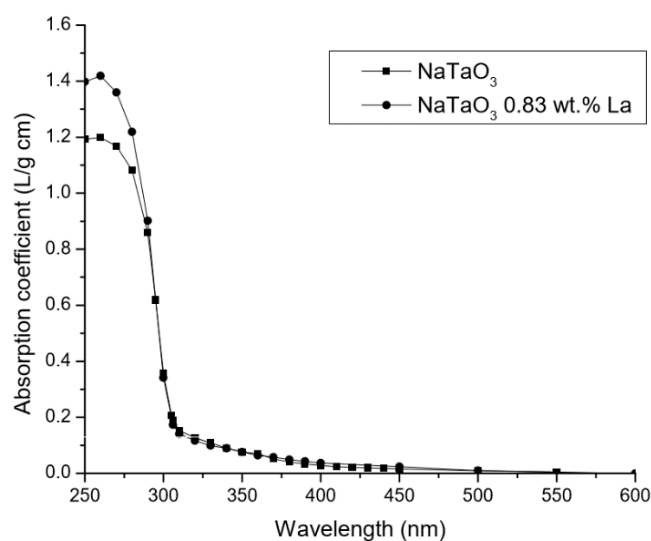


**Figure 4.7:** Absorption coefficient of bare and 0.83 wt.% La  $\text{NaTaO}_3$  aqueous suspensions<sup>18</sup>.

The comparison of the two spectra shown in Fig. 4.7 evidences that there is no big difference between the absorption of bare and lanthanum doped sodium tantalate. Both of the materials exhibit only a small light absorption from 400 to 300 nm. Smaller wavelengths than 300 nm present a much higher light absorption coefficient. The material with 0.83 wt.% of La has a slightly higher absorption than the bare material around 250 nm.

#### 4.5 Flatband potential measurements

The flatband potential ( $E_{FB}$ ) of the semiconductor materials at the semiconductor/electrolyte junction have been evaluated by means of Mott-Schottky plots, which are measured in the dark. For this purpose, the capacitance of the semiconductor thin films has been measured when a potential sweep from -1 to +1 V was applied and a frequency of 100 Hz or 1 KHz respectively was used. Fig. 4.8 presents the inverse of the square of the measured capacitance *vs.* the applied potential at different frequencies.

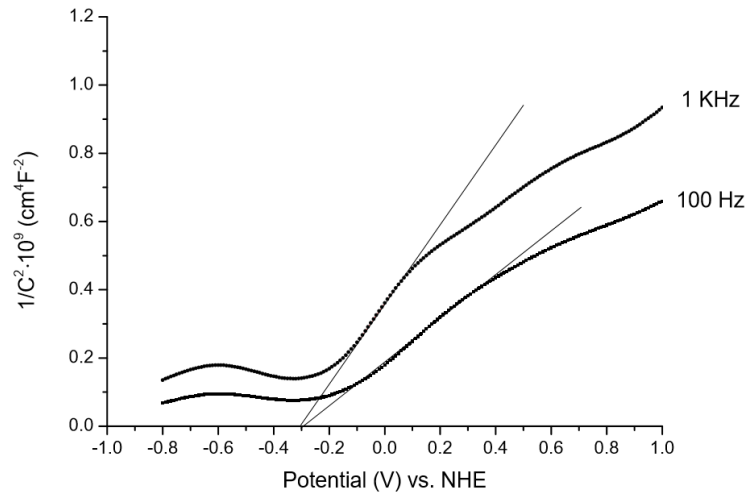


**Figure 4.8:** Mott-Schottky plots of bare  $\text{NaTaO}_3$  films on FTO measured at different frequencies using KCl (0.1 M).

Plotting  $1/C^2$  versus the potential should yield a straight line intersecting the potential at the  $E_{FB}$ . Depending on the examined potential range, different flatband potentials are obtained from the two different straight lines that can be drawn through these data points. The reason of choosing the steepest line possible to extract the flatband potential can be found in <sup>115,116</sup>. By drawing a line through the steep slope, the same flatband potential can be obtained for flat surface electrodes as for harshened electrodes. Therefore, the slope and the intercept of the steep line fit have been used to evaluate the flatband potential. Fig. 4.8 shows two Mott-Schottky plots for bare  $\text{NaTaO}_3$  at frequencies of 100 Hz and 1 KHz. The results presented in this figure clearly demonstrate that the frequency has an influence on the slope of the calculated straight line, but the intercept with the X-axis occurs at the same point indicating that the flatband potential for  $\text{NaTaO}_3$  lies at around -0.32 V *vs.*

NHE. As shown in Fig. 4.5, the band gap of the material does not change with lanthanum doping, remaining constant at 4.0 eV.

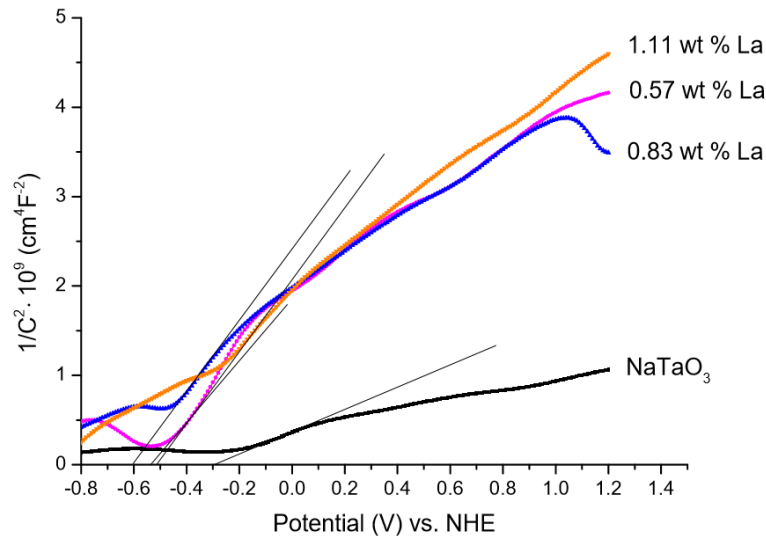


**Figure 4.9:** Mott-Schottky plots for bare and La-doped  $\text{NaTaO}_3$  measured at 1 KHz.

Mott-Schottky plots were evaluated for the La-doped materials in order to investigate a possible shift in the conduction and valence band positions. The respective results are presented in Fig 4.9., and it clearly shows that lanthanum doping has an effect on the slope of the Mott-Schottky plots. All three La-doping amounts present a steeper slope than the bare material. The respective donor density  $N_D$  can be calculated from the slope of these lines<sup>115</sup>. Depending on the examined material, different flatband potentials can be drawn through these data points, which translates into a negative shift of the flatband potential for the La-doped materials. The negative shift is, however, not directly proportional to the lanthanum amount. The material with 0.83 wt.% La exhibits the most negative flatband potential. It has to be noted that the differences in the flatband potentials between the lanthanum doped materials are not as large as the difference between the lanthanum doped and the bare material. The flatband potentials and calculated donor densities are compiled in Table 4.2. To ensure a straightforward comparison of the results for the  $\text{NaTaO}_3$  prepared for this work,  $E_{FB}$  and  $N_D$  values were calculated from the capacity measurements performed at 1 KHz using equation 2.4. The value of the dielectric constant for  $\text{NaTaO}_3$  has not been reported to date, but taken into account the values for other metal oxides such as  $\text{TiO}_2$  a hypothetical value of  $\epsilon(\text{NaTaO}_3)$  of 30 was used<sup>115</sup>.

**Table 4.2:** Flatband potentials and donor densities for bare and La-doped NaTaO<sub>3</sub>.

Material	V <sub>FB</sub> <i>vs.</i> NHE (V)	Donor Density (cm <sup>-3</sup> )
NaTaO <sub>3</sub>	-0.32 ± 0.02	9.27 · 10 <sup>28</sup>
NaTaO <sub>3</sub> 0.57 wt.% La	-0.54 ± 0.02	5.77 · 10 <sup>28</sup>
NaTaO <sub>3</sub> 0.83 wt.% La	-0.61 ± 0.01	6.84 · 10 <sup>28</sup>
NaTaO <sub>3</sub> 1.11 wt.% La	-0.51 ± 0.01	8.32 · 10 <sup>28</sup>

When 0.57 wt.% La is present in the system, a shift of 0.22 V in the flatband potential occurs (from -0.32 V to -0.54 V *vs.* NHE). When the lanthanum content increases to 0.83 wt.% La, the flatband potential shifts to -0.61 V *vs.* NHE which is the most negative value found for all La-doped materials studied here. After this, a further increase in the lanthanum amount does not translate into a more negative flatband potential. The high donor density values obtained can be understood as a result of very thin and highly defective oxide films<sup>115</sup>. In equation 2.2 it is presented the relation between donor density and the width of the space charge layer. With increasing donor densities, the space charge layer becomes narrower.

#### 4.6 Quantum yield determination

The quantum yield is defined as:

$$\phi(\%) = \frac{r}{I_0 \cdot A} \times 100 = \frac{5 \cdot 10^{-6} \text{ mol} \cdot \text{s} \cdot \text{cm}^2}{3600 \text{ s} \cdot 2.03 \cdot 10^{-8} \text{ mol} \cdot 7.065 \text{ cm}^2} \times 100 = 0.97 \%$$

where  $r$  is the rate of gas evolution,  $I_0$  is the number of absorbed photons and  $A$  is the irradiated area.  $I_0$  has been calculated as follows:

$$\begin{aligned} I_0 &= \frac{I_a \cdot \lambda}{N_A \cdot h \cdot c} = \frac{8.2 \cdot 10^{-3} \text{ J} \cdot \text{s}^{-1} \cdot \text{cm}^{-2} \cdot 306 \cdot 10^{-9} \text{ m}}{6.022 \cdot 10^{23} \text{ mol}^{-1} \cdot 6.626 \cdot 10^{-34} \text{ J} \cdot \text{s} \cdot 2.998 \cdot 10^8 \text{ m} \cdot \text{s}^{-1}} \\ &= 2.03 \cdot 10^{-8} \text{ mol} \cdot \text{s}^{-1} \cdot \text{cm}^{-2} \end{aligned}$$

with  $I_a$ : the total energy which can be absorbed by the NaTaO<sub>3</sub> particles.

$\lambda$ : the wavelength corresponding to the band gap energy of NaTaO<sub>3</sub>

$N_A$ : Avogadro constant

$h$ : Planck constant

$c$ : speed of light

$I_a$  has been determined according to the following equation:

$$I_a = I_\lambda \cdot F_s = 0.41 \text{ mW} \cdot \text{cm}^{-2} \cdot 0.02 = 0.0082 \text{ mW} \cdot \text{cm}^{-2} = 8.2 \cdot 10^{-3} \text{ J} \cdot \text{s}^{-1}$$

where  $I_\lambda$  is the light intensity of the employed lamp being determined by the integration of the irradiance of the lamp at 350 nm (see Fig. 3.3 right axis).  $F_s$  is the integrated absorption fraction of the NaTaO<sub>3</sub> particles at 350 nm which has been determined using the following equation:

$$F_s = \frac{\int_{\lambda_1}^{\lambda_2} I_\lambda f_\lambda^s d\lambda}{\int_{\lambda_1}^{\lambda_2} I_\lambda d\lambda} = \frac{0.0082}{0.41} = 0.02 \quad \text{with } f_\lambda^s = 1 - 10^{-A_\lambda^s}$$

where  $A_\lambda^s$  is the absorbance of the suspended NaTaO<sub>3</sub> particles at 350 nm measured by means of an UV-vis spectrophotometer (see Fig. 3.3 left)



## 5. Results

### 5.1 Photocatalytic H<sub>2</sub> evolution upon sub-band gap irradiation

The analysis of the photocatalytically evolved molecular hydrogen from a 0.03 M aqueous methanol suspension of platinized sodium tantalate is shown in Fig. 5.1.

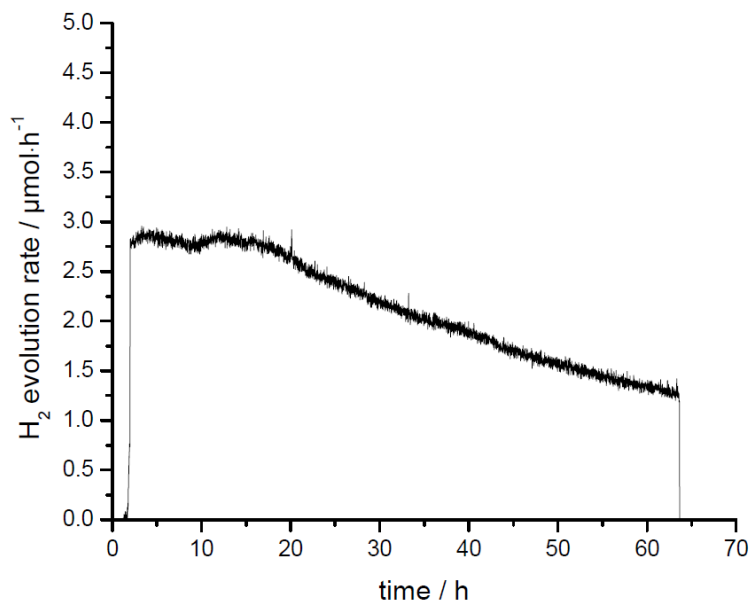


**Figure 5.1:** Photocatalytic evolution of H<sub>2</sub> from aqueous methanol solution employing undoped NaTaO<sub>3</sub>. Methanol concentration: 0.03 M, Pt loading: 1 wt.%, reactor volume: 50 ml, Irradiation intensity:  $I_{350} = 41 \text{ mW}/\text{cm}^2$ .

The figure above presents the evolution of H<sub>2</sub> when bare NaTaO<sub>3</sub> was irradiated with a light of 350 nm. The material exhibits a small light absorption starting from 375 to 300 nm as observed in Fig. 4.5. In order to evaluate if some molecular hydrogen could be produced upon illumination with this wavelength, this photocatalytic measurement was performed. As co-catalyst, 1 wt.% of Pt was added, as well as an aqueous methanol solution of 0.03 M.

Small amounts of molecular hydrogen can be detected when the sample was irradiated at 350 nm. The irradiation with this wavelength corresponds to an energy lower than the band gap energy. The work of Ivanova<sup>18</sup> shows a deeper study of the photocatalytic water splitting using NaTaO<sub>3</sub> suspensions. In this work, the whole range of wavelengths of the xenon lamp was used to irradiate the sample, whilst herein only light of 350 nm was used. Because of the lower light absorption of undoped NaTaO<sub>3</sub> at 350 nm, the amount of evolved H<sub>2</sub> is much lower than when light from a range between 250 to 450 nm was used. Fig. 5.1 shows a H<sub>2</sub> evolution of 2.8  $\mu\text{mol}/\text{h}$  at 350 nm (quantum yield of 0.97%). However, the

work of Ivanova reports a  $\text{H}_2$  evolution of  $47 \mu\text{mol/h}$  (quantum yield of 14 %) when the sample was irradiated with a range of wavelengths from 250 to 450 nm<sup>18</sup>.

## 5.2 Determination of free radicals by EPR

The measurements performed using the electron paramagnetic resonance (EPR) technique are presented in this chapter. Fig. 5.2 shows the EPR measurements performed in vacuum for undoped  $\text{NaTaO}_3$ .

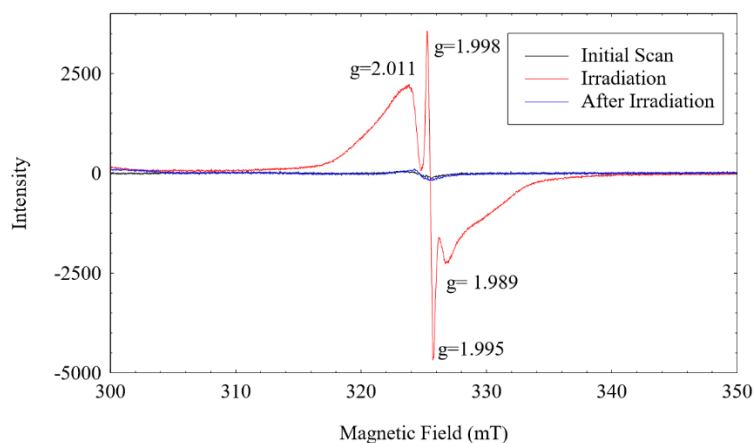


**Figure 5.2:** EPR spectra of undoped  $\text{NaTaO}_3$  in vacuum.

The initial EPR spectrum of bare  $\text{NaTaO}_3$  in the dark (initial scan), prior to irradiation does not show a lot of information as it only exhibits a small curve centered at 325 mT. The sample was subsequently illuminated with broadband irradiation (320-900nm), which was achieved by using pyrex and water filters to cut off the IR and UV wavelengths. However, this had no observable effect on the measurements due to the large band gap of  $\text{NaTaO}_3$  (4.0 eV). A wavelength of approximately 315 nm or below is required for photoexcitation of the sample and therefore it is expected that the material can only be excited by UV irradiation (200-320 nm).

Without the pyrex filter, which allow passage of some UV light into the sample, an intense EPR signal with primarily symmetrical components appears. The signal persists for the duration of the irradiation but disappears instantly when the light is turned off. This signal reappears with further irradiation, and it can be reversibly bleached in the dark and consecutively made to reappear by turning the light on and off. As no signal was observed in the dark, no long lived deeply trapped holes or electrons could be identified, unlike in many other semiconductors such as in titanium dioxide, where electrons have been reported to persist on trap states after irradiation at 80 K<sup>117</sup>.



**Table 5.1:** Different isotopes and their contributions to the observed EPR signals of NaTaO<sub>3</sub> including contributions from nuclear spins.

Isotope	Natural Abundance (%)	Nuclear Spin (I)	Number of peaks (2N+1)	
			N=1	N=2
<sup>23</sup> Na	100	3/2	4	7
<sup>180</sup> Ta	0.012	8	17	33
<sup>181</sup> Ta	99.988	7/2	8	15
<sup>16</sup> O	99.757	0	1	1
<sup>17</sup> O	0.038	5/2	6	11
<sup>18</sup> O	0.205	0	1	1

Fig. 5.3 presents the results of NaTaO<sub>3</sub> in presence of molecular oxygen and shows four peaks, two with a positive intensity and two with a negative intensity in the EPR spectrum during irradiation. However, two of the observed peaks are broad humps at  $g = 2.011$  and  $g = 1.992$ , which will have a finer hyperfine splitting that cannot be identified with the current resolution. As the sample was examined in its powdered form, the orientation dependence of the signal must be considered. Hyperfine splitting, which arises from an electron interacting with the magnetic contribution of its corresponding nuclei, arises from hyperfine anisotropy, *i.e.* the directional dependence of the electron with regard to the nucleus. This effect is not field dependent, which means that all hyperfine splitting components are observed at an equal distance from each other. The distance between peaks caused by hyperfine splitting is always the same, and does not increase or decrease with increasing magnetic field. Thus, it is certain that the EPR signal observed during irradiation has at least two separate contributions; the signal observed as a sharp peak at  $g = 2.001$  and  $g = 1.998$ , and the signal observed as two broad bumps at  $g = 2.011$  and  $g = 1.992$ .

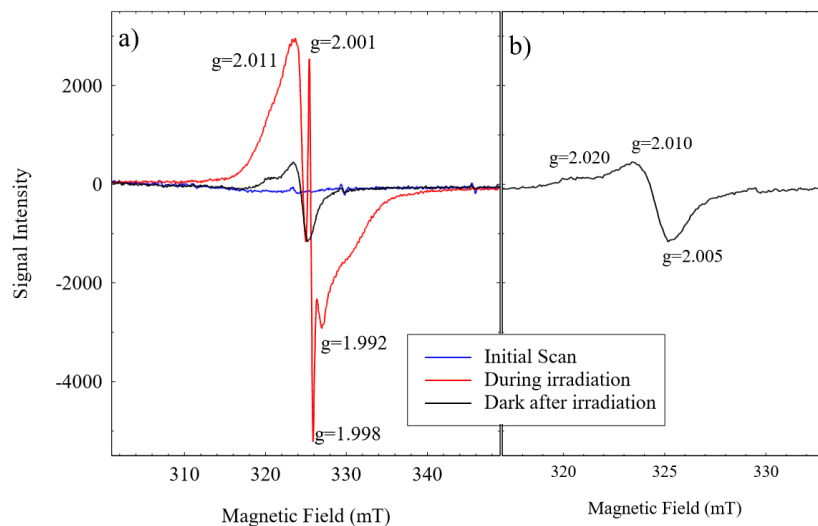


**Figure 5.3:** EPR spectra of bare NaTaO<sub>3</sub> in molecular oxygen (20 mbar) a) 300-350 mT scan before, during and after irradiation, and b) close up on the observed superoxide species after irradiation at 315-335 mT.

Upon addition of molecular oxygen, the EPR signal the undoped NaTaO<sub>3</sub> changes in two ways. First, the ratio of the intensity of the trapped electron signal decreases significantly compared to that of the hole signal, when comparing to the measurements taken in vacuum. Second, when the light was turned off, the spectrum was not perfectly bleached, but a signal remained. This signal can be reversibly changed between the one appearing during irradiation and after irradiation by turning the light on and off, and no change in the intensity of the signal was observed with consecutive repeats. Upon further evacuation at room temperature the signal returned to its original state. The small sharp peaks appearing all over the spectrum arise from physisorbed oxygen on the surface of the sample.

The effect of methanol on bare NaTaO<sub>3</sub> has been studied with EPR as well and the results are shown in Fig. 5.4. An evacuated sample of undoped sodium tantalate was subjected to saturated vapor pressure of methanol overnight prior to the measurements. The observed initial scan prior to the experiment was the same as for bare NaTaO<sub>3</sub> in vacuum, with the difference that the signal remained after turning off the light. The signal can be reversibly changed between that observed during and after irradiation by turning the light on and off.

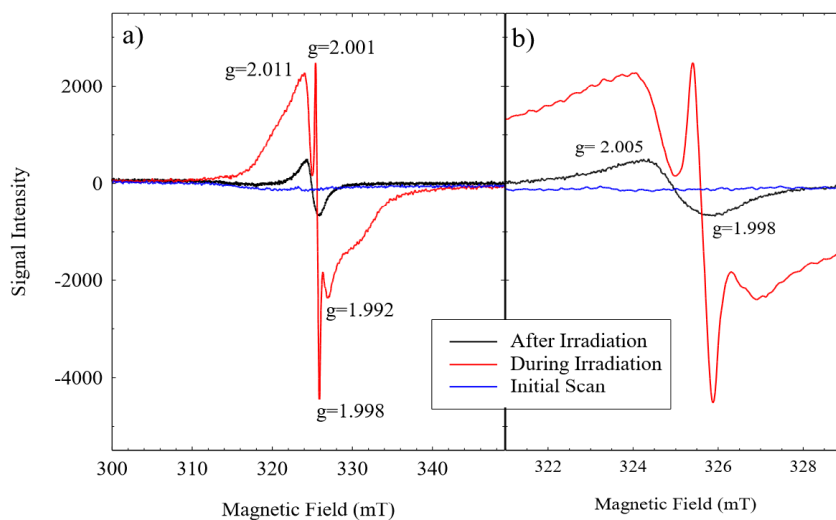


**Figure 5.4:** EPR spectra of bare  $\text{NaTaO}_3$  in saturated vapor pressure of methanol in a) the wide scan measurements are for the four component signal appearing during irradiation, and the g-value b) the narrow scan spectra are for the two component signal appearing in the dark after irradiation.

EPR measurements were carried out for  $\text{NaTaO}_3$  0.83 wt.% La as well (see Fig. 5.5), and they showed very similar behavior as bare  $\text{NaTaO}_3$ . The appearance of a small signal, which was observed asymmetrically at  $g = 2.011$ , was noted, and it was already there prior to irradiation, and it appeared both in the presence as well as in the absence of molecular oxygen.

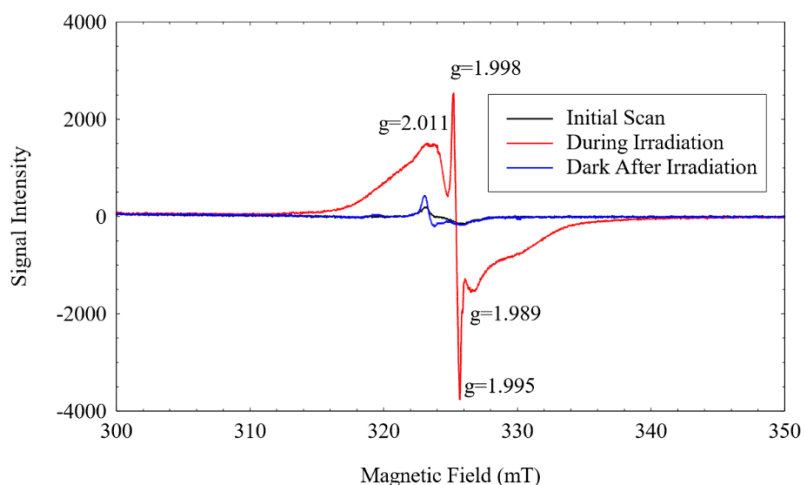


**Figure 5.5:** EPR spectra of  $\text{NaTaO}_3$  0.83 wt.% La.

### 5.3 Laser flash photolysis

The laser flash photolysis results for bare NaTaO<sub>3</sub> as well as lanthanum doped NaTaO<sub>3</sub> with 0.57, 0.83 and 1.11 wt.% of La are presented in this section. The results compile measurements performed without sacrificial reagents and when electron and/or hole scavengers were added to the system. All measurements were carried out using two different excitation wavelengths (248 and 351 nm).

#### 5.3.1 Band gap excitation with UV(C) light

The different samples were illuminated with 248 nm. Irradiating the sample with this wavelength ensures that the material will absorb light very easily and a good amount of electrons and holes can be generated (see Fig. 4.5). As shown in section 4.4.1, the band gap of NaTaO<sub>3</sub> is 4.0 eV. Irradiation with 248 nm corresponds to an energy of 5.0 eV which is over the band gap of the material.

$$E = \frac{h \cdot c}{\lambda} = \frac{4.136 \times 10^{15} \text{ eV} \cdot \text{s} \cdot 3 \times 10^8 \text{ m} \cdot \text{s}^{-1}}{248 \times 10^{-9} \text{ m}} = 5.0 \text{ eV} \quad 5.1$$

with  $h$ : Planck's constant

$c$ : speed of light

$\lambda$ : irradiation wavelength

The section starts with an investigation of the bare material without the presence of any sacrificial reagents. Electrons and hole scavengers were introduced in the subsequent measurements. All measurements were performed three times with freshly prepared samples.

##### 5.3.1.1 Excitation in the absence of sacrificial reagent

Fig. 5.6 shows the transient absorption signal of undoped NaTaO<sub>3</sub> without any sacrificial reagent. The measurements were performed in argon and in vacuum, purging the sample prior to the measurement, in order to remove adsorbed hydroxyl groups at the surface of the material.

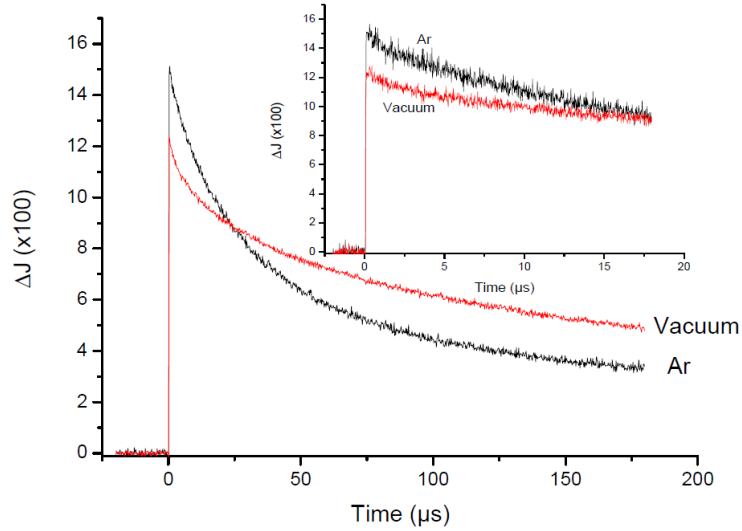


**Figure 5.6:** Transient absorption signals for bare  $\text{NaTaO}_3$  in Ar and vacuum measured at 310 nm. Inset: measurement during 20  $\mu\text{s}$ .

Fig. 5.6 shows that there is a difference between the signal decay measured in argon and in vacuum, being the signal decay in argon faster than in vacuum. The half lifetime of the photogenerated charge carriers ( $t_{1/2}$ ) has been calculated in order to compare the decay of the signals as is represented in Fig. 5.7.

The highest absorption intensity measured is labeled as  $A_1$  and the correspondent time is labeled as  $t_1$ . For calculating  $t_{1/2}$  the time at which the absorption intensity is reduced in half has to be found. Therefore,  $A_2$  corresponds to the absorption intensity at which half of the photogenerated charge carriers have already reacted. The corresponding time at which this happens is labeled as  $t_2$ . Using  $t_{1/2} = t_2 - t_1$  the half-life of the photogenerated charge carriers is obtained. The representation of how  $t_{2/3}$  is obtained can be seen in Fig. 5.7 as well. This will be employed for the results of the measurements using a 351 nm laser wavelength.

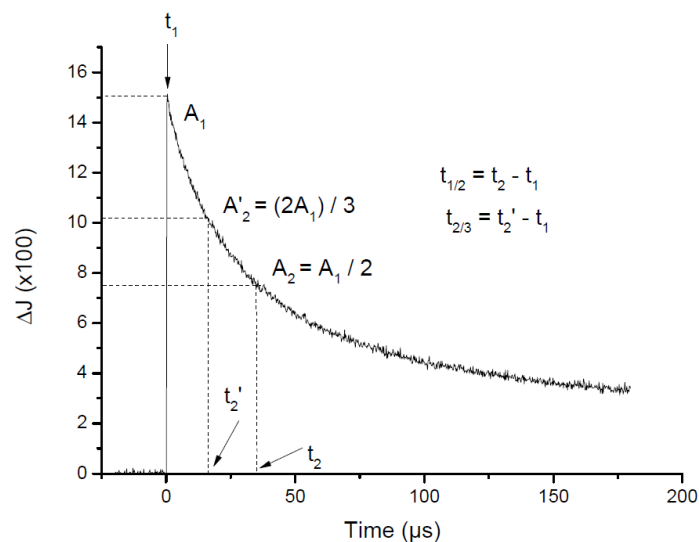


**Figure 5.7:** Graphic representation of the calculation of the half-life ( $t_{1/2}$ ) and  $t_{2/3}$  of the photogenerated charge carriers.

As Fig. 5.6 shows, the decay in argon is faster than in vacuum. The signal was measured during 200  $\mu\text{s}$  and in that period of time 74 % of the signal has disappeared when measured in argon. On the contrary, only 60 % of the signal has disappeared in vacuum after 200  $\mu\text{s}$ . A faster decay of the signal translates in a shorter half-life of the photogenerated charge carriers. Using the method explained in Fig. 5.7,  $t_{1/2}$  was determined for both signals and  $t_{1/2} = 34.2 \pm 0.3 \mu\text{s}$  was found for argon and  $t_{1/2} = 98.0 \pm 0.2 \mu\text{s}$  for vacuum. This difference can be due to the fact that after 1h of purging with argon there can still be some traces of adsorbed oxygen at the surface of the particles, whilst the vacuum system is more effective in the removal of the adsorbed oxygen atoms from the surface.

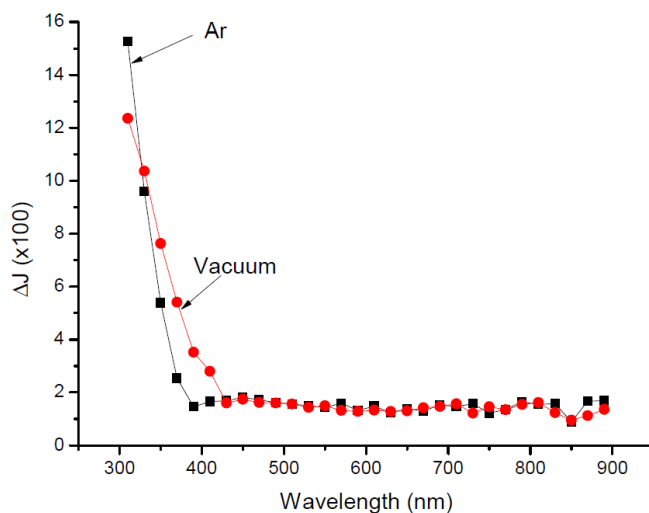


**Figure 5.8:** Transient absorption spectra 20  $\mu\text{s}$  after laser irradiation for bare  $\text{NaTaO}_3$  in Ar and vacuum.

The transient absorption spectra for both experiments were measured in a wavelength range from 300 to 890 nm. As Fig. 5.8 shows, both spectra exhibit a very intense absorption signal at 310 nm. Besides this high signal, no other signals or shoulders can be seen in the measured range. It has to be noted that for the signal measured in argon, the absorption intensity is higher than for the signal in vacuum. That means that a higher concentration of photogenerated charge carriers are created when argon is purged than when vacuum conditions were used.

### 5.3.1.2 Excitation in the presence of electron scavengers

In this section, the results of measurements with electron acceptors are presented. The experiments were performed in air, O<sub>2</sub> and after photodeposition of Pt nanoparticles.

#### 5.3.1.2.1 Bare NaTaO<sub>3</sub> in air

Fig. 5.9 shows the transient absorption signals measured in different wavelengths for undoped NaTaO<sub>3</sub> in air

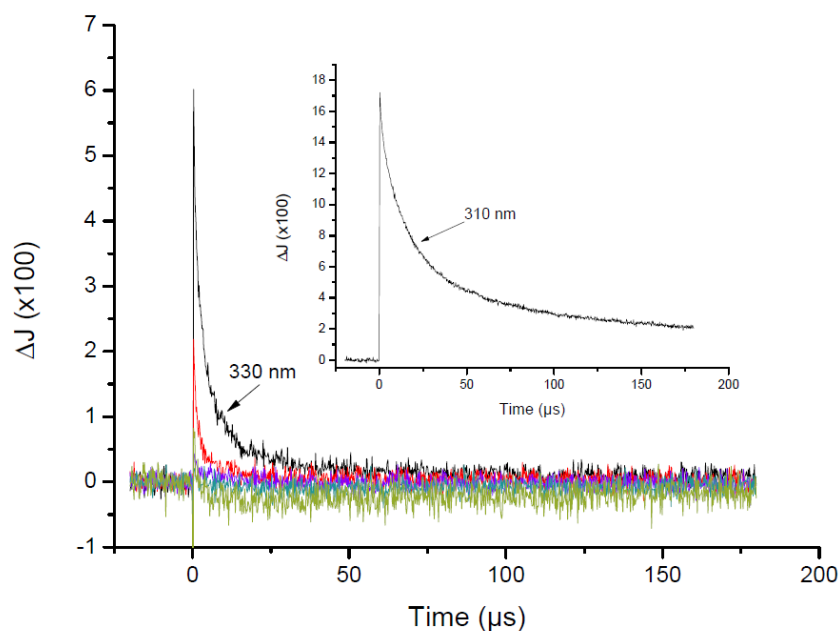


**Figure 5.9:** Transient absorption signals for bare NaTaO<sub>3</sub> in air and analyzed at 330, 350, 450, 550 and 850 nm. Inset: transient absorption kinetic signal measured at 310 nm.

As Fig. 5.9 shows, the signal at 310 nm presents the highest absorption intensity and the slowest decay of the whole measured range. When the analyzing wavelength was increased, the transient absorption signals observed exhibit lower absorption intensities and a much faster decay than the signal at 310 nm. However, it has to be noted that this peak cannot be described as a maximum. Because of the photomultiplier detector and xenon lamp limitations of the system, measurements at lower wavelengths could not be performed and the signal at 310 nm may not be the highest point of the curve.

The inset of Fig. 5.9 illustrates the transient absorption signal at 310 nm isolated from the other analyzing wavelengths in order to evaluate it in more detail. The signal presents a very sharp absorption with a fast decay (after 100  $\mu\text{s}$  42 % of the photogenerated charge carriers have already recombined). The calculated  $t_{1/2}$  is  $17.2 \pm 0.1 \mu\text{s}$ .

After the observed signals have been evaluated, the transient absorption spectra for bare  $\text{NaTaO}_3$  in air are plotted in Fig 5.10. Three different times have been chosen ( $t_1=1 \mu\text{s}$ ,  $t_2=60 \mu\text{s}$  and  $t_3=165 \mu\text{s}$ ), in order to identify the different photogenerated charge carriers that might be appearing.

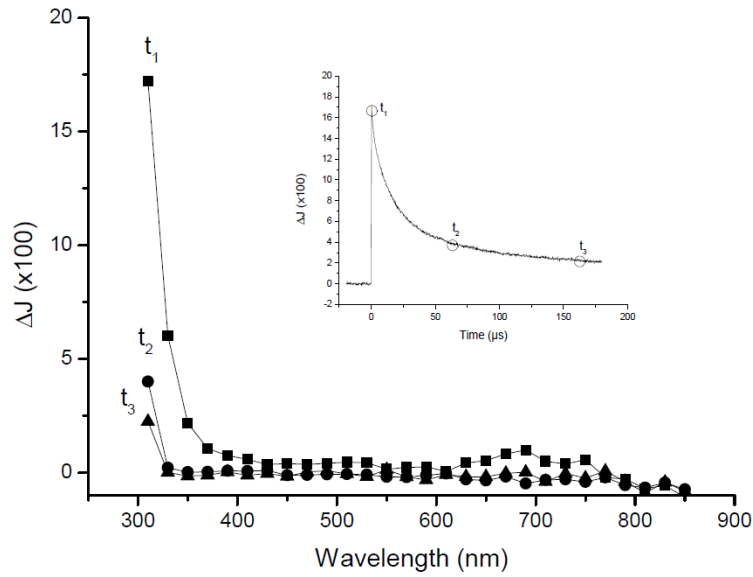


**Figure 5.10:** Transient absorption spectra at ( $t_1=1 \mu\text{s}$ ), ( $t_2=60 \mu\text{s}$ ) and ( $t_3=165 \mu\text{s}$ ) for bare  $\text{NaTaO}_3$  in air. Inset: transient absorption kinetic signal for bare  $\text{NaTaO}_3$  in air at 310 nm.

Fig. 5.10 shows the transient absorption spectra for bare  $\text{NaTaO}_3$  in air measured at three different times after the laser pulse ( $t_1=1\mu\text{s}$ ), ( $t_2=60\mu\text{s}$ ) and ( $t_3=165 \mu\text{s}$ ). No other signals appear in the spectra after analyzing the signal at the beginning, middle and end of the signal besides the peak at 310 nm. The fact that no new signals emerge when looking at different times can be explained because no new species or intermediates are being formed, and that the photogenerated charge carriers responsible for the peak at 310 nm decrease their concentration with time. The transient absorption spectrum of bare  $\text{NaTaO}_3$  has been measured and compared with the spectrum measured in argon as shown in Fig. 5.11.



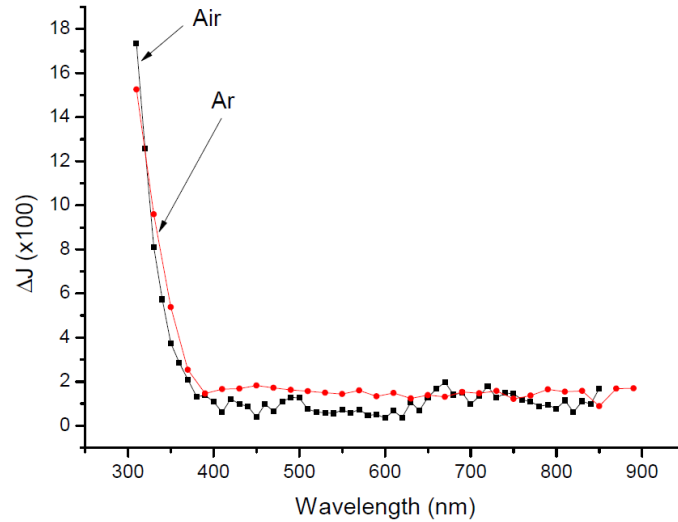


**Figure 5.11:** Transient absorption spectra 20  $\mu\text{s}$  after the laser pulse for bare  $\text{NaTaO}_3$  in air and Ar.

Both spectra shown in Fig. 5.11 are follow the same pattern and are very similar. The highest measured signal appears at 310 nm in both cases and presents a fast decay. However, the spectrum measured in air exhibits a slightly higher absorption intensity than the spectrum measured in argon.

### 5.3.1.2.2 Lanthanum doped tantalates in air

In this section, the effect of different amounts of lanthanum (0.57, 0.83 and 1.11 wt.% La) on the observed transient absorption signals is evaluated. Fig. 5.12 shows the transient absorption signals of undoped and La-doped  $\text{NaTaO}_3$  at 310 nm.

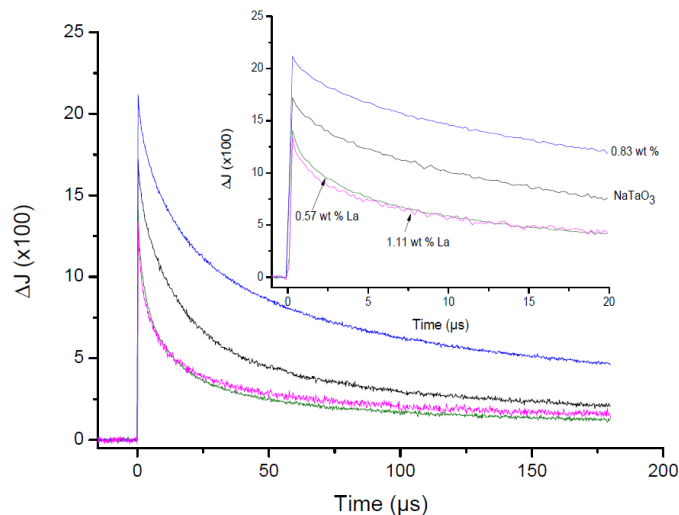


**Figure 5.12:** Transient absorption signals of undoped (black), 0.57 wt.%La (green), 0.83 wt.%La (blue) and 1.11 wt.%La (purple)  $\text{NaTaO}_3$  in air at 310 nm. Inset: measurement during 20  $\mu\text{s}$ .

As Fig. 5.12 shows, the materials doped with 0.57 and 1.11 wt.% of lanthanum exhibit lower initial absorption intensities and a faster decay than the undoped material. The material doped with 0.83 wt.% lanthanum shows the highest absorption intensity of all the studied powders and at the same time the slowest decay. This suggests that an optimum doping concentration has been achieved and charge separation is more effective when the material was doped with 0.83 wt.% of lanthanum.

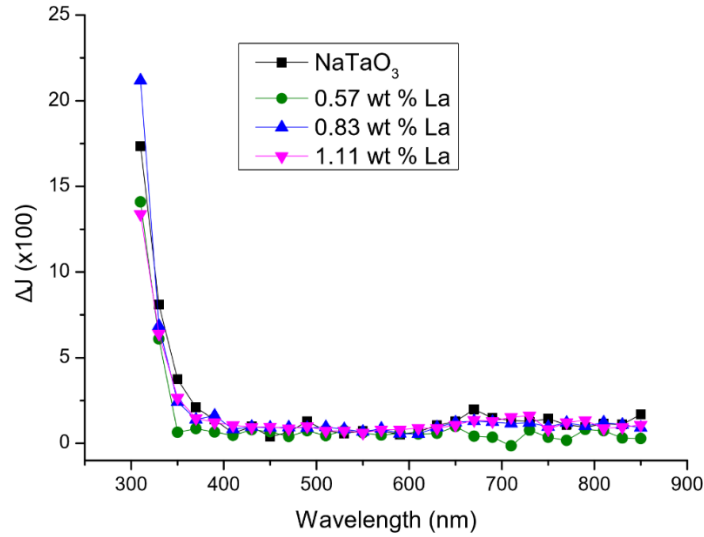


**Figure 5.13:** Transient absorption spectra in air 20  $\mu\text{s}$  after laser irradiation of bare and lanthanum doped  $\text{NaTaO}_3$ .

In Fig. 5.13 are shown the transient absorption spectra of the undoped and La-doped  $\text{NaTaO}_3$  in air at 310 nm. The signal at 310 nm present some differences in its absorption intensity depending on the amount of lanthanum doping. The material with the highest initial absorption was the one doped with 0.83 wt.%La. Lower (0.57 wt.%La) and higher (1.11 wt.%La) lanthanum doping exhibit lower absorption intensities than the undoped  $\text{NaTaO}_3$  and the 0.83 wt.%La. This correlates with the results presented in Fig. 5.12. Table 5.2 resumes the half lifetimes ( $t_{1/2}$ ) and the initial intensities ( $\Delta J_0$ ) of the photogenerated charge carriers for bare and La-doped  $\text{NaTaO}_3$  of Fig. 5.21 and Fig. 5.13.

**Table 5.2:** Summary of the initial intensities ( $\Delta J_0$ ) and the half lifetimes ( $t_{1/2}$ ) of the transient absorption signals in air at 310 nm for undoped and La-doped  $\text{NaTaO}_3$ .

Material	$t_{1/2}$ ( $\mu\text{s}$ )	$\Delta J_0$ (x100)
$\text{NaTaO}_3$	$17.2 \pm 0.1$	17
$\text{NaTaO}_3$ 0.57 wt.% La	$5.8 \pm 0.3$	14
$\text{NaTaO}_3$ 0.83 wt.% La	$27.7 \pm 0.4$	21
$\text{NaTaO}_3$ 1.11 wt.% La	$6.0 \pm 0.3$	13

Table 5.2 clearly demonstrates that for the investigated bare and La-doped NaTaO<sub>3</sub> both the values obtained for the half lifetime and the those measured for the initial intensity of the transient absorption signal at 310 nm show a similar trend:  $\Delta J_0$  and  $t_{1/2}$  of 0.83 wt.%La NaTaO<sub>3</sub> > undoped NaTaO<sub>3</sub> > 1.11 wt.%La NaTaO<sub>3</sub>  $\approx$  0.57 wt.%La NaTaO<sub>3</sub>.

### 5.3.1.2.3 Bare NaTaO<sub>3</sub> in a molecular O<sub>2</sub> purged atmosphere

In this section are presented the measurements done in presence and absence of molecular oxygen.

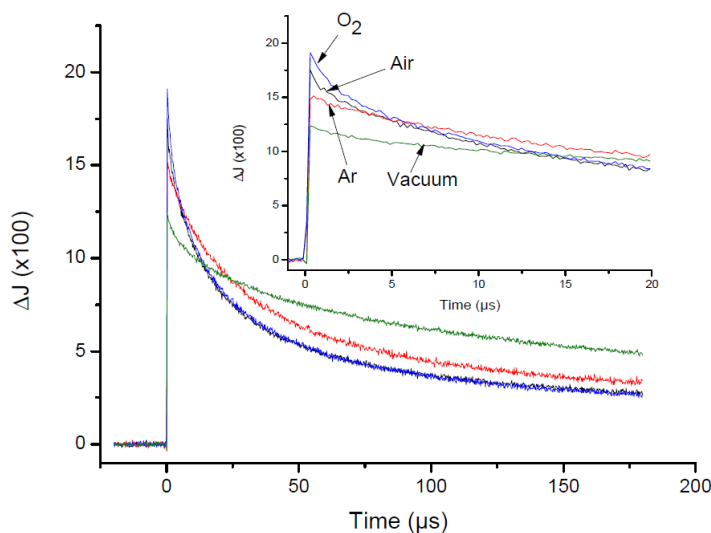


**Figure 5.14:** Transient absorption signals for bare NaTaO<sub>3</sub> in air, Ar, O<sub>2</sub> and vacuum at 310 nm. Inset: measurement during 20  $\mu\text{s}$ .

As Fig. 5.14 shows, different atmospheres have different impacts on the signal decay at 310 nm. The measurements performed in air and after purging with molecular oxygen did not present a significant change in the signal decay, and both curves follow approximately the same trend. The inset of Fig. 5.14 shows, however, a small difference in the absorption intensity for the signals in air and in molecular oxygen. In air the signal presents a slightly lower absorption intensity than in O<sub>2</sub>.

Comparing the results obtained with and without electron scavengers (see Fig. 5.14) it is clear that the presence of electron scavengers in the system has an impact on the decay of the signals. The curves measured in air and in O<sub>2</sub> exhibit faster decays than the curves measured in argon or in vacuum. This leads to shorter half lifetimes of the photogenerated charge carriers as well.

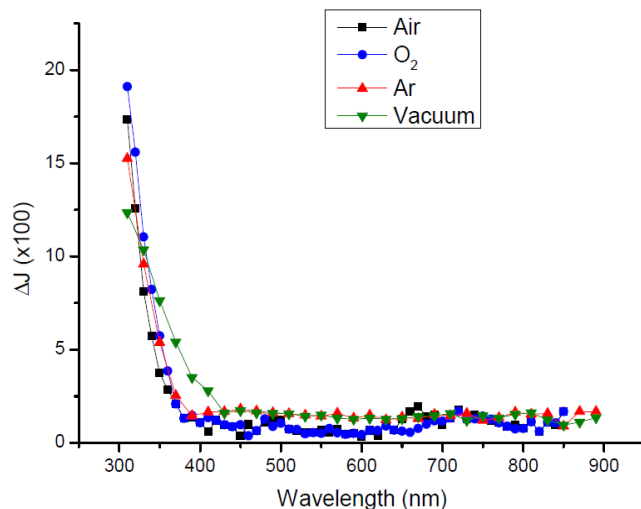


**Figure 5.15:** Transient absorption spectra for bare NaTaO<sub>3</sub> in air, Ar, O<sub>2</sub> and vacuum 20  $\mu$ s after laser excitation.

Fig. 5.15 shows the transient absorption spectra 20  $\mu$ s after the laser pulse for bare NaTaO<sub>3</sub> in air, molecular oxygen, argon and vacuum. The bare NaTaO<sub>3</sub> material follows the same trend when is measured in different atmospheres and there are no significant differences between the presented spectra.

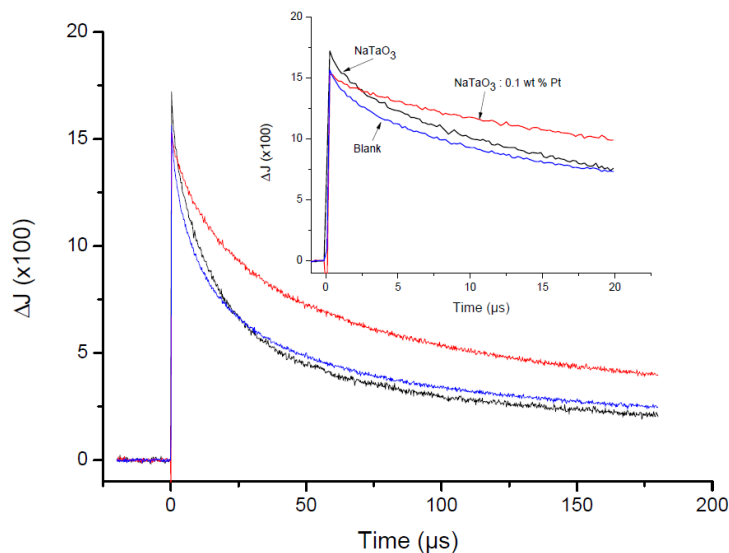
In table 5.3, the half lifetime of the photogenerated charge carriers in presence and absence of electron scavengers are resumed. The presence of air and molecular oxygen increases dramatically the decay of the observed signal. The systems were no sacrificial reagent was present, presented much slower decays, hence a longer half lifetime of the photogenerated charge carriers.

**Table 5.3:** Summary of the initial intensities ( $\Delta J_0$ ) and the half lifetimes ( $t_{1/2}$ ) of the transient absorption signals in air at 310 nm for undoped NaTaO<sub>3</sub> in air, O<sub>2</sub>, Ar and vacuum at 310 nm.

Atmosphere	$t_{1/2}$ ( $\mu$ s)	$\Delta J_0$ (x100)
Air	$17.2 \pm 0.1$	17
O <sub>2</sub>	$14.0 \pm 0.2$	19
Ar	$34.2 \pm 0.3$	15
Vacuum	$98 \pm 3$	12

#### 5.3.1.2.4 Platinum photodeposition

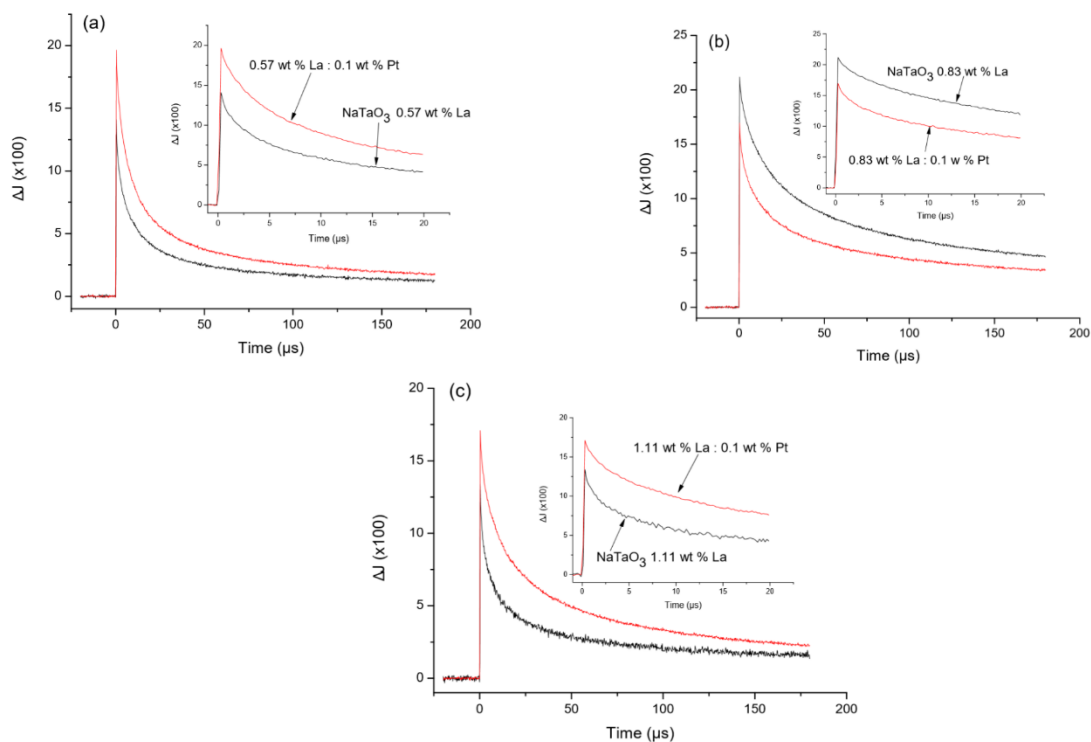
In order to minimize the recombination reaction between the photogenerated charge carriers, photodeposition of Pt nanoparticles performed on undoped and La-doped NaTaO<sub>3</sub> in air and the results are presented in the next figures.



**Figure 5.16:** Transient absorption signals for undoped  $\text{NaTaO}_3$  (black), 0.1 wt.%Pt doped  $\text{NaTaO}_3$  (red) in air at 310 nm. Inset: measurements during 20  $\mu\text{s}$ . Blank experiment performed using the same procedure as for the Pt photodeposition but without adding Pt to the system (blue).

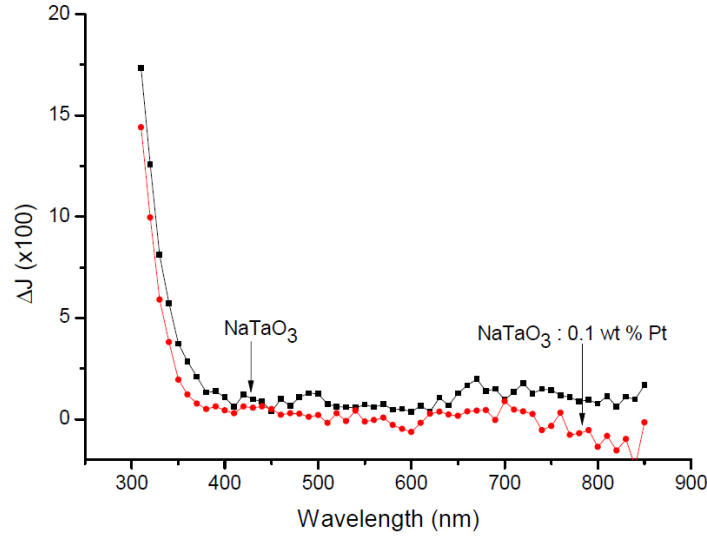
Fig. 5.16 presents the transient absorption signals for  $\text{NaTaO}_3$  before and after 0.1 wt.% Pt photodeposition. The blank measurement included in the figure belongs to an experiment performed following the same procedure as for Pt photodeposition (same amount of water, calcination time and temperature) but without the addition of platinum. This helps ensure that the procedure does not modify the material in any way other than the Pt photodeposition, and that the observed changes are due to the presence of Pt and not due to the presence of adsorbed molecules at the surface or morphological changes due to calcination.

Fig. 5.16 clearly shows that the photodeposition of platinum has an important effect on the behavior of the photogenerated charge carriers, slowing the decay and increasing the half-lifetime of the photogenerated charge carriers. Fig. 5.17 shows the results of the Pt photodeposition on La-doped  $\text{NaTaO}_3$  materials, in order to enlighten the effect of the Pt as a co-catalyst working when lanthanum is already present in the system.



**Figure 5.17:** Transient absorption signals of (a)  $\text{NaTaO}_3$  0.57 wt.% La, (b)  $\text{NaTaO}_3$  0.83 wt.% La and (c)  $\text{NaTaO}_3$  1.11 wt.% La before and after 0.1 wt.% Pt photodeposition measured in air at 310 nm. Inset: measurements during 20  $\mu\text{s}$ .

As shown in Fig. 5.12, the doping of  $\text{NaTaO}_3$  with 0.57 wt.% of lanthanum results in a faster decay of the signal, decreasing the lifetime of the photogenerated charge carriers. After photodeposition of 0.1 wt.% of Pt on the 0.57wt.% La-doped material the lifetime of the photogenerated charge carriers is found to be increased again (see Fig. 5.17 a). Moreover, the data presented in Fig. 5.12 showed that the material with a 0.83 wt.% La doping was the one that exhibits the highest initial intensity of the transient absorption signal and the slowest decay of all studied materials. Apparently, 0.83 wt.% La presents the optimum doping concentration of the investigated materials and for this, the loading of a co-catalyst may not have a considerable impact on the signal decay. In this case, the Pt loading has even a negative effect on the lifetime of the photogenerated charge carriers, resulting in faster decay of the transient absorption signal (see Fig. 5.17 b). The material with 1.11 wt.% La follows the same trend that the material with 0.57 wt.% La. The photodeposition of Pt in this case also increases the lifetime of the photogenerated charge carriers, slowing the signal decay. Fig. 5.18 shows the transient absorption spectra of bare  $\text{NaTaO}_3$  before and after the Pt photodeposition 20 ns after the laser pulse.



**Figure 5.18:** Transient absorption spectra for bare (black) and Pt-loaded (0.1 wt%) NaTaO<sub>3</sub> (red) in air 20 μs after laser excitation.

Fig. 5.18 shows the same trend that has been observed in all transient absorption spectra presented to this point; a signal at 310 nm and no other significant signals in the whole range of measured wavelengths (from 300 to 850 nm). Table 5.4 resumes the lifetime of the photogenerated charge carriers for all materials before and after Pt photodeposition.

**Table 5.4:** Summary of the initial intensities ( $\Delta J_0$ ) and the half lifetimes ( $t_{1/2}$ ) of the transient absorption signals in air at 310 nm for bare and La-doped NaTaO<sub>3</sub> before and after Pt photodeposition.

Material	$t_{1/2}$ ( $\mu$ s)	$\Delta J_0$ (x100)
NaTaO <sub>3</sub>	$17.2 \pm 0.1$	17
NaTaO <sub>3</sub> + 0.1 wt.%Pt	$44.0 \pm 0.1$	15
NaTaO <sub>3</sub> 0.57 wt.%La	$5.8 \pm 0.3$	14
NaTaO <sub>3</sub> 0.57 wt.%La + 0.1 wt.%Pt	$8.0 \pm 0.3$	20
NaTaO <sub>3</sub> 0.83 wt.%La	$27.7 \pm 0.4$	21
NaTaO <sub>3</sub> 0.83 wt.%La + 0.1 wt.%Pt	$17.0 \pm 0.2$	17
NaTaO <sub>3</sub> 1.11 wt.%La	$6.0 \pm 0.3$	13
NaTaO <sub>3</sub> 1.11 wt.%La + 0.1 wt.%Pt	$14.6 \pm 0.2$	17

For the undoped NaTaO<sub>3</sub> and materials doped with 0.57 and 1.11 wt.% of lanthanum the effect after Pt photodeposition follows the same trend. For these materials the introduction of Pt islands slowed the decay and increased the lifetime of the photogenerated charge carriers, suggesting that the electrons are being scavenged by the platinum. In the case of 0.83 wt.% La however, the opposite trend has been observed. This photocatalyst exhibited the slowest decay when no other sacrificial reagent was present in the system (see Fig. 5.12). The introduction of Pt leads however, to a much faster decay than the material without Pt photodeposition and therefore the lifetime of the photogenerated charge carriers decreases. For this material the Pt loading has a negative effect on the overall performance, suggesting a competition between the lanthanum (which presented the optimum doping of all investigated material) and the platinum.

### 5.3.1.3 Excitation in the presence of hole scavengers

#### 5.3.1.3.1 Methanol

The presence of a sacrificial system like an electron donor molecule can increase the molecular hydrogen production rate by scavenging the holes and therefore, the recombination rate and the back reaction to form H<sub>2</sub>O are reduced<sup>118</sup>. Alcohols have been widely used as hole scavengers, particularly methanol<sup>6</sup>. In this section, the effect of the addition of different amounts of methanol has been investigated. The measurements presented here were carried out using bare NaTaO<sub>3</sub> purged with argon in order to ensure that only the methanol was acting as hole scavenger.

Fig. 5.19 shows the transient absorption signals in argon at 310 nm when a range of different methanol amounts were added to the system (from 20 to 500  $\mu$ l). It has to be noted that each measurement has been made with a freshly prepared sample.



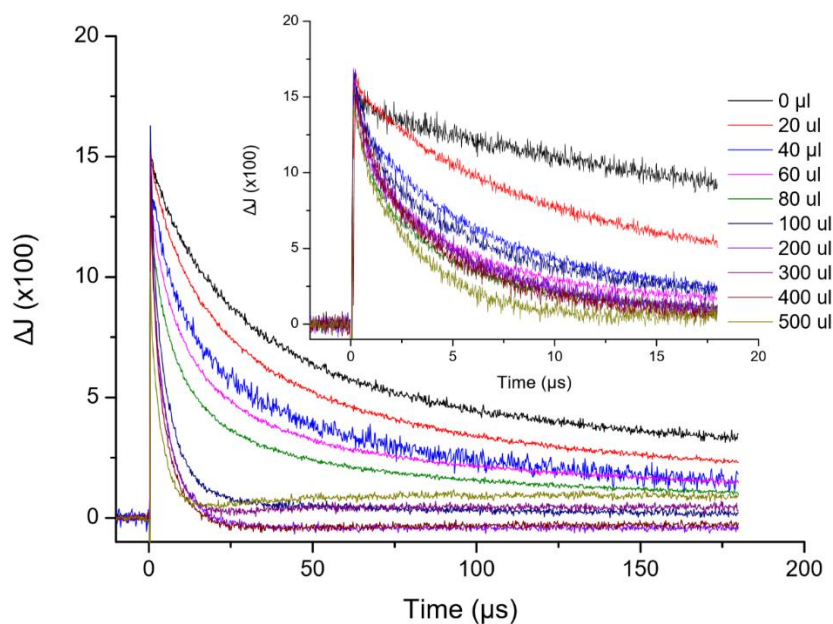


**Figure 5.19:** Transient absorption signals for bare  $\text{NaTaO}_3$  in Ar at 310nm after the addition of different amounts of methanol. Inset: measurements during 20  $\mu\text{s}$ .

As Fig. 5.19 shows, the addition of methanol has a big effect on the signal decay. After the addition from 20 to 80  $\mu\text{l}$  of methanol, the transient signal decay becomes progressively faster. The fastest change however, is observed after the addition of 100  $\mu\text{l}$  of methanol. With higher methanol concentrations (from 200 to 500  $\mu\text{l}$ ) the powders start to become very wet and the materials agglomerate and difficult the measurements. Therefore, it can be said in a first approximation that the photogenerated charge carriers responsible for the observed signal at 310 nm have a shorter lifetime with increasing methanol concentration (hole scavenger). In Fig. 5.20 the transient absorption spectra for bare  $\text{NaTaO}_3$  in argon are shown before and after the addition of 100  $\mu\text{l}$  of methanol.

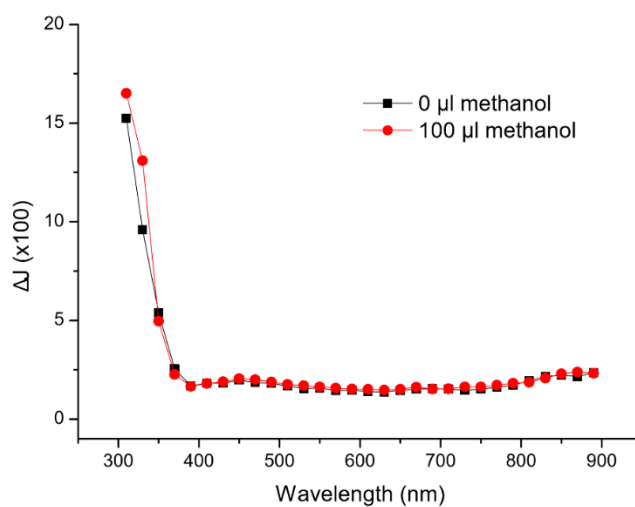


**Figure 5.20:** Transient absorption spectra 20  $\mu\text{s}$  after laser irradiation for bare  $\text{NaTaO}_3$  in Ar, before (black) and after (red) 100  $\mu\text{l}$  of methanol addition.

As Fig. 5.20 shows, the initial transient absorption spectra of the bare material with and without methanol do not exhibit any big differences. For an easier comparison between the decay of signals with different methanol amounts, the lifetime of the photogenerated charge carriers can be observed in Table 5.5.

**Table 5.5:** Summary of the initial intensities ( $\Delta J_0$ ) and the half lifetimes ( $t_{1/2}$ ) of the transient absorption signals in argon at 310 nm for bare NaTaO<sub>3</sub> after the addition of different amounts of methanol.

Methanol ( $\mu\text{l}$ )	$t_{1/2}$ ( $\mu\text{s}$ )	$\Delta J_0(\times 100)$
0	$34.0 \pm 0.3$	15
20	$23.0 \pm 0.3$	15
40	$13.3 \pm 0.2$	15
60	$11.4 \pm 0.1$	14
80	$7.2 \pm 0.1$	14
100	$2.6 \pm 0.2$	16
200	$2.0 \pm 0.2$	15
300	$1.8 \pm 0.2$	15
400	$2.0 \pm 0.4$	14

Table 5.5 shows how the half lifetimes of the photogenerated charge carriers progressively decreases with increasing amount of methanol. This suggests that the observed signal at 310 nm belongs to the photogenerated holes.

### 5.3.1.3.2 Other alcohols

Other alcohols besides methanol such as ethanol and 2-propanol have been shown to also act as efficient hole scavengers. Tamaki *et al.*<sup>96</sup> reported that the total amount of adsorbed alcohol decreases with the higher dimensions of the alcohol molecules in the following order: methanol > ethanol > 2-propanol. In this work, experiments using ethanol, 2-propanol and tert-butanol were therefore performed employing bare NaTaO<sub>3</sub> in argon, following the same steps as for methanol addition. The respective transient signals at 310 nm are shown in Fig. 5.21.

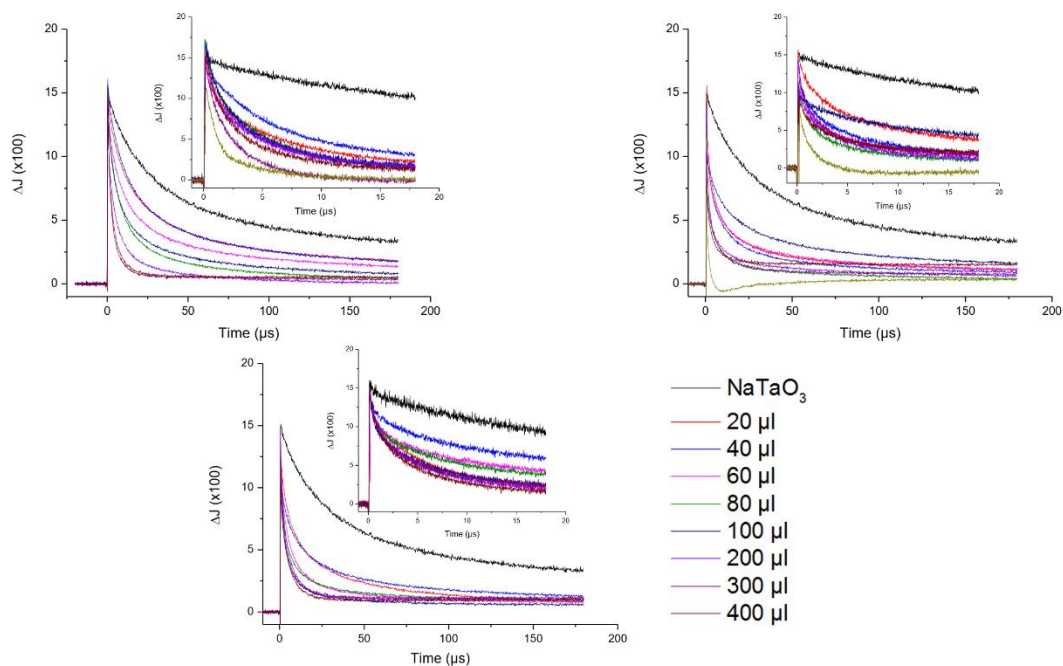


**Figure 5.21:** Transient absorption signals for undoped  $\text{NaTaO}_3$  in Ar with different amounts of (a) ethanol, (b) 2-propanol and (c) tert-butanol at 310 nm. Inset: measurements during 20  $\mu\text{s}$ .

As Fig. 5.21 shows, the transient signals were influenced in the same way when ethanol, 2-propanol and tert-butanol were introduced into the system, as when methanol was used. In all cases the signals presented a faster decay with increasing alcohol addition, shortening the lifetime of the photogenerated charge carriers. However, not only the alcohol amount plays a role in the lifetime of the species but the type of alcohol seems to have an impact on the decay. Looking at the Fig. 5.21, differences can be observed even after the addition of 20  $\mu\text{l}$  of alcohol. After the same alcohol concentration has been added, the signal decay becomes faster for alcohols with longer chain length. Therefore, the lifetime of the photogenerated charge carriers is shorter when tert-butanol was used instead of alcohols with less than four carbon atoms in the chain. The half lifetimes for the photogenerated charge carriers after the addition of different amounts of alcohols are compiled in Table 5.6.

**Table 5.6:** Summary of the half lifetimes ( $t_{1/2}$ ) of the transient absorption signals in argon at 310 nm for bare NaTaO<sub>3</sub> after the addition of different amounts of ethanol, 2-propanol and tert-butanol.

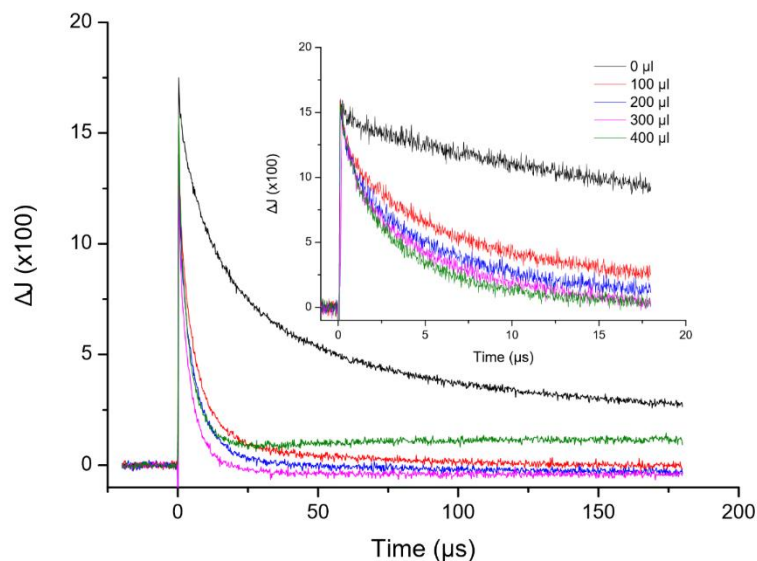
Amount ( $\mu\text{l}$ )	$t_{1/2}$ ( $\mu\text{s}$ )		
	Ethanol	2-Propanol	Tert-Butanol
0	$34.0 \pm 0.3$	$34.0 \pm 0.3$	$34.0 \pm 0.3$
20	$13.8 \pm 0.3$	$3.2 \pm 0.2$	$7.4 \pm 0.2$
40	$13.4 \pm 0.2$	$3.2 \pm 0.3$	$7.6 \pm 0.2$
60	$8.6 \pm 0.2$	$6.8 \pm 0.2$	$3.0 \pm 0.1$
80	$4.9 \pm 0.2$	$1.6 \pm 0.1$	$2.1 \pm 0.1$
100	$4.1 \pm 0.1$	$17.2 \pm 0.2$	$2.4 \pm 0.1$
200	$3.0 \pm 0.2$	$3.6 \pm 0.3$	$2.0 \pm 0.1$
300	$2.0 \pm 0.1$	$2.6 \pm 0.2$	$2.2 \pm 0.1$
400	$1.1 \pm 0.2$	$2.0 \pm 0.1$	$2.0 \pm 0.1$

Table 5.6 clearly shows the changes in the half-lifetimes on the undoped NaTaO<sub>3</sub> when alcohols with different chain lengths were used. The  $t_{1/2}$  decays faster when alcohols with longer chain lengths were added. One of the main differences when using methanol or other alcohols is that with methanol the biggest change in  $t_{1/2}$  occurs when 100  $\mu\text{l}$  methanol were added. However, when ethanol, 2-propanol or tert-butanol were used, a dramatic decrease in the signal decay can be observed already after adding 20 or 40  $\mu\text{l}$  of the alcohol.

#### 5.3.1.4 Excitation in the simultaneous presence of electron and hole scavengers

The results presented in the previous sections have shown the behavior of the photogenerated charge carriers when only an electron donor or acceptor was added to the system. In this section are presented the results of measurements performed when O<sub>2</sub> (electron acceptor) and methanol (electron donor) are present simultaneously in the system for undoped NaTaO<sub>3</sub>.

Fig. 5.22 shows the transient absorption signals at 310 nm for bare NaTaO<sub>3</sub> in air when different amounts of methanol were added to the system. It has to be noted that each measurement was performed using a freshly prepared sample.



**Figure 5.22:** Transient absorption signals at 310 nm for bare  $\text{NaTaO}_3$  in air after different amounts of methanol were added. Inset: measurements during 20  $\mu\text{s}$ .

The comparison of Fig. 5.19 and Fig. 5.22 shows that the addition of methanol does not lead to any big changes for systems in air or purged with argon. In the case where both an electron and a hole scavenger are present (methanol and air), the addition of 100  $\mu\text{l}$  of methanol translates in a dramatic fast decrease in the signal decay and a shorter lifetime of the photogenerated charge carriers (see Fig. 5.22 and table 5.7). Such a big difference cannot be observed with increasing methanol amounts. In Table 5.7 are presented the half lifetimes for the photogenerated charge carriers in air and in argon with increasing methanol concentrations.

**Table 5.7:** Summary of the half lifetimes ( $t_{1/2}$ ) of the transient absorption signals in air at 310 nm for bare  $\text{NaTaO}_3$  after the addition of different amounts of methanol.

Amount ( $\mu\text{l}$ )	$t_{1/2}$ ( $\mu\text{s}$ )	
	Air	Ar
0	$17.2 \pm 0.1$	$34.0 \pm 0.3$
100	$2.8 \pm 0.2$	$2.6 \pm 0.2$
200	$2.0 \pm 0.2$	$2.0 \pm 0.2$
300	$1.8 \pm 0.2$	$1.8 \pm 0.2$
400	$2.0 \pm 0.2$	$2.0 \pm 0.4$

As the table 5.7 shows, the main difference between the measurements in air and in argon occur when no alcohol was present in the system. The addition of methanol does not lead to a big difference between  $t_{1/2}$ . In both cases, the presence of methanol produces a dramatic decrease in the half lifetime of the photogenerated charge carriers and faster decays of the measured signals.

Fig. 5.23 illustrates the effect of the methanol addition on undoped NaTaO<sub>3</sub> when molecular oxygen was purged into the system and compares it with the measurements in air.

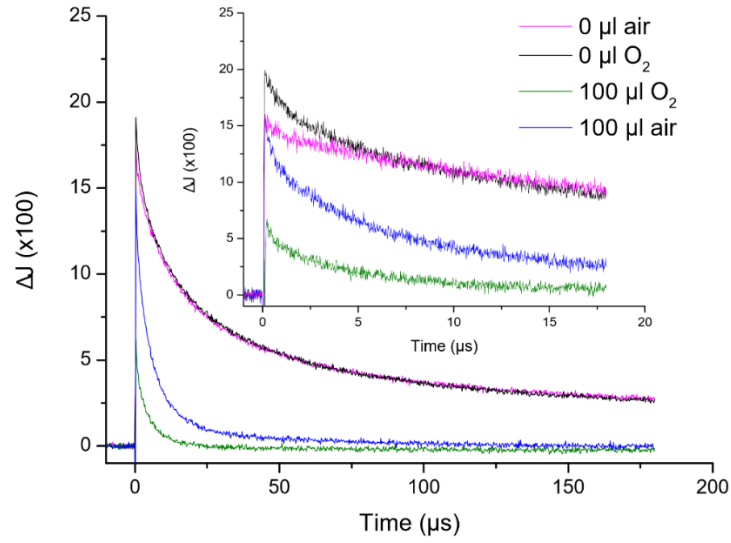


**Figure 5.23:** Transient absorption signals for bare NaTaO<sub>3</sub> at 310 nm in air and O<sub>2</sub> before and after addition of 100 µl of methanol. Inset: measurements during 20 µs.

As Fig. 5.23 shows, the addition of 100 µl of methanol when the atmosphere was purged with molecular oxygen presents a signal with a much lower absorption intensity and a faster kinetic decay of the photogenerated species than the signal with methanol in air. In Table 5.8 are resumed the lifetimes for the photogenerated species of bare NaTaO<sub>3</sub> in air and under oxygen saturated atmosphere at 310 nm.

**Table 5.8:** Summary of the half lifetimes ( $t_{1/2}$ ) of the transient absorption signals in air and O<sub>2</sub> at 310 nm for bare NaTaO<sub>3</sub> before and after the addition of 100 µl of methanol.

Amount (µl)	$t_{1/2}$ (µs)	
	Air	O <sub>2</sub>
0	$17.2 \pm 0.1$	$14.0 \pm 0.2$
100	$2.8 \pm 0.2$	$1.8 \pm 0.2$

### 5.3.2 Sub-band gap excitation with UV(A) light

In the next section are presented the results of the measurements performed for bare and lanthanum doped NaTaO<sub>3</sub> powders when a laser excitation wavelength of 351 nm was used. The band gap of NaTaO<sub>3</sub> is 4.0 eV (see section 4.4.1), and irradiation with 351 nm corresponds to an energy of 3.5 eV that is lower than the band gap of the semiconductor. All measurements presented in this section were performed three times with freshly prepared samples.

### 5.3.2.1 Excitation in the absence of sacrificial reagents

Fig. 5.24 shows the transient absorption spectra of bare and La-doped NaTaO<sub>3</sub> in argon. The spectra were recorded from 400 to 890 nm. For the undoped NaTaO<sub>3</sub>, the measured signal has an absorption intensity from 2.0 to 2.5 and does not go to zero. However, three overlapping peaks can be differentiated at 450, 690 and 890 nm. With increasing lanthanum doping these peaks become less pronounced and the one at 890 nm is the only one remaining visible for all materials, though with different absorption intensities.

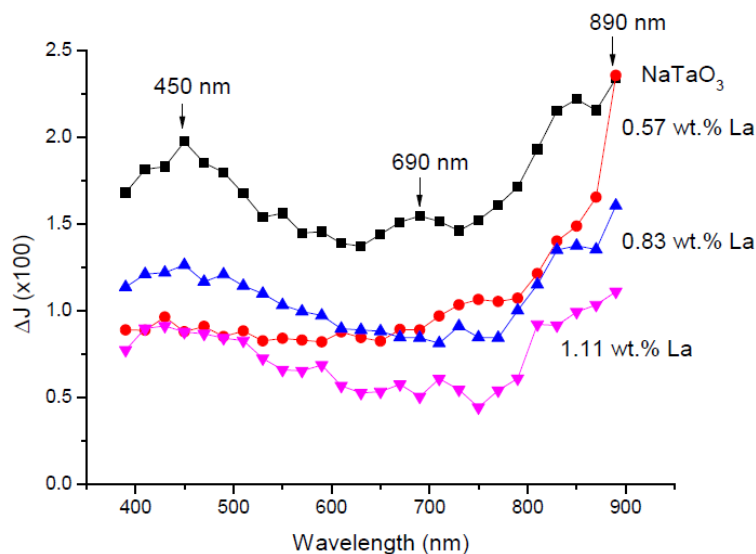


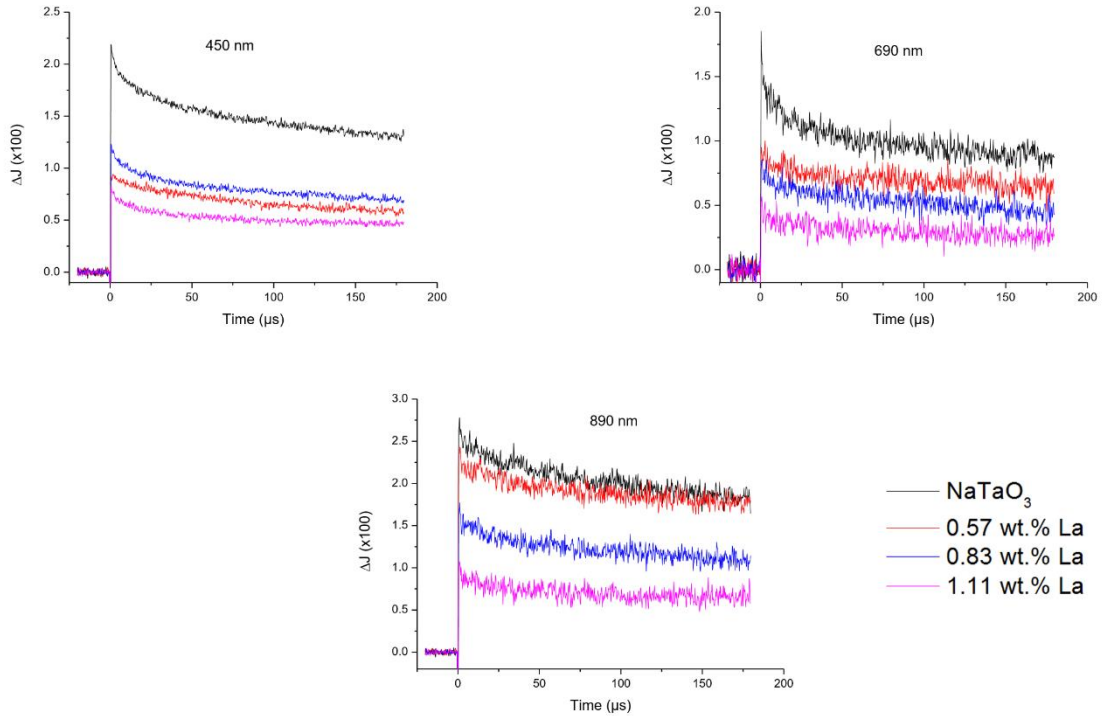
**Figure 5.24:** Transient absorption spectra of bare and lanthanum doped NaTaO<sub>3</sub> in argon measured 20 μs after laser excitation.

Doping with 0.57 wt.% of lanthanum provokes that the absorption intensity of the peak at 450 nm is reduced in half and keeps on reducing with increasing lanthanum doping. The same trend can be observed for the peaks at 690 and 890 nm. In all cases, the absorption intensity decreases with increasing lanthanum concentration. In Fig. 5.25, these three wavelengths will be examined in more detail by plotting the transient absorption signals for undoped and lanthanum doped NaTaO<sub>3</sub>. Table 5.9 summarizes the  $t_{2/3}$  of the photogenerated charge carriers for bare and La-doped NaTaO<sub>3</sub> in argon. In this section, as the signal decay is slower than for the signals obtained with the 248 nm laser excitation wavelength,  $t_{2/3}$  has been calculated instead of  $t_{1/2}$ . The method employed for the calculations is explained in Fig. 5.7.

**Table 5.9:** Summary of the  $t_{2/3}$  of the photogenerated charge carriers for undoped and lanthanum doped NaTaO<sub>3</sub> in argon at 450, 690 and 890 nm (taken from Fig. 5.25).

Wavelength(nm)	$t_{2/3}$ ( $\mu\text{s}$ )			
	Undoped	0.57 wt.% La	0.83 wt.% La	1.11 wt.% La
450	$94 \pm 1$	$138 \pm 2$	$72 \pm 1$	$39 \pm 3$
690	$13 \pm 2$	$> 179$	$74 \pm 1$	$7 \pm 2$
890	$\approx 179$	$> 179$	$42 \pm 2$	$25 \pm 2$

As Table 5.9 shows, the signal at 450 nm presents longer  $t_{2/3}$  when 0.57 wt.% of La was doped into the system, going from 94 (undoped NaTaO<sub>3</sub>) to 138  $\mu\text{s}$ . A subsequent increase of the lanthanum amount in the material however, does not follow the same trend and the addition of 0.83 and 1.11 wt.% of La shortened the  $t_{2/3}$  and increased the transient absorption signal decay (see Fig. 5.25), to 72 and 39  $\mu\text{s}$  respectively.

**Figure 5.25:** Transient absorption signals of undoped and lanthanum doped NaTaO<sub>3</sub> in argon at (a) 450 nm, (b) 690 nm and (c) 890 nm.

The signal at 690 nm presents a dramatic increase of  $t_{2/3}$  when 0.57 wt.% of La was doped, going from 13 (undoped NaTaO<sub>3</sub>) to  $>179$   $\mu\text{s}$  which corresponds to the slowest kinetic decay of all materials for this wavelength (Fig. 5.25). Increasing the lanthanum doping leads to a decrease in  $t_{2/3}$  and faster signal decays are observed (Fig. 5.25), following the same trend observed for the signals at 450 nm.

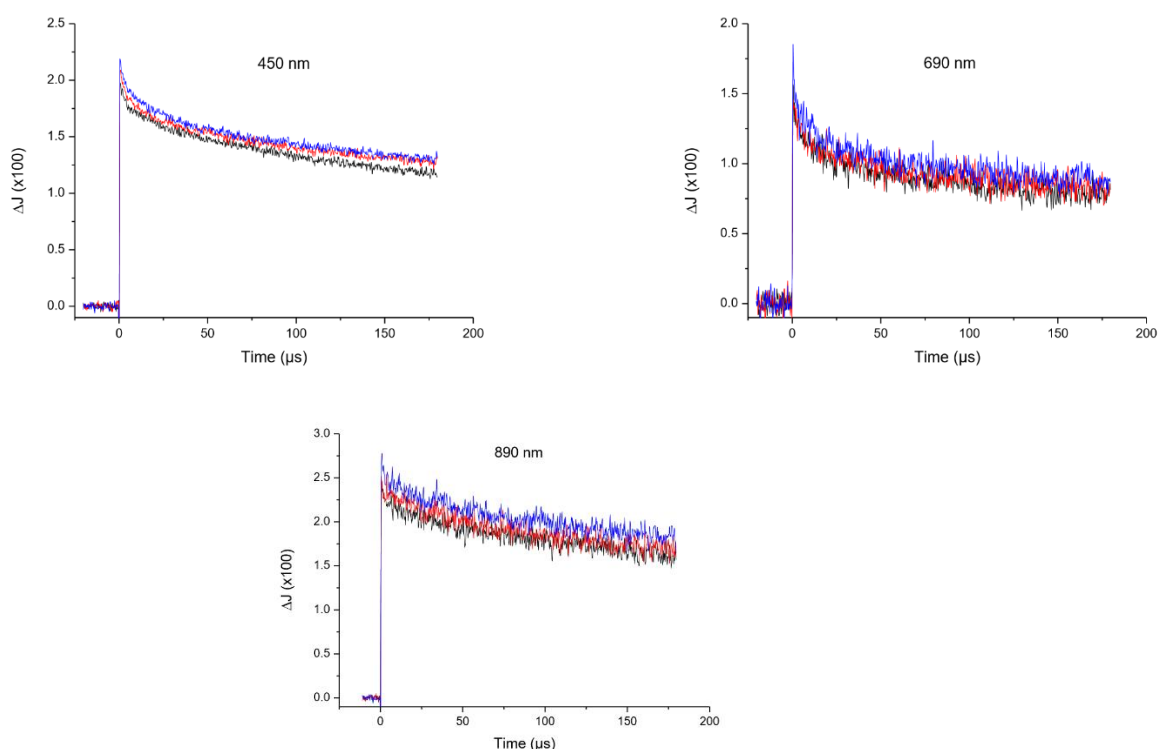


The signal at 890 nm exhibits a slightly different behavior. In this case, the undoped NaTaO<sub>3</sub> already exhibits a high  $t_{2/3}$  ( $>179 \mu\text{s}$ ) and the doping with 0.57 wt.% of lanthanum does not produce any significant changes in the transient absorption decay. However, following the same trend as for the other two wavelengths, the increasing amount of lanthanum doped into the system shortens  $t_{2/3}$  and faster signal decays can be observed (see Fig. 5.25 and Table 5.9).

### 5.3.2.2 Excitation in the presence of electron scavengers

#### 5.3.2.2.1 Bare NaTaO<sub>3</sub> in air and in a molecular O<sub>2</sub> purged atmosphere

Next are presented the results of the measurements for undoped NaTaO<sub>3</sub> in the presence of electron scavengers.



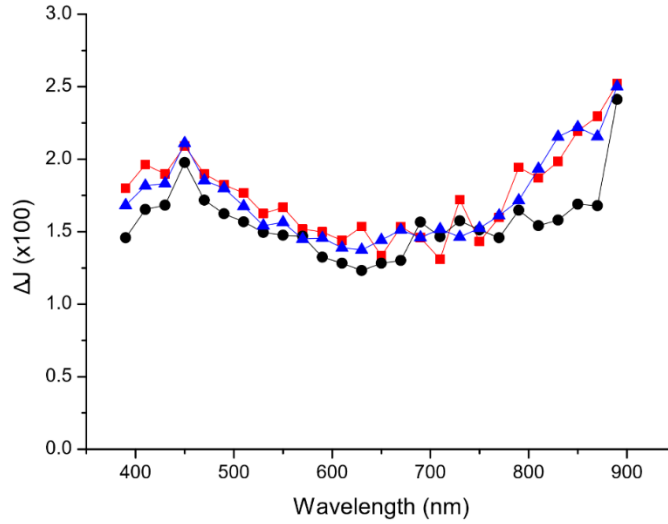
**Figure 5.26:** Transient absorption signals of undoped NaTaO<sub>3</sub> measured in air (black), molecular oxygen (red) and argon (blue) at (a) 450 nm, (b) 690 nm and (c) 890 nm.

Fig. 5.26 shows the transient absorption signals for undoped NaTaO<sub>3</sub> in air, molecular oxygen and argon at 450, 690 and 890 nm. The signal decay for the measurements performed in argon are slightly slower than the decays in air and molecular oxygen, although the differences are not very significant. The lifetimes of the photogenerated charge carriers for bare NaTaO<sub>3</sub> in air and molecular oxygen purging are compiled in Table 5.10.

**Table 5.10:** Summary of  $t_{2/3}$  of the photogenerated charge carriers for undoped NaTaO<sub>3</sub> in air, molecular oxygen and argon at 450, 690 and 890 nm (taken from Fig. 5.26).

Wavelength(nm)	$t_{2/3}$ ( $\mu$ s)		
	Ar	Air	O <sub>2</sub>
450	$94 \pm 1$	$100 \pm 1$	$94 \pm 1$
690	$13 \pm 2$	$19 \pm 2$	$27 \pm 3$
890	$\approx 179$	$\approx 179$	$> 179$

As Table 5.10 shows, the calculated  $t_{2/3}$  in air and molecular oxygen are slightly higher than in argon. This could be due to the fact that the observed signals belong to photogenerated holes which live longer once the photogenerated electrons have been scavenged by the oxygen atoms. In all three atmospheres, the measurements at 890 nm exhibit a very long  $t_{2/3}$  ( $\approx 179$  or higher). Fig. 5.27 shows the transient absorption spectra for undoped NaTaO<sub>3</sub> in air, molecular oxygen and argon.



**Figure 5.27:** Transient absorption spectra 20  $\mu$ s after laser irradiation of bare NaTaO<sub>3</sub> in air (black), molecular oxygen (red) and argon (blue).

From fig. 5.27 it is evident that there are no big differences between the illustrated transient absorption spectra. The spectrum measured in air presents slightly lower absorption intensity than the spectra measured for molecular oxygen and argon, which follow a very similar trend.

### 5.3.2.2.2 Lanthanum doped NaTaO<sub>3</sub> in air

In this section, the results of the measurements using lanthanum doped NaTaO<sub>3</sub> in air are presented.

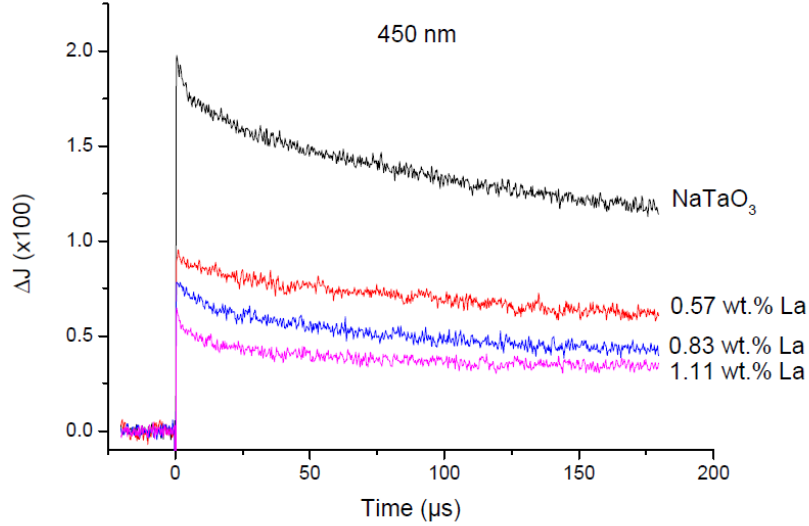


**Figure 5.28:** Transient absorption signals for bare and lanthanum doped NaTaO<sub>3</sub> in air at 450 nm.

Fig. 5.28 shows the transient absorption signals for bare and lanthanum doped NaTaO<sub>3</sub> in air at 450 nm. The undoped material shows the highest absorption intensity from all investigated materials at 450 nm and with increasing lanthanum doping, the absorption intensity of the signals decreases. The signal decay however, does not follow the same trend. The materials with 0.83 and 1.11 wt.% of lanthanum present faster signal decays than the undoped NaTaO<sub>3</sub> and the 0.57 wt.% La material. The summary of  $t_{2/3}$  for the signals in Fig. 5.28 is summarized in Table 5.11 and compared to the decays in argon (taken from Table 5.9).

**Table 5.11:** Summary of  $t_{2/3}$  of the photogenerated charge carriers for bare and La-doped NaTaO<sub>3</sub> in air and argon at 450 nm.

Material	$t_{2/3}$ ( $\mu$ s)	
	Ar	Air
NaTaO <sub>3</sub>	$94 \pm 1$	$100 \pm 1$
NaTaO <sub>3</sub> 0.57 wt.% La	$138 \pm 2$	$113 \pm 2$
NaTaO <sub>3</sub> 0.83 wt.% La	$72 \pm 1$	$64 \pm 1$
NaTaO <sub>3</sub> 1.11 wt.% La	$39 \pm 3$	$25 \pm 1$

As Table 5.11 shows, the calculations for  $t_{2/3}$  differ between argon and air. In argon the material doped with 0.83 wt.% of lanthanum presents the longest  $t_{2/3}$  of all investigated materials (including undoped NaTaO<sub>3</sub>). However, when the measurements were performed

in air this is not the case. The bare  $\text{NaTaO}_3$  and the material doped with 0.57 wt.% of La exhibit a very similar signal decay. This signal decay decreases with increasing lanthanum concentration.

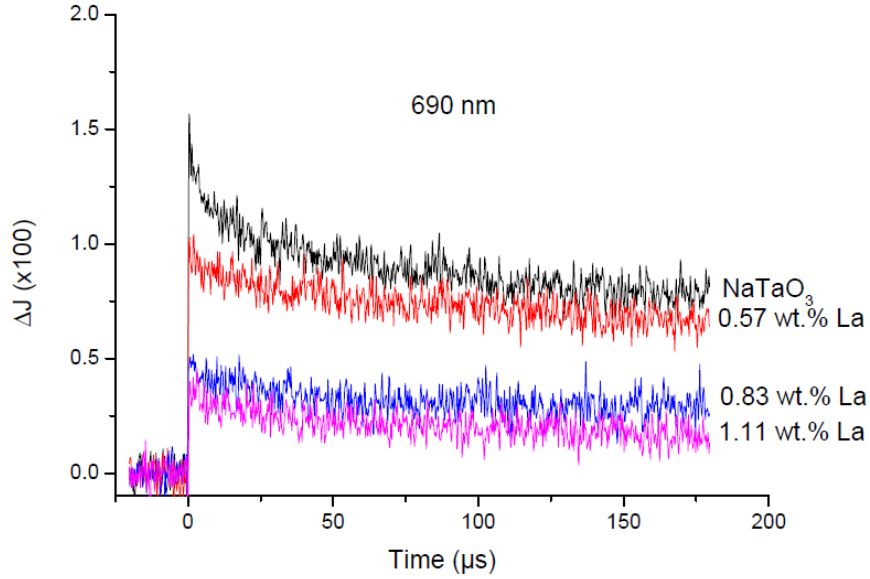


**Figure 5.29:** Transient absorption signals for bare and lanthanum doped  $\text{NaTaO}_3$  measured at 690 nm in air.

As Fig. 5.24 showed, the signal at 690 nm is the one that suffered more drastically the impact of the lanthanum doping, being significantly diminished after 0.57 wt.% of lanthanum was doped in the system and it can be more clearly seen in Fig. 5.29. The absorption intensity of the signals decreases significantly with increasing lanthanum doping.

**Table 5.12:** Summary of  $t_{2/3}$  of the photogenerated charge carriers for bare and La-doped  $\text{NaTaO}_3$  in air and argon at 690 nm.

Material	$t_{2/3}$ ( $\mu\text{s}$ )	
	Ar	Air
$\text{NaTaO}_3$	$13 \pm 2$	$19 \pm 2$
$\text{NaTaO}_3$ 0.57 wt.% La	$> 179$	$\approx 179$
$\text{NaTaO}_3$ 0.83 wt.% La	$74 \pm 1$	$32 \pm 3$
$\text{NaTaO}_3$ 1.11 wt.% La	$7 \pm 2$	$7 \pm 2$

Table 5.12 shows that in argon, the same trend can be observed at 690 and 450 nm, where the signal for the material doped with 0.57 wt.% of lanthanum presents the longest  $t_{2/3}$  (slowest signal decay) of all the investigated materials. In air, as it has been shown in Fig. 5.24 and Fig. 5.29, the addition of lanthanum has a big effect on the absorption intensity and decay of the signal for the 0.57 wt.% La doped material, increasing the lifetime of the

photogenerated charge carriers. The sample with 0.57 wt.% La presents the slowest signal decay (highest  $t_{2/3}$ ), whilst the other materials have rather fast decays.

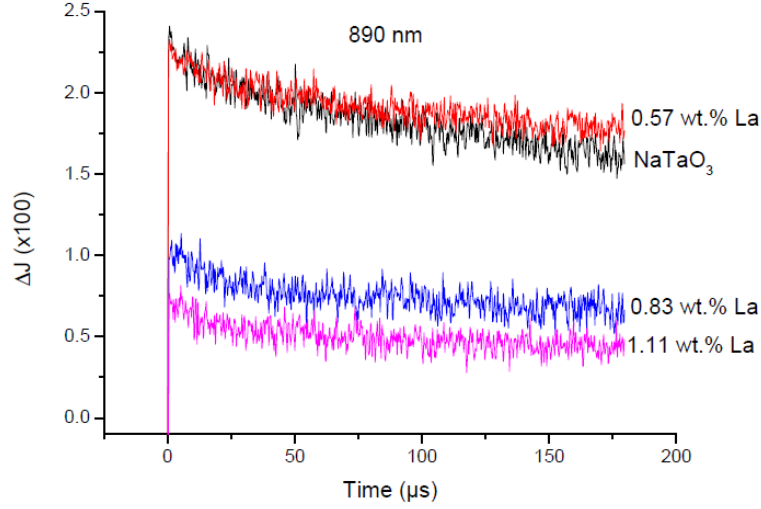


**Figure 5.30:** Transient absorption signals for bare and lanthanum doped  $\text{NaTaO}_3$  measured at 890 nm in air.

Finally, the signals at 890 nm present higher absorption intensities for all investigated materials than at 450 and 690 nm (see Fig. 5.24 and Fig. 5.30). In this case, the undoped  $\text{NaTaO}_3$  and the material doped with 0.57 wt.% La follow a very similar trend and have similar signal decays (see Table 5.13). The absorption intensity of the signals decreases with increasing lanthanum concentration and the signal decay becomes faster, indicating shorter lifetime for the photogenerated charge carriers with increasing lanthanum doping. In Table 5.13 are summarized the  $t_{2/3}$  of the photogenerated charge carriers in air at 890 nm for bare and La-doped  $\text{NaTaO}_3$ .

**Table 5.13:** Summary of  $t_{2/3}$  of the photogenerated charge carriers for bare and La-doped  $\text{NaTaO}_3$  in air and argon at 890 nm.

Material	$t_{2/3}$ ( $\mu\text{s}$ )	
	Ar	Air
$\text{NaTaO}_3$	$\approx 179$	$\approx 179$
$\text{NaTaO}_3$ 0.57 wt.% La	$> 179$	$> 179$
$\text{NaTaO}_3$ 0.83 wt.% La	$42 \pm 2$	$40 \pm 1$
$\text{NaTaO}_3$ 1.11 wt.% La	$25 \pm 2$	$20 \pm 1$

The material doped with 0.57 wt.% La exhibits a very long  $t_{2/3}$  of the photogenerated charge carriers (higher than the measured range), followed by the undoped material. Afterwards with increasing lanthanum concentration the lifetime decreases gradually.

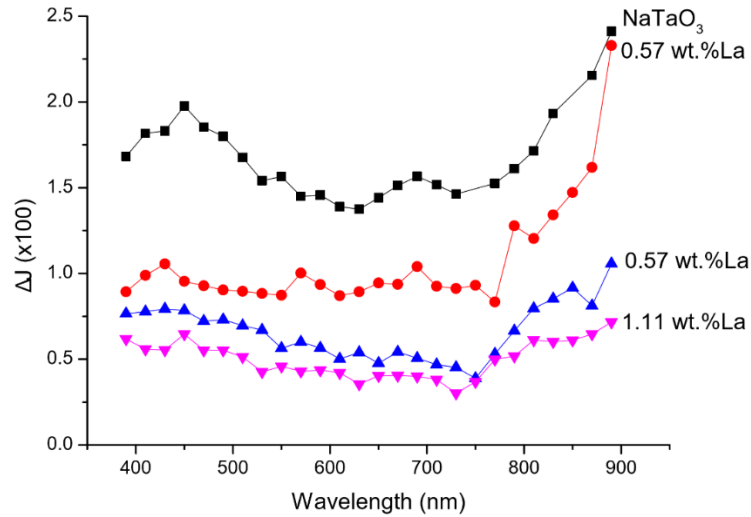


**Figure 5.31:** Transient absorption spectra 20  $\mu$ s after laser irradiation of bare and lanthanum doped NaTaO<sub>3</sub> in air.

In Fig. 5.31 the transient absorption spectra in air for bare and lanthanum doped NaTaO<sub>3</sub> 20  $\mu$ s after laser excitation is shown. The lanthanum doping does have an effect on the observed three signals at 450, 690 and 890 nm. The signal at 450 nm is still visible when a doping amount of 0.57 wt.% of lanthanum is present in the system, however, it flattens with increasing lanthanum doping. The signal at 690 nm is the one that exhibited a more drastic effect of the lanthanum doping, decreasing its absorption intensity after doping with 0.57 wt.% of lanthanum. Finally, the peak at 890 nm is still visible after all lanthanum additions although decreasing its intensity with increasing lanthanum amount.

### 5.3.2.2.3 Lanthanum doped NaTaO<sub>3</sub> in a molecular oxygen purged atmosphere

Fig. 5.32 shows the transient absorption signals for the lanthanum doped materials in molecular oxygen at 450, 690 and 890 nm.

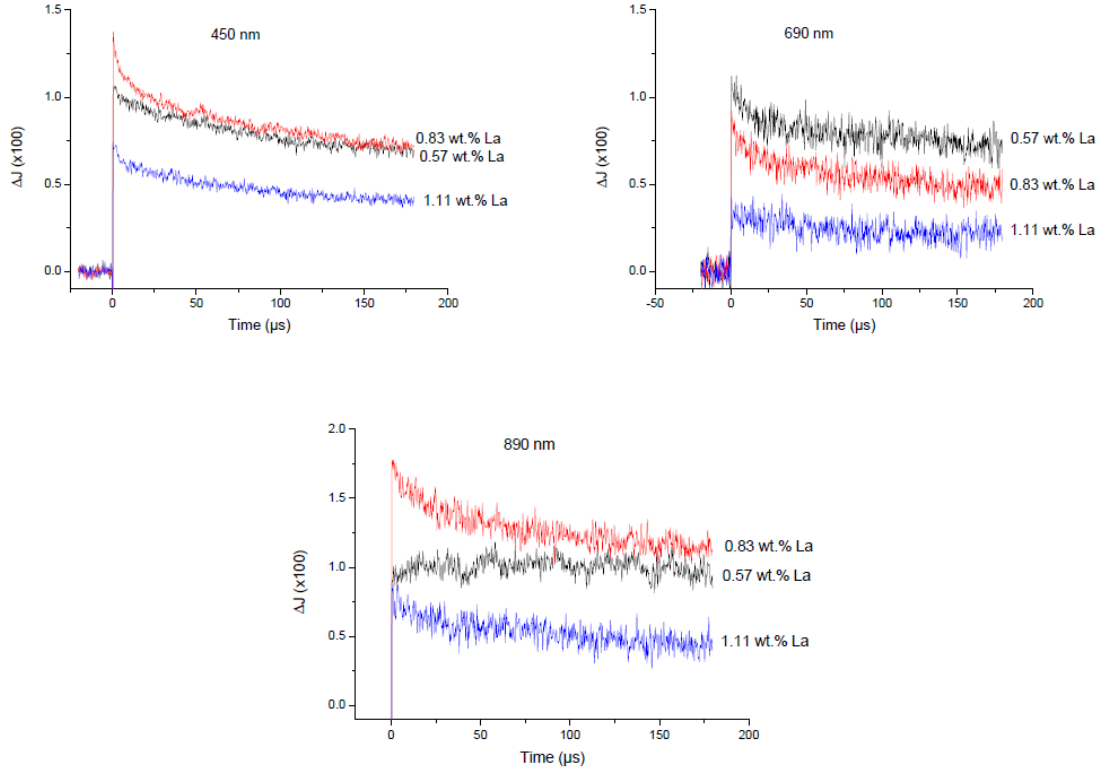


**Figure 5.32:** Transient absorption signals of La-doped NaTaO<sub>3</sub> in oxygen. (a) 450 nm, (b) 690 nm and (c) 890 nm.

Fig. 5.32 shows the effect of molecular oxygen on the lanthanum doped materials. The measurements at 450 and 890 nm show that the material doped with 0.83 wt.% of La presents the highest absorption intensity of all investigated materials. However, the measurement at 690 nm does not show the same trend. In this case, the highest absorption intensity corresponds to the material with 0.57 wt.% La. The Table 5.14 summarizes the calculated  $t_{2/3}$  of the signals presented in Fig. 5.32.

**Table 5.14:** Summary of  $t_{2/3}$  of the photogenerated charge carriers for bare and La-doped NaTaO<sub>3</sub> in molecular oxygen at 450, 690 and 890 nm.

Material	$t_{2/3}$ ( $\mu$ s)		
	450 nm	690 nm	890 nm
NaTaO <sub>3</sub>	94 $\pm$ 1	27 $\pm$ 3	>179
NaTaO <sub>3</sub> 0.57 wt.% La	150 $\pm$ 1	50 $\pm$ 1	>179
NaTaO <sub>3</sub> 0.83 wt.% La	40 $\pm$ 2	35 $\pm$ 1	75 $\pm$ 1
NaTaO <sub>3</sub> 1.11 wt.% La	50 $\pm$ 2	7 $\pm$ 1	20 $\pm$ 1

Table 5.14 shows that, at 450 nm, doping with 0.57 wt.% of La increased the lifetime of the photogenerated charge carriers, slowing down the signal decay (see Fig.5.32). Doping with 0.83 wt.% La has the contrary effect and decreases drastically the calculated lifetime down to 40  $\mu\text{s}$ . The material with 0.83 wt.% La presents the fastest signal decay of all investigated materials at 450 nm.

The signal at 690 nm presents a very fast decay and a short lifetime (27  $\mu\text{s}$ ) for the undoped material. Doping with 0.57 and 0.83 wt.% of La increases the lifetime of the photogenerated charge carriers and slows down the signal decay (see Fig. 5.32 and Table 5.14). However, the material doped with 1.11 wt.% of La, exhibits a very fast decay and the shortest lifetime (7  $\mu\text{s}$ ) of the measurements at 690 nm.

Finally, the signal at 890 nm exhibits a totally different behavior. The undoped  $\text{NaTaO}_3$  and the material doped with 0.57 wt.% of La present a very long lifetime of the photogenerated charge carriers ( $>179 \mu\text{s}$ ), which decreases with increasing lanthanum concentration (see Table 5.14).

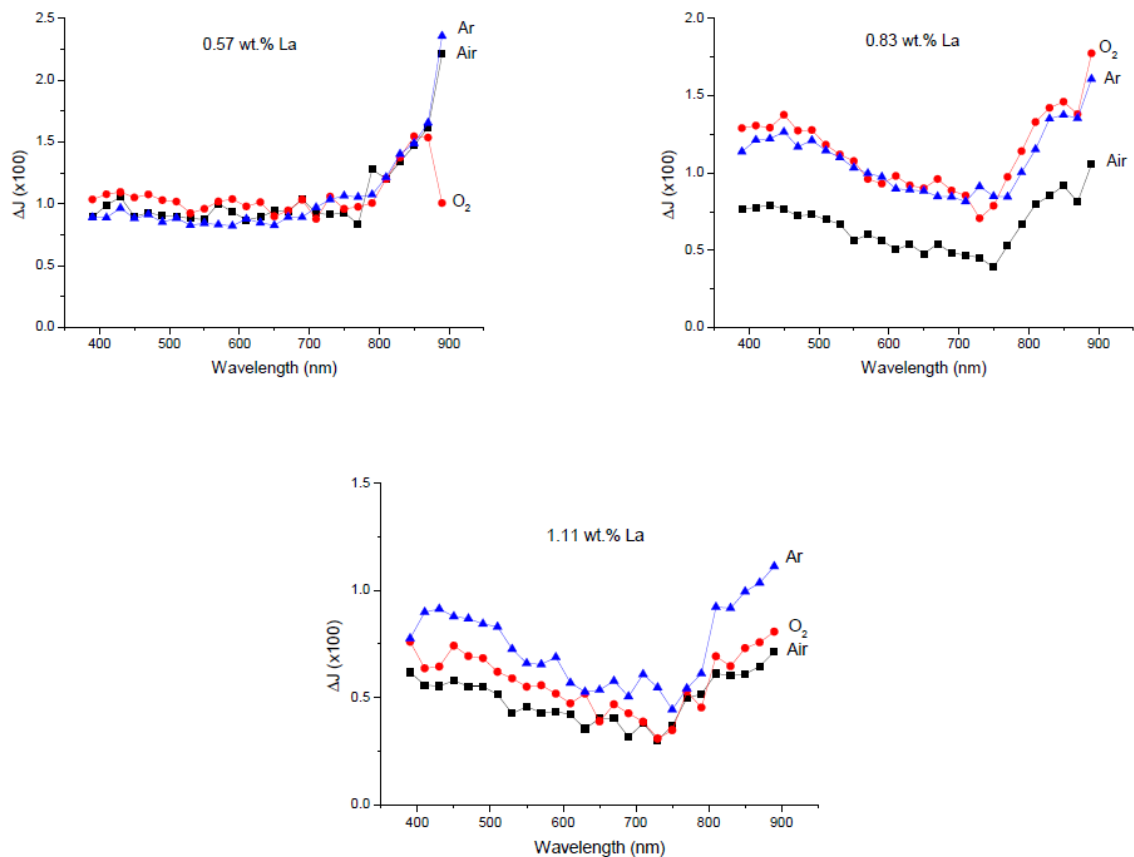


**Figure 5.33:** Transient absorption spectra 20  $\mu\text{s}$  after laser irradiation of La-doped  $\text{NaTaO}_3$  in oxygen. (a) 0.57 wt.% La, (b) 0.83 wt.% La and (c) 1.11 wt.% La.



Fig. 5.33 shows that the transient absorption spectra in all three atmospheres differ very lightly from each other. The sample doped with 0.57 wt.% La exhibit almost no change in the whole measured range (from 400 to 890 nm). The only difference can be observed at 890 nm, where the signal for argon and air is very but the one measured in molecular oxygen presents a much lower absorption intensity.

The material doped with 0.83 wt.% La presents the same shape for all three spectra, with the only difference in the absorption intensity. The spectrum in air has lower absorption intensity than the spectra for argon and O<sub>2</sub>.

Lastly, the sample doped with 1.11 wt.% La presents approximately the same trend in all three atmospheres as well. It has to be noted that in this case, the spectrum measured in Ar appears at a higher absorption intensity than the spectra for air and molecular oxygen.

### 5.3.2.3 Excitation in the presence of hole scavengers

In this section, bare NaTaO<sub>3</sub> powders were investigated in presence of hole scavengers (methanol). The same experimental procedure was followed as in the case of illumination with UV (C) light (see section 5.3.1.3). The powders were introduced in the cuvette and the system was purged with argon prior to the measurements. Different methanol amounts were introduced in the cuvette using a syringe. Each curve was taken with a freshly prepared sample.

Fig. 5.34 illustrates the transient absorption signals for bare NaTaO<sub>3</sub> in argon at 450, 690 and 890 nm after the addition of different amounts of methanol. The introduction of methanol to the system translates in slower signal decays (longer lifetime of the photogenerated charge carriers, see Table 5.15) for the three measured wavelengths. In all cases, the signal after the addition of 20 µl of methanol presents the lowest absorption intensity, and the signal after the addition of 100 µl of methanol the highest (higher than the material without methanol).

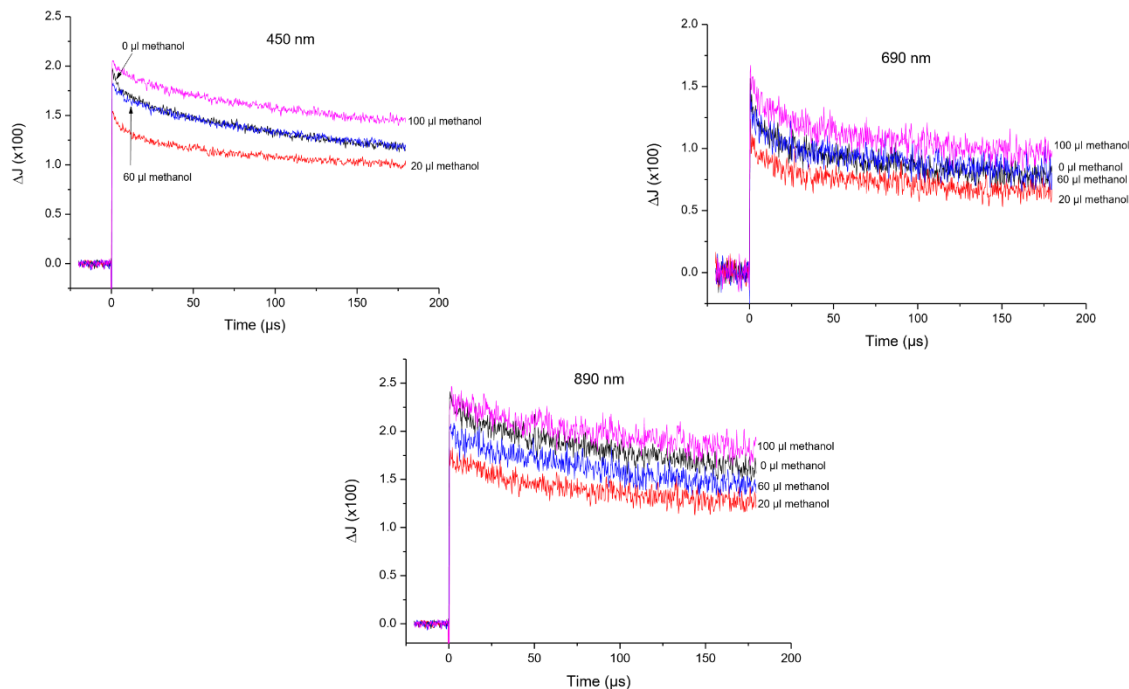


**Figure 5.34:** Transient absorption signals of bare NaTaO<sub>3</sub> measured in argon, at (a) 450 nm, (b) 690 nm and (c) 890 nm. No methanol (black), 20  $\mu\text{l}$  methanol (red), 60  $\mu\text{l}$  methanol (blue), 100  $\mu\text{l}$  methanol (pink).

The Table 5.15 summarizes the calculated lifetime of the photogenerated charge carriers before and after the methanol addition. As the results show, the addition of hole scavengers (methanol) to bare NaTaO<sub>3</sub> results in an increase in the lifetime of the photogenerated charge carriers and a slower signal decay (see Fig. 5.34). As the holes have been scavenged by the methanol molecules adsorbed at the surface of the photocatalyst, these results suggest that the observed signals might belong to photogenerated electrons. At 450 and 890 nm the addition of methanol increases drastically the lifetime of the charge carriers ( $>179 \mu\text{s}$ ), however, the increase of the lifetime at 690 nm occurs gradually.

**Table 5.15:** Summary of  $t_{2/3}$  of the photogenerated charge carriers for bare NaTaO<sub>3</sub> in argon at 450, 690 and 890 nm with different methanol additions.

Methanol ( $\mu\text{L}$ )	$t_{2/3}$ ( $\mu\text{s}$ )		
	450 nm	690 nm	890 nm
0	$94 \pm 1$	$13 \pm 2$	$\approx 179$
20	$>179$	$15 \pm 1$	$>179$
60	$>179$	$25 \pm 1$	$>179$
100	$>179$	$40 \pm 1$	$>179$

Fig. 5.35 shows the transient absorption spectra of bare NaTaO<sub>3</sub> in argon after addition of different methanol amounts.

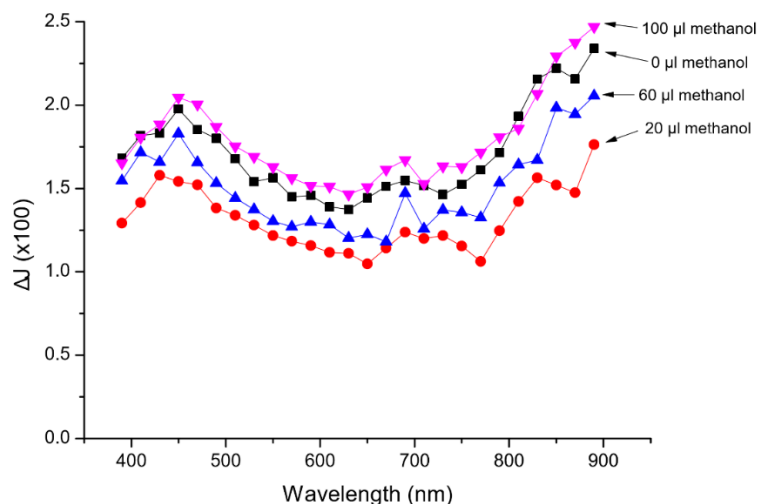


**Figure 5.35:** Transient absorption spectra 20  $\mu$ s after laser irradiation of bare NaTaO<sub>3</sub> in argon after addition of different methanol amounts. No methanol (black), 20  $\mu$ l methanol (red), 60  $\mu$ l methanol (blue), 100  $\mu$ l methanol (pink).

There are no big differences between the plotted spectra. The trend is very similar with and without methanol addition. The only observed change is in the absorption intensity. When only small amounts of methanol were added to the cuvette (20 and 60  $\mu$ l) the absorption intensity was slightly lower than for the material without any methanol. However, after adding 100  $\mu$ l of methanol the absorption intensity increase lightly above the material without hole scavenger.



## 6. Discussion

In this chapter, the results of the experimental section will be discussed and interpreted in detail. The first part deals with the optical and morphological properties of sodium tantalate materials. Next, the laser flash photolysis measurements using both excitation wavelengths (248 and 351 nm) with and without sacrificial reagents are discussed.

Previous work from Ivanova<sup>18</sup> already deals with sodium tantalates, and this thesis complements the results presented in said work. The optical and morphological properties presented next, correlates very good with Ivanova's thesis. However, in this work a deeper study has been made using laser flash photolysis.

### 6.1 Optical and morphological properties

#### 6.1.1 Band gap energy determination

For photocatalysts materials, band gap energy determination is a crucial step to understand the potential of a specific semiconductor. Using the method described in the section 4.4 it is not possible to distinguish between direct and indirect electron transitions of a semiconductor. Assuming that the scattering coefficient is constant throughout the entire wavelength range of measurement, the Kubelka-Munk equation<sup>119</sup> eq. (6.1) is usually employed instead of the absorption coefficient  $\alpha$ .

$$F(R) = \frac{(1 - R)^2}{2R} = \frac{k}{S} \quad 6.1$$

where  $R$  is the absolute reflectance of the sample,  $k$  is the molar absorption coefficient and  $S$  is the scattering coefficient. A modified Kubelka-Munk function can be obtained by multiplying the  $F(R)$  function by  $h\nu$ , using the corresponding coefficient ( $n$ ) associated with an electronic transition as follows:

$$(F(R) \cdot h\nu)^n \quad 6.2$$

By plotting this equation *vs.* the energy in eV, the band gap energy ( $E_g$ ) of the semiconductor can be obtained. For the  $E_g$  calculation, the considered type of transition is indicated with  $n=2$  for an indirect allowed transition,  $n=3$  for an indirect forbidden transition,  $n= 1/2$  for a direct allowed transition and  $n=3/2$  for a direct forbidden transition. In this work, the Tauc method was used for band gap evaluation<sup>33</sup>, where  $(F(R)h\nu)^{1/2}$  *vs.*  $h\nu$  is used for indirect electronic transitions and  $(F(R)h\nu)^2$  *vs.*  $h\nu$  is used for direct electronic transitions. In Fig. 6.1 the modified Kubelka-Munk function for allowed direct and indirect transitions versus the absorbed light energy is shown. Two straight lines can be drawn until the intercept with the abscissa. It can be seen, that the band gap slightly changes for direct and indirect electronic transitions (4.15 and 4.03 eV respectively). It is often unclear which transition mode should be preferred for a given semiconductor. According to the work by W. H. Lin<sup>120</sup> the materials present different crystal structures and band gaps depending on the synthetic mode. The materials in this

work were synthesized using a solid-state method which according to Lin's work responds to a direct transition mode. It has to be noted though, that the estimated band gap values are quite close to one another making the differentiation between the two types of electronic transitions difficult.

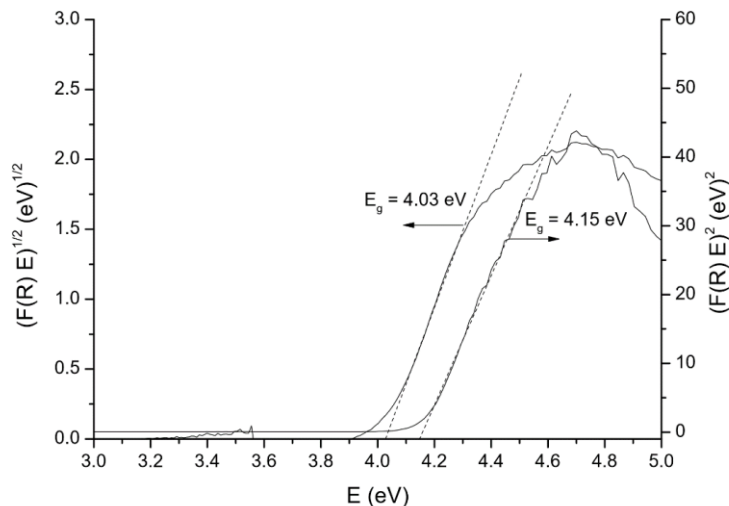


**Figure 6.1:** Modified Kubelka-Munk function *vs.* the energy of the absorbed light for the allowed direct and indirect transitions of bare NaTaO<sub>3</sub> (see Fig. 4.5).

Kanhere<sup>121</sup> reported for pristine NaTaO<sub>3</sub> that was synthesized by a solid state method, a band gap of 4.01 eV. Kudo *et al.* reported band gaps of 4.0 and 4.07 eV for bare and lanthanum doped NaTaO<sub>3</sub> powders, respectively<sup>25,26</sup>. Similar to the results obtained in this work, no significant change in the absorption of NaTaO<sub>3</sub> after lanthanum doping could be observed either.

### 6.1.2 Effect of lanthanum doping

The modification of the optical properties of a photocatalyst with an inclusion of rare earth elements often leads to an increase in the photocatalytic activity. For tantalate semiconductors, NaTaO<sub>3</sub> doped with lanthanum has been suggested to be a very promising photocatalyst for hydrogen production through water splitting<sup>25,104</sup>. The reported band gap type and optical properties of sodium tantalates differ depending on its modification, space group and synthetic route<sup>120,122</sup>. The materials used in this work were synthesized using a solid-state method and according to the literature data the sol-gel synthesis of NaTaO<sub>3</sub> provides mostly a cubic structure with band gap energy of 4.1 eV, while the solid-state route delivers an orthorhombic crystal structure with a slightly narrower band gap of 4.0 eV<sup>120</sup>. The work of Ivanova<sup>18</sup> showed X-ray diffraction (XRD) measurements for bare and La-doped NaTaO<sub>3</sub> that confirm the orthorhombic structure. Therefore, an orthorhombic structure has been assumed for the materials investigated in this thesis.

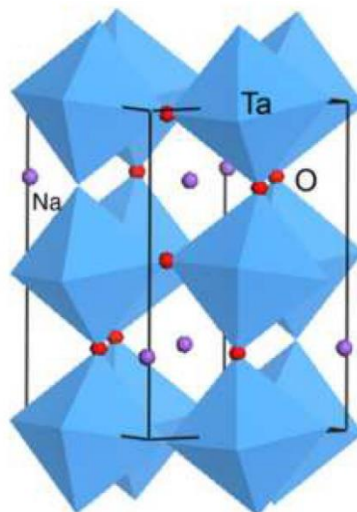


**Figure 6.2:** Crystal structure model for orthorhombic  $\text{NaTaO}_3$  <sup>123</sup>.

In the orthorhombic crystal structure, the top of the valence band consists of mainly O 2p orbitals and the conduction band consists mainly of Ta 5d orbitals. Fig. 6.2 illustrates a model of the orthorhombic crystal structure of  $\text{NaTaO}_3$ . The A site from a perovskite-type ( $\text{ABO}_3$ ) is occupied by Na and the B site hosts the Ta. The diffuse reflectance measurements performed for bare and lanthanum doped  $\text{NaTaO}_3$  (see Fig. 4.5), revealed that no changes in the band gap of the powders could be observed after doping. In order to know which positions are substituted after La doping (Na or Ta) the ionic radii of three occupied sites for La-doped material and an undoped sample should be compared <sup>124</sup>. It has been reported by Shannon *et al.* <sup>125</sup> that the ionic radii of the 12-coordinated La(III) and the Na(I) ions are almost equivalent. On the other side, the ionic radius of a 6-coordinated La(III) is larger than that of the Ta(V) ion. Therefore, the Na(I) sites will be occupied by La(III). The contribution of the Na atoms to the bands of Ta 5d and O 2p is very small because of the large distance from Na to Ta and O atoms, therefore, the lanthanum doping does not have a significant effect on the optical properties of the sodium tantalate materials, with the band gap before and after doping remaining the same (4.0 eV) as shown in Fig. 6.1.

The scanning electron microscopy (SEM) measurements performed for bare and La-doped  $\text{NaTaO}_3$  (see Fig. 4.1) showed that lanthanum doping led to a decrease in the particle size and at the same time an increase in the inhomogeneity and irregularities of the system. In fact, the measurements of the specific surface area (BET) (see Table 4.1) exhibited that La-doped materials showed a marked increase in the surface area (from 2.7 to 5.4  $\text{m}^2/\text{g}$ ).

Similar observations can be found in the literature where the particle size of  $\text{NaTaO}_3$  was found to decrease upon lanthanum doping <sup>26,44</sup>. Additionally, this thesis reports that the morphology of  $\text{NaTaO}_3$  depends strongly on the amount of lanthanum doped. It was observed that up to 0.83 wt.% of lanthanum, the inhomogeneity and irregularities of the particles increased drastically. Higher lanthanum doping with 1.11 wt.% La reduced both

inhomogeneity and irregularities and some rectangular shaped particles could be observed again (see Fig. 4.1).

The Raman spectroscopy analysis performed in this work (see Fig. 4.3) shows as well, the loss of homogeneity and the increase in irregularities provoked by lanthanum doping. As shown in Fig. 4.3 the observed Raman bands for the undoped NaTaO<sub>3</sub> decrease in intensity and shape with increasing lanthanum doping amount, which reflects the loss of shape and irregularities in the La-doped samples.

## 6.2 Energetic position of conduction and valence band

For an effective performance of the photoelectrochemical cell, the porous surface of the photocatalyst electrode is very important. Usually a doctor-blade technique is used to fabricate such porous films by coating a water-medium photocatalyst solution onto a transparent conductive glass. In this work however, a screen-printing technique is used, due to the fact that the particle size is rather large (see Fig. 4.1) and the water-medium solution of the semiconductor presented some stability problems. The screen-printing method allows the control of the film thickness and it is interesting for large scale production as well. One of the key points in this method is the paste quality which will lead to more homogeneous and stable coatings. Grätzel and coworkers have reported a procedure to produce TiO<sub>2</sub> pastes with  $\alpha$ -terpineol from commercially available powders<sup>126</sup>.

The semiconductor/electrolyte interface has been frequently treated as a Schottky barrier like the one produced at the union between a semiconductor and a metal<sup>35,127</sup> (see Fig. 2.4). As with metals, the Helmholtz layer is developed by adsorption of ions or molecules on the semiconductor surface by oriented dipoles or in the case of oxides, by the formation of surface bonds between the solid surface and species in solution. Band-edge placement can be done through differential capacitance measurements on the semiconductor/electrolyte interface.

According to eq. 2.4 the intercept of  $1/C^2$  with the voltage axis yields a straight line intersecting the potential axis at the  $E_{FB}$  as shown in Fig. 4.8. The respective donor density can be calculated from the slope of this line if all other parameters are known. For NaTaO<sub>3</sub> the permittivity has not been reported to this date, however, an approximately donor density has been calculated in section 4.5 (see Table 4.2). Non-linear Mott-Schottky plots for TiO<sub>2</sub>/electrolyte junctions have been reported frequently and the same can be said for NaTaO<sub>3</sub>. This non-linearity can be attributed to inhomogeneous donor distributions in the depletion layer or to surface roughness effects<sup>116</sup>. Surface states on a semiconductor surface can change the potential of the Helmholtz layer, thereby leading to non-linearity. As Fig. 4.8 shows, two different straight lines can be drawn through the data points. As two slopes can be found, the flatband potential is obtained by extrapolation of the first linear region at more negative potentials<sup>128</sup>. It has to be noted that eq. 2.4 assumes that  $C_{SC} < C_H$  where  $C_H$  is the Helmholtz layer capacitance. A strong dispersion of data has been obtained



with different frequencies. Similar results have been reported for  $\text{TiO}_2$ <sup>115</sup>. In this case, the Mott-Schottky plots are found to converge to a common point on the potential axis, allowing the determination of a common flatband potential.

Fig. 4.9 shows the effect of the lanthanum doping on the flatband potential determination. Taking the first linear region at more negative potentials and with increasing lanthanum doping up to 0.83 wt.%, the flatband potential shifts to more negative values. Increasing the doping to higher lanthanum concentrations translates in a back shift of the flatband potential to more positive values. The determined flatband potentials are resumed in Table 4.2. It is well established that the open-circuit potential ( $V_{OC}$ ) increment is closely correlated with the shift of the flatband potential and the Fermi level<sup>129</sup>. From the Mott-Schottky plots evaluated in the material characterization section, it is clear that the flatband edge shows an evident negative shift with increasing lanthanum concentration. This negative shift of the flatband position can be attributed to a shift in the position of the conduction band edge of  $\text{NaTaO}_3$  to more negative potentials due to La doping. As it was evaluated in the optical and morphological section of the discussion, an increase in the band gap could not be observed when lanthanum was doped. Thus an upward movement of the conduction band edge would have to be accompanied by an upward shift in the valence band edge as well. Similar results have been reported for  $\text{TiO}_2$ <sup>130</sup>. A schematic representation of the energy levels for bare and lanthanum doped  $\text{NaTaO}_3$  estimated from the flatband potential and band gap energy is presented in Fig. 6.3.

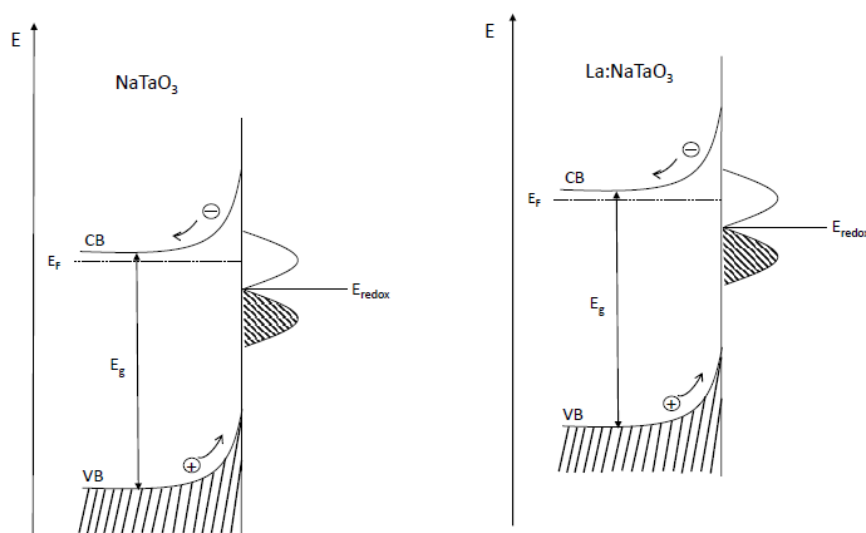


**Figure 6.3:** Schematic energy level diagrams for bare and lanthanum doped  $\text{NaTaO}_3$ .

Fig. 4.9 shows evidence of the conduction band shift with increasing lanthanum doping amount. Based on the results compiled in Table 4.2, a comparison of the band edge positions for all investigated materials can be found in Fig. 6.4 This figure shows that the material with 0.83 wt.% of La exhibits the most negative conduction band position and

therefore would be the most suitable of all studied semiconductors for water splitting as it was evidenced in the work of Ivanova<sup>18</sup>.

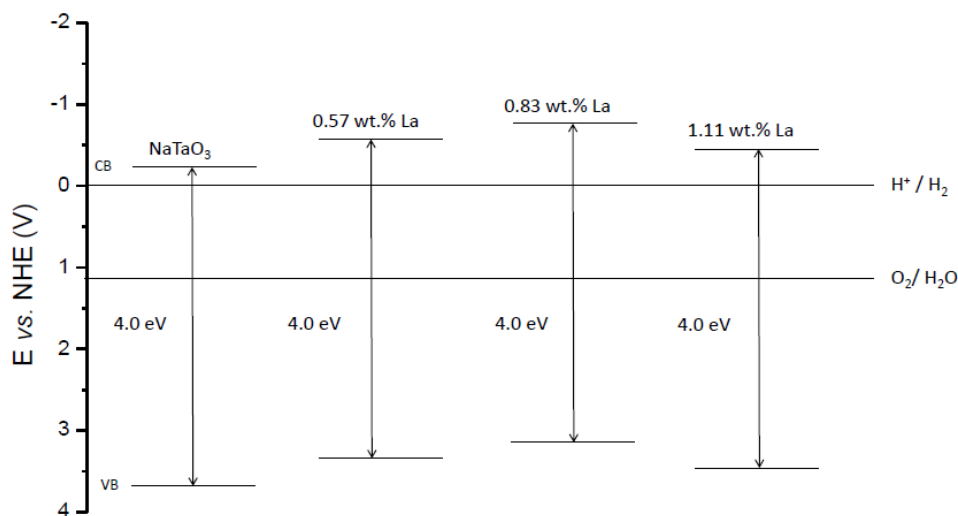


**Figure 6.4:** Positions of the conduction and valence bands for bare and La-doped NaTaO<sub>3</sub> materials.

As Fig. 1.1 showed, the theoretical minimum of the photon energy thermodynamically required to split water into hydrogen and oxygen is 1.23 eV, corresponding to a wavelength of ca. 1000 nm. This leads to the conclusion that theoretically, the entire visible spectral range can be used to achieve water splitting. However, it is important to consider the thermodynamic and kinetic energy losses in photochemical systems, which affect the band gap energy of the semiconductor. The thermodynamic energy losses have been estimated to be 0.4 eV<sup>131</sup>. The kinetic losses associated mostly with bulk and interfacial charge carrier transport, *i.e.*, with non-radiative recombination, interfacial kinetics (overpotentials), and band bending in the semiconducting materials have also been estimated to be at least 0.4 eV<sup>132,133</sup>. Therefore, the total contribution to the energy losses can be estimated to be around 0.8 eV, which increases the minimum band gap energy from 1.23 to 2.03 eV.

### 6.3 Photocatalytic H<sub>2</sub> formation

In section 4.6 the overall quantum yield of the molecular hydrogen formation for undoped NaTaO<sub>3</sub> has been determined. This helps to achieve a quantitative evaluation of the photocatalytic H<sub>2</sub> formation. The work of Ivanova<sup>18</sup> presents the quantum yield results of NaTaO<sub>3</sub> doped with 0.83 wt.% of lanthanum when it was irradiated with a wavelength range from 250 to 450 nm. In this work, only light of 350 nm was used to illuminate the sample.

The determined quantum yield of the undoped sodium tantalate is 0.97% (2.8 μmol/h) which is lower than the quantum yield determined by Ivanova (14% with 47 μmol/h)<sup>18</sup>. These results are expected as the material absorbs little light at 350 nm (see Fig. 4.5). Kato *et al.* reported a significantly higher apparent quantum yield of 56% for the La-doped

NaTaO<sub>3</sub> modified with NiO, however this group did not determine any overall quantum yield<sup>25</sup>.

The main differences between the particles investigated in this work and the particles synthesized by Kato *et al.* are the particle size and the surface structure. The La-doped particles investigated in this work and in the work of Ivanova have significantly smaller particle sizes (100-250 nm, see section 4.1) as compared to those synthesized by Kato *et al.* (100-700 nm)<sup>25</sup>. It is usually assumed that larger particles can absorb more photons creating more charge carriers and hence increasing the recombination rate, lowering the photocatalytic activity. However, the surface of the NaTaO<sub>3</sub> undoped and La-doped is flat (see Fig. 4.1) while that of the La-doped NaTaO<sub>3</sub> particles synthesized by Kato *et al.* exhibits ordered nanostep structure. The authors claim that owing to such a characteristic nanostep structure created at the surface of the La-doped NaTaO<sub>3</sub> crystal, the reactions sites can be effectively separated with the edges acting as reduction sites (H<sub>2</sub> evolution) and the grooves as oxidation sites (O<sub>2</sub> evolution)<sup>25</sup>.

#### 6.4 Electron paramagnetic resonance

Fig. 5.2 shows a sharp peak at  $g = 2.001$  and its reciprocal at  $g = 1.998$ , which are very close to the free electron value of  $g_e = 2.0023$  and suggest that the signal belongs to electrons with a low nuclear contribution<sup>117</sup>. Therefore, the signal at 310 nm measured with the laser flash photolysis technique (see Fig. 5.6 and Fig. 5.9) arises most likely from excited electrons near the conduction band. Electrons in the conduction band are usually not paramagnetic, due to the freedom of movement that the electron possess in the conduction band caused by the multitude of energy levels that lie close to each other<sup>117</sup>.

In titanates, trapped electron signals are often observed at titanium sites according to eq. 6.3. A similar reaction presented in eq. 6.4 is theoretically possible in tantalates, as the electronic configuration of Ta<sup>IV</sup> is d<sup>1</sup>, which is indeed a paramagnetic species. To date, no direct evidence of the existence of Ta<sup>IV</sup> species has been reported, and this work shows for the first time some evidence of the presence of such species in a reaction mechanism (see eq. 6.4 and 6.10). However, due to the nuclear spin ( $I = 7/2$ , see table 5.1) of the most abundant tantalum isotope <sup>181</sup>Ta, the hyperfine splitting of such species would have 8 components to it, and the observed sharp signal has only one spin up and one spin down contribution. Due to the sharp nature of the signal, which does not seem to have anisotropic contributions, the trapped electrons cannot be localized and because the signal disappears instantly in the dark, it cannot belong to deeply trapped electrons. Thus, the signal could be generated by shallowly trapped electrons, which can be hopping between nearby sites, giving rise to the anisotropy of the signal.



The higher field signal observed as a broad bump at approximately  $g = 2.011$  (see Fig. 5.2), was identified as a trapped hole signal, which is expected to be generated similarly to other oxide semiconductors as shown in eq. 6.5. As the valence band of NaTaO<sub>3</sub> is formed primarily by the O 2p orbitals, any signal associated with the holes on the valence band is expected to appear at a lower field, at least at  $g > 2.0$ . This is because an electron on a more than half-filled p orbital resonates at a lower field than a free electron, *i.e.* its  $g$  value is greater than that of a free electron. The signal also coincides well with the previously reported trapped hole signals in oxide semiconductors, where trapped hole signals of O<sup>•</sup> have been reported at  $g_{\perp} = 2.012$  and  $g = 2.005$ <sup>134-137</sup>.

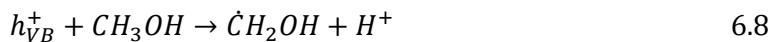


As the signal is fully reversible, and as the timescale of recombination or separation of charges are faster than which an EPR is capable of measuring, it can be concluded that in vacuum, the charges recombine perfectly and on a very fast timescale. Therefore, no photocorrosion or deep charge traps could be observed. It is worth mentioning, however, that if the data would be integrated to compare the relative areas of hole and electron signals, it would be clear that the signal of the trapped holes is greater than that of trapped electrons in area. This most likely due to promotion of some electrons to the conduction band, thus making them silent.

Fig. 5.3 showed the effect of O<sub>2</sub> on the EPR signals of the undoped NaTaO<sub>3</sub>. Yamakata *et al.*<sup>106</sup> explained the strong impact of molecular oxygen onto the rate of the electron signal decay observed with laser flash photolysis at 2000 cm<sup>-1</sup>, by oxygen acting as an electron scavenger forming a superoxide. Superoxide, O<sub>2</sub><sup>-•</sup> is a well known species, that has been recorded extensively over other semiconductor photocatalysts, such as titanium dioxide. It is a rhombic species, and as such has three signal components, which in previous literature have been reported to appear at  $g_{zz} = 2.025$  or 2.018,  $g_{yy} = 2.009$  or 2.010 and  $g_{xx} = 2.003$ <sup>24,136,138</sup>. These values correlate well with the observed values of  $g_{zz} = 2.020$ ,  $g_{yy} = 2.010$  and  $g_{xx} = 2.005$ . In general, the superoxide is formed according to eq. 6.6 and recombine according to eq. 6.7. Thus it is easy to understand, that for a superoxide to form, excited electrons are required. However, as the superoxide signal disappears upon irradiation, the electrons are not scavenged effectively from the conduction band, but only upon them falling from the higher energy levels.



Fig. 5.4 shows the effect of the methanol addition on the EPR signals of undoped NaTaO<sub>3</sub>. The small isotropic signal centered at 325 mT, which was observed in the dark after irradiation, was induced by the presence of methanol. A possible explanation for the formation of this signal is the hole scavenging. This could occur via the eq. 6.8. Methanol has been found to increase the hydrogen production rate of NaTaO<sub>3</sub><sup>18</sup>, and hence this reaction is plausible.



Rabani *et al.*<sup>139</sup> observed the effect of hole scavengers, including methanol, to TiO<sub>2</sub> and found that the presence of a hole scavenger competes with charge carrier separation and recombination.

Fig. 5.5 shows the results of the EPR measurements of 0.83 wt.% La doped NaTaO<sub>3</sub>. As the sample was otherwise the same as the undoped material, except for the lanthanum doping, the observed signal was assigned as a lanthanum induced signal. Because lanthanum is in the structure as La(III), a charge imbalance is expected to arise from La-doping. This could explain the appearance of a trapped charge carrier signal in the dark prior to irradiation. As the shape of the residual signal changes slightly, and its intensity decreases, after irradiation, it is also likely that the photoexcitation process that takes part during irradiation causes charge transfer to the observed trapped charge carrier signal. The sample was also studied in the presence of 20 mbar of molecular oxygen, but besides of the appearance of sharp physisorbed oxygen peaks, the added oxygen had no observable effect to the sample. Most notably, no formation of superoxide was observed. This suggests that La-doping somehow prevents electron scavenging by molecular oxygen.

## 6.5 Laser Flash Photolysis

### 6.5.1 Band gap excitation with UV(C) light

#### 6.5.1.1 No sacrificial reagents

The photocatalytic process is a consequence of the interaction between the semiconductor particles activated by light irradiation and its surroundings. Electron/hole pairs are created upon light absorption and they can recombine or undergo reductive or oxidative reactions, respectively. The measurements performed without any sacrificial reagent have the objective of evaluate the behavior of the photocatalyst material when it has been activated by light absorption, and the different pathways taken by the remaining photogenerated charge carriers after the recombination reaction takes place. Next, a mechanism is proposed for the photocatalytic process of sodium tantalate, based on research employing TiO<sub>2</sub> as a photocatalyst.

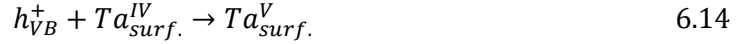
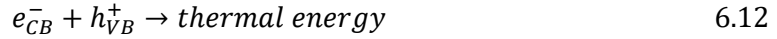
Charge carrier generation:



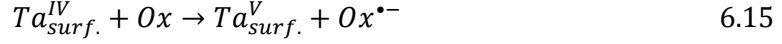
Charge carrier trapping at Ta<sup>V</sup> sites and terminal surface hydroxyl groups, respectively:



Charge carrier recombination:



Interfacial charge transfer:



where  $h\nu$  is an UV photon, Red is a reductand (electron donor) and Ox an oxidant (electron acceptor)

After the generation of charge carriers upon light irradiation, the trapping of the electrons and holes takes place. In eq. 6.9 the trapping of the electrons is proposed and based on the EPR results presented in section 5.2, the assumption has been made that the conduction band electrons could be trapped at  $Ta^{IV}$  sites in analogy to  $TiO_2$ <sup>140-142</sup> (see section 6.3 and eq. 6.4).

Eq. 6.11 corresponds to the process of the hole trapping and can be attributed to the signal measured at 310 nm (with 248 nm laser irradiation). Fig. 5.7 shows the transient absorption signals for undoped  $NaTaO_3$  in argon and vacuum. As in these cases no sacrificial reagent was added, the figure simply presents the recombination of the photogenerated electron and holes after the laser excitation. The photogenerated charge carriers present longer  $t_{1/2}$  in vacuum than in argon (see Table 5.3) which can be due to the fact that the vacuum pump is much more effective in the removal of surface oxygen than when the sample is purged with argon during 1h. In this case, the sample measured in argon still presents some molecular oxygen at the photocatalyst surface, which act as an electron scavenger. This result suggest that the signal might belong to the photogenerated electrons. However, the work of Maruyama<sup>143</sup> presents time-resolved laser flash photolysis measurements for  $NaTaO_3$  using IR light. This work claimed that the only signal visible in the IR spectrum was due to the electron accumulation, therefore it is possible that the signal belonging to holes lies in the UV region and the signal from the electrons lies in the IR region of the light spectrum. In order to further evaluate the nature of the signal at 310 nm some sacrificial reagents were added.

### 6.5.1.2 Effect of electron scavengers

#### 6.5.1.2.1 Bare $NaTaO_3$ in presence of air and molecular oxygen

As it was presented in section 5.3.1.2, a transient absorption signal at 310 nm can be observed for bare and La-doped  $NaTaO_3$  (see Fig. 5.12 and Fig. 5.14). To date only the work of Ivanova<sup>18</sup> deals with laser flash photolysis experiments on sodium tantalate using

UV light and therefore, the results in this investigation will be compared with Ivanova's work and those obtained for TiO<sub>2</sub>.

As it was shown in the work of Yamakata *et al.*<sup>106</sup>, the observed signal decay was strongly dependent of the presence of oxygen which act as an electron scavenger. For NaTaO<sub>3</sub> the presence of air and molecular oxygen in the system led to a faster signal decay than when no sacrificial reagents were present as it was shown in Fig. 5.15. The calculated half-lifetimes of the photogenerated charge carriers in presence of electron scavengers are resumed in Table 5.3 and it shows that the presence of air and molecular oxygen shortened dramatically the lifetime of the photogenerated species. This results suggest that the measured signal at 310 nm might belong to the photogenerated electrons, because of the faster decay when air and molecular oxygen were present. However, in this work measurements using Pt as electron scavenger have been performed and the nature of the signal was evaluated in more detail (see subsection 6.3.3).

#### 6.5.1.2.2 Lanthanum doped NaTaO<sub>3</sub> in air

Among the catalysts studied to date, NaTaO<sub>3</sub> doped with lanthanum has exhibited the highest quantum yield for water splitting with more than 50%<sup>25</sup>. Little is known about the charge transfer kinetics in this kind of catalysts. Although some of the knowledge accumulated for TiO<sub>2</sub> can be transferred to other catalysts, photoexcited charges should be characterized on the catalysts themselves. Therefore, in this section, some explanations are proposed for the behavior of the lanthanum doped NaTaO<sub>3</sub> powders.

Particle size is an important parameter for catalysis in general since it directly impacts the specific surface area of the photocatalyst. With a small particle size, the number of active surface sites increases, and therefore increases also the surface charge carrier transfer rate<sup>44</sup>. However, the photocatalytic efficiency does not directly increase with decreasing particle size and it is assumed that exists an optimal particle size for each semiconductor. To increase the quantum yield of nanocrystalline photocatalysts, the electron hole recombination rate has to be reduced. An effective method for the separation of electrons and holes is to introduce defects in the lattice of the material through selective metal doping. Machida *et al.* studied the photocatalytic properties of tantalates containing lanthanoid metal ions<sup>144-148</sup>. Because lanthanoid metal ions have unique properties that can modulate the band structure, surface morphology and other properties, tantalates containing lanthanoids present an interesting photocatalytic behavior. However, only the La derivative was found to be active for overall water splitting.

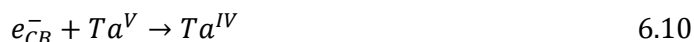
As shown in section 5.3.1.2.2, doping different amounts of lanthanum leads to different behavior of the photogenerated charge carriers. Fig. 5.13 shows that the absorption intensity for the signal at 310 nm is affected by the doping amount, as well as the signal decay. Doping with too little (0.57 wt.% La) or too much (1.11 wt.% La) lanthanum has the effect of decreasing the transient absorption intensity and increasing the signal decay when compared to undoped NaTaO<sub>3</sub>. At the same time, a shortened half-lifetime of the

photogenerated charge carriers is obtained (see table 5.2). Doping with 0.83 wt.% of La has the contrary effect. The absorption intensity of the signal at 310 nm became the highest of all investigated materials including the undoped one. The kinetic decay slowed down leading to a longer half-lifetime of the photogenerated charge carriers.

The work of Zhang <sup>149</sup> already shows that for TiO<sub>2</sub> particles there is an optimal particle size for reaching the maximum photocatalytic efficiency and that an optimal dopant concentration exists. The same postulate can be extrapolated for the sodium tantalate materials. Of the three studied doping amounts, one is more efficient in the charge separation than the others. As it has been mentioned, it is accepted that doping tantalates with lanthanum increases their photocatalytic efficiency, but in the doping concentrations studied in this work the lifetime does not increase linearly with increasing doping amount.

The material with 0.57 wt.% La-doping presents a shorter half-lifetime of the photogenerated charge carriers with respect to the undoped material (see Table 5.2). This may be due to a decrease on the particle size with the doping (increase in the surface area as showed the BET measurements in Table 4.1) and as was exposed earlier, the charges may reach the photocatalyst surface very fast leading to a very poor charge carrier separation and therefore faster electron/hole recombination.

The case of doping with 0.83 wt.% of La, the recombination reaction may be hindered and the half-lifetime of the photogenerated charge carriers is longer (see Table 5.2) due to the fact that lanthanum can act as an electron scavenger (see eq. 6.10). This suggest that the observed signal at 310 nm belongs to the photogenerated holes as opposed to the results discussed earlier.



The reaction mechanism proposed above is plausible, due to the fact that in this work the possible evidence of the existence of Ta<sup>IV</sup> species has been presented (see section 5.2).

The material doped with 1.11 wt.% of La exhibits a shorter half-lifetime of the photogenerated charge carriers (see Table 5.2) that may be due to too high lanthanum doping. This may lead to a multiple trap of the photogenerated electrons. The electrons may be trapped more than once on their way to the surface and it will likely recombine with holes before they can reach the surface.

### 6.5.1.2.3 Effect of Pt photodeposition

Noble metal coating is one of the most effective strategies to improve the efficiency of photocatalysts. It has been widely reported that surface deposition of Pt, Au, Ag and Pd on TiO<sub>2</sub> can significantly enhance its photocatalytic activity <sup>150</sup>. Although the mechanism it is still not completely understood, it is widely agreed that noble metal particles on the



TiO<sub>2</sub> surface can act as electron scavengers, thereby facilitating charge separation and reducing the charge carrier recombination rate<sup>49</sup>. It is known that noble metals exhibit higher values for the work function than metal oxides and therefore the Schottky barrier height is also higher<sup>43</sup>. This can serve as an efficient barrier, preventing the undesired electron migration back to the semiconductor (see Fig. 2.5).

While the electrons are trapped by the noble metal, the holes remain at the valence band of the host catalyst and migrate to the surface ensuring an efficient charge separation<sup>43</sup>. The work of Anpo<sup>86</sup> showed the electron transfer process from TiO<sub>2</sub> to the Pt particles using electron spin resonance (ESR) measurements. In this thesis, 0.1 wt.% of Pt was photodeposited on the NaTaO<sub>3</sub> surface in order to evaluate the behavior of the observed signal at 310 nm when an electron scavenger different from O<sub>2</sub> was present. As Fig. 5.17 shows, the photodeposition of Pt on bare NaTaO<sub>3</sub> slightly decreases the absorption intensity of the measured signal. Simultaneously, a faster signal decay is observed. The half-lifetime of the photogenerated charge carriers have been summarized in Table 5.4, showing longer lifetime of the charge carriers when platinum was present than for bare NaTaO<sub>3</sub> suggesting that the signal at 310 nm belongs to the photogenerated holes.

The work of Maruyama<sup>143</sup> shows that the signal belonging to the trapped electrons in sodium tantalate appears in the IR region of the light spectrum<sup>143</sup> and therefore it is possible that the observed signal at 310 nm belongs to the photogenerated holes. The absence of other signals might be due to the fact that the signal belonging to the photogenerated electrons lies out of the detection range of the used experimental setup.

In section 5.3.1.2.4 are shown the measurements with Pt which were performed in air, and therefore, the competition between the electron reaction with oxygen and the trapping by the Pt particles must be addressed. The presence of Pt on the surface of the photocatalyst leads to an increase of the Schottky barrier, suppressing the recombination process according to these reactions<sup>151</sup>:



The proposed mechanism for bare sodium tantalate with Pt photodeposition is illustrated in Fig. 6.5. For the materials with lanthanum doping the interpretation is different. As it has been shown in Table 5.4, the material doped with 0.57 wt.% of lanthanum (without Pt) exhibited a shorter half lifetime for the photogenerated charge carriers (see Table 5.4) than the bare NaTaO<sub>3</sub>. The decrease on the particle size due to lanthanum doping (increase in the surface area, see Table 4.1) leads to a poor charge separation, due to the fact that the charges reach the photocatalyst surface very fast, hence a faster electron/hole recombination occurs. The fact that the lanthanum can act as an electron scavenger does not seem to have a stronger impact than the particle size in this case. The photodeposition

of Pt on the surface of this material increases the half-lifetime of the photogenerated holes by increasing the efficiency of the charge separation (see Table 5.4).

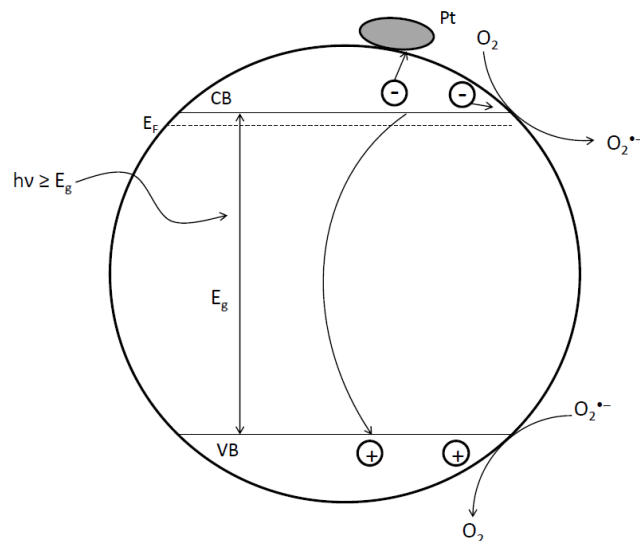


**Figure 6.5:** Proposed mechanism for electron trapping by the Pt particles in air for undoped NaTaO<sub>3</sub>.

The case of NaTaO<sub>3</sub> doped with 0.83 wt.% of lanthanum does not present the same behavior. This material showed an increase in the lifetime of the holes when only lanthanum was present (see Table 5.4), because lanthanum acts as an electron scavenger already. As it was presented in the results section, this material exhibits the slowest signal decay and longer half-lifetime of all studied materials, leading to the conclusion that the doping concentration of lanthanum was more or less optimum. The deposition of Pt however has a negative impact on the half-lifetime of the holes (see Table 5.4), suggesting a competition between the lanthanum and the Pt. The material with 1.11 wt.% of lanthanum presented a shorter half-lifetime of the photogenerated holes than with Pt because of the high lanthanum concentration that may act as a recombination center. However, the presence of Pt increased the half-lifetime of the holes suggesting a better trapping of the electrons and a more effective charge separation.

In order to evaluate whether the employed La concentration (0.83 wt. % La) corresponds to the optimal dopant concentration for NaTaO<sub>3</sub>, a newly developed theoretical model suggested by Bloh *et al.* describing the correlation between photocatalytic activity, doping ratio and particle size has been used in this work<sup>152</sup>. This model is based on the optimal doping data collected for different particle sizes of doped titanium dioxide and zinc oxide (see Fig. 6.6).

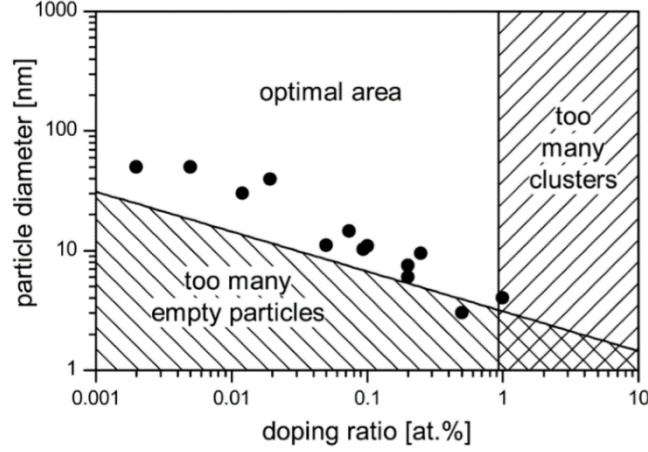


**Figure 6.6:** Optimal combinations of particle size and doping ratio, where neither too many recombination centers nor too many empty particles are present <sup>152</sup>.

It is important to emphasize, that this model is not material specific and therefore it should be applicable to any semiconductor photocatalyst considering its molar mass, density and particle size. When assuming that the optimal number of dopants per particle is  $2.40 \text{ mm}^{-1}$  of particle size, as determined by Bloh *et al.*, the optimal dopant concentration for  $\text{NaTaO}_3$  can be calculated employing the following formula <sup>152</sup>:

$$r_{d,opt} = \frac{6M}{N_A \cdot \rho \cdot \pi \cdot d^2} \times 2.40 \text{ mm}^{-1} \quad 6.22$$

with  $M$ : Molar mass of  $\text{NaTaO}_3$  (251.8 g/mol)

$N_A$ : Avogadro constant ( $6.022 \cdot 10^{23}$  mol)

$\rho$ : Density of  $\text{NaTaO}_3$  ( $7.417 \text{ g/cm}^3$ )

$\pi$ : Mathematical constant (3.14)

$d$ : Diameter of  $\text{NaTaO}_3$  particles (250 nm)

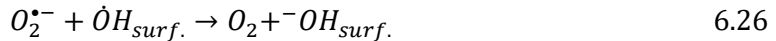
Accordingly, the calculated dopant concentration for  $\text{NaTaO}_3$  is 0.0004 at%. The lanthanum concentration employed in this work is much higher than the theoretically calculated dopant concentration.

Since the photocatalytic activity of  $\text{NaTaO}_3$  at such low dopant concentration has been not investigated yet, the existence of two optimal dopant concentrations cannot be excluded. On the one hand, this model was developed based on experimental data for  $\text{TiO}_2$  and  $\text{ZnO}$  where significantly smaller particle sizes and different crystallographic structures were considered. Therefore, this model might not be applicable for  $\text{NaTaO}_3$ . On the other hand, the doping itself might play different role for  $\text{NaTaO}_3$  materials on the one side and for

TiO<sub>2</sub> or ZnO on the other side. Consequently, completely different mechanisms might affect the photocatalytic activity of NaTaO<sub>3</sub> photocatalyst.

However, based on the results obtained from the XRD measurements presented in Ivanova's work<sup>18</sup> indicating the majority of La atoms are rather localized near the surface than in the bulk of NaTaO<sub>3</sub>, the real dopant concentration might be in this case significantly lower than 0.3 at% La (0.83 wt% La). Accordingly, it cannot be excluded that the real dopant concentration of La used in this work might indeed be very close to the theoretical value of 0.0004 at %.

The results obtained when air and molecular oxygen acted as electron scavengers suggested that the observed signal at 310 nm belonged to the photogenerated electrons whilst the results with lanthanum and Pt photodeposition led to the opposite conclusion. It is known that the photocatalytic reactions proceed mainly by the contribution of active oxygen species such as the superoxide  $O_2^{\bullet-}$ . This superoxide is formed following the next scheme in which  $e_{CB}^-$  and  $h_{VB}^+$  are the photogenerated electrons and holes and  $\dot{O}H_{surf.}$  represents the trapped holes at the photocatalyst surface.



As it can be seen from the above proposed reactions, after irradiation of bare sodium tantalate (eq. 6.9) and hole trapping (eq. 6.23), in eq. 6.24 the molecular oxygen reacts with the photogenerated electrons and a superoxide radical is formed. This superoxide radical can react with the valence band holes as well as with the trapped holes to form molecular oxygen again as seen in eq. 6.25 and eq. 6.26 respectively. The work of Fujishima<sup>153</sup>, proposes the reduction of O<sub>2</sub> to  $O_2^{\bullet-}$  when the conduction band edge of TiO<sub>2</sub> is more negative than the redox potential of superoxide radical formation. As shown in Table 4.2, the flatband potential for bare NaTaO<sub>3</sub> lies at -0.32 V and the potential for the superoxide formation is -0.284 V<sup>154</sup>, being the E<sub>CB</sub> of bare NaTaO<sub>3</sub> just slightly more negative and allowing the formation of the superoxide. In the same table (Table 4.2) the flatband potentials for the lanthanum doped powders can be also found and with increasing lanthanum concentration the flatband potential shifts to more negative values, allowing an easier oxygen reduction. The material doped with 0.83 wt.% of La, is the one with the most negative conduction band edge and therefore will react more easily with molecular oxygen.

As Fig. 5.15 shows, only one signal is observed, which means that the trapped holes will not accumulate and therefore no shift or new shoulder appears in presence of molecular oxygen. At the same time, electrons and holes are being consumed by the recombination reaction. If the observed transient absorption signal at 310 nm belongs to the holes, these

reactions explain why in presence of oxygen, the signal decay is faster and the half-lifetime of the photogenerated charge carriers becomes shorter. In Fig. 6.5 is presented the proposed mechanism for the oxygen effect in the system through the formation and reduction of a superoxide radical. Photogenerated electrons and holes are being consumed not only through the reaction with oxygen and the superoxide but also through the recombination reaction.

### 6.5.1.3 Effect of hole scavengers

It has been proven that the photocatalytic activity for H<sub>2</sub> evolution from pure water is much lower than the photocatalytic activity from aqueous alcoholic solutions<sup>18</sup>. As proposed by Tamaki *et al.* this can be explained by the much lower water oxidation efficiency by the photogenerated holes as compared with the alcohol oxidation efficiency<sup>96</sup>. The photocatalytic activity for hydrogen evolution depends on the nature of the alcohol employed in such photocatalytic reactions. Different works have shown that methanol is the most effective electron donor among other investigated alcohols for TiO<sub>2</sub><sup>155-157</sup>.

In this work the impact of the addition of different amounts of methanol to bare NaTaO<sub>3</sub> has been investigated and compared to the results of studies with TiO<sub>2</sub>. Fig. 5.19 shows how the observed transient absorption signal at 310 nm is affected by the addition of different methanol amounts. With increasing methanol concentration the signal decay becomes faster which is consistent with the results of studies performed on titanium dioxide<sup>96</sup>. This decay is slow at the beginning but after the addition of 100 µl of methanol a more dramatic change happens.

In Table 5.5 the half-lifetimes of the photogenerated charge carriers are summarized and it can be clearly seen how an increase in the methanol amount led to a decrease in the half-lifetime of the photogenerated charge carriers. With these results, the assumption that the observed signal belongs to the photogenerated holes is confirmed. The measurements with methanol were performed in argon in order to evaluate more easily the effect of the alcohol in the photogenerated charge carriers. Adding methanol as an electron donor to react irreversibly with the valence band (VB) holes can enhance the photocatalytic electron/hole separation efficiency, resulting in higher quantum efficiencies. In Fig. 6.7 the proposed mechanism for all the processes involved in the photocatalytic hydrogen evolution is presented using methanol as an electron donor.

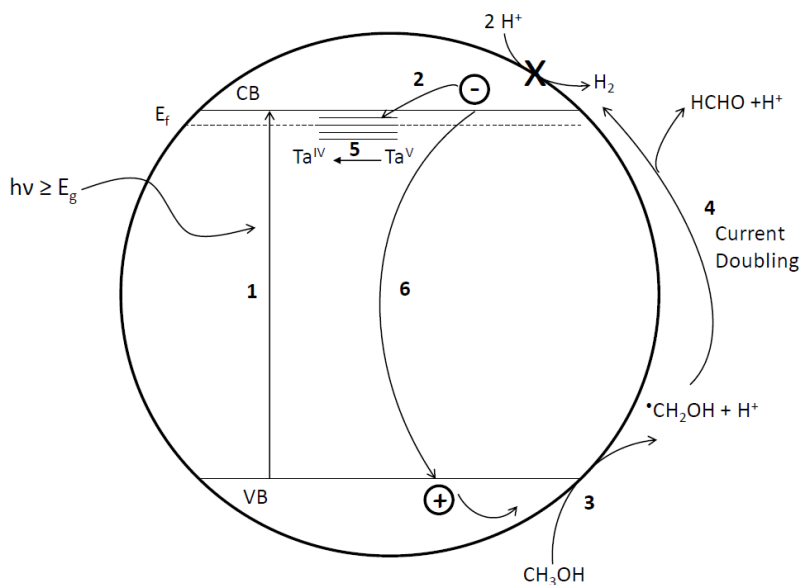


**Figure 6.7:** Proposed mechanism for hole scavenging by methanol in Ar for bare NaTaO<sub>3</sub>.

(1) Represents the photogeneration of the electron and holes, (2) trapping of the conduction band electron by Ta<sup>V</sup>, (3) first oxidation step of methanol, (4) formation of HCHO through electron injection into the conduction band of NaTaO<sub>3</sub> (current doubling), (5) formation of Ta<sup>IV</sup> and (6) recombination of the charge carriers. As it was shown in Table 5.5, the half-lifetime of the photogenerated holes decreases with increasing methanol addition. However, the process pictured in Fig. 6.7 can be applied for methanol, ethanol and 2-propanol but not for tert-butanol (2-methyl-2-propanol). In this last case, a β-hydroxy radical is formed which can neither reduce tantalates nor inject an electron into the conduction band of sodium tantalate (current doubling effect). Therefore, the only effect upon the presence of tert-butanol in the system is the inhibition of the undesired electron/hole recombination reaction.

Calculations have been made in order to evaluate the volume of tantalate molecules with respect to the volume of methanol molecules. For that purpose, the length of 1 cm of the cuvette was taken. When the photocatalyst was added, the height was 1.5 cm and the methanol was absorbed to a depth of 1 mm. Therefore, a total volume of  $1.5 \cdot 10^{20} \text{ nm}^3$  is available. The volume of a  $175 \times 175 \text{ nm}$  NaTaO<sub>3</sub> particle is calculated to be  $2.81 \cdot 10^6 \text{ nm}^3$ . For that reason, in the mentioned volume are  $5.36 \cdot 10^{13} \text{ nm}^3$  particles of NaTaO<sub>3</sub>.

Fig. 5.21 shows that the addition of other alcohols presents the same behavior than methanol. In all cases, the signal decay becomes faster with increasing alcohol amount. Moreover, in Table 5.6 are shown how the half-lifetimes of the photogenerated charge carriers decrease with the increasing alcohol amount. Fig. 6.8 represents the inverse of the half-lifetime of the photogenerated holes ( $1/t_{1/2}$ ) vs. the moles of added alcohol.

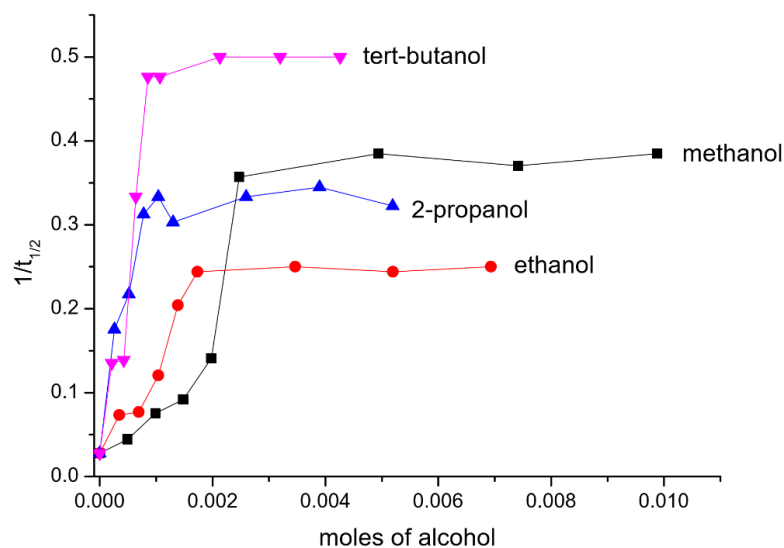


**Figure 6.8:** Reciprocal lifetime (see table 5.5 and table 5.6) of the photogenerated holes in bare  $\text{NaTaO}_3$  vs. moles of added alcohol in Ar.

It is clear from Fig. 6.8 that the nature of the alcohol plays a role in the signal decay. In all cases, an almost linear increase in the kinetic constant can be seen until a plateau is reached after a certain alcohol amount. In the case of methanol this constant region is achieved after the addition of 0.0025 moles. However, for alcohols with longer chain lengths this plateau is achieved sooner. This would imply that alcohols with longer chain lengths can act as better hole scavengers than methanol for small alcohol amounts, and that the reaction kinetics are faster as well, translating in a better charge carrier separation efficiency. As the first part of Fig. 6.8 is more or less linear,  $k_2$  could be calculated. Fig. 6.9 represents the calculated  $k_1$  versus the moles of alcohol. The first kinetic constant has been obtained using Eq. 6.27.

$$k_1 = \frac{\ln 2}{t_{1/2}} \quad 6.27$$

From the slope of the representation in Fig. 6.9, a second kinetic constant ( $k_2$ ) can be obtained, and the values are summarized in Table 6.1.

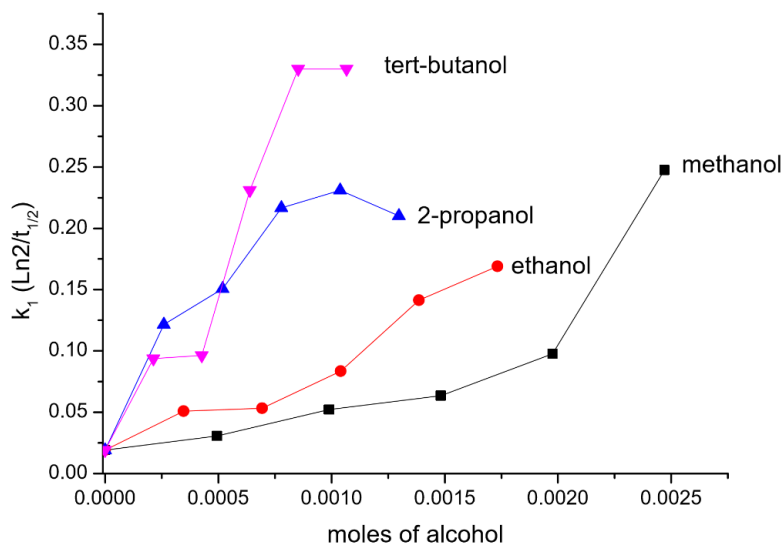


**Figure 6.9:** Representation of the calculated  $k_1$  vs. the moles of alcohol added.

**Table 6.1:** Summary of the calculated  $k_2$  for the different used alcohols. Slope extracted from the curves in Fig. 6.9.

Alcohol	$k_2$
Methanol	38.4
Ethanol	86.65
2-Propanol	199.83
Tert-Butanol	356.11

As Table 6.1 shows, the calculated kinetic constant  $k_2$  increases with longer alcohol chain-length.

Some results found in the literature for titanium dioxide<sup>96</sup> observed an opposite trend and methanol presented the shorter lifetime (fastest signal decay) of the investigated alcohols. Fig. 6.7 shows that the reactions with alcohol take place through radical formation. Therefore, the stability of these radicals plays an important role. The first step in the process of radical formation is the breaking of the C-H bond. In the case of methanol this bond is more stable<sup>158</sup> and strong than for ethanol, propanol and tert-butanol which form primary, secondary and tertiary radicals respectively and therefore, the formation of the radical is more difficult for methanol than for the other alcohols. When only small amounts of methanol are added to the system, the hole scavenging process can be slowed down due to the more difficult radical formation. After a certain amount of methanol is added (100  $\mu$ l) this effect can be compensated and the lifetime of the photogenerated charge carriers becomes shorter than for the other alcohols. The alcohols of longer chain length may reach the plateau before methanol because the effect of the repulsive forces between molecules



may be stronger due to the bigger molecule size. The work of Rabani *et al.*<sup>159</sup> observed a better reactivity of the radical formed by propanol than the methanol radical as well.

#### 6.4.1.4 Effect of electron and hole scavengers

In this work, measurements in systems where both electron and hole scavengers are present were performed as well. The samples were measured in air or after purging with molecular oxygen and methanol addition and compared with the results obtained in Ar and methanol. The competition between the processes will be evaluated next.

As it has been proposed, the transient absorption signal observed at 310 nm (see Fig.5.6) belongs to the photogenerated holes, which decay rapidly when only methanol (or other alcohol) as hole scavenger was present in the system, which suggests an effective trap of the photogenerated holes by the alcohol molecules. At the same time, the different atmospheres evaluated without alcohol addition, showed that the signal in argon presented a much longer lifetime of the holes than in air or after oxygen purging (see Table 5.3). The addition of methanol to the three atmospheres (air, oxygen and argon) has the same effect in all cases: a drastic decrease in the half-lifetime of the photogenerated holes. As it has been resumed in Table 5.7 and table 5.8, the addition of 100  $\mu$ l of methanol reduced the half-lifetime of the holes in air in a 82.76%, in molecular oxygen a 87.5% and in argon in a 92.94%. Therefore, it can be said that the photogenerated holes are effectively trapped by the methanol and the presence of electron scavengers has a very little effect on the overall mechanism. The reaction between the  $O^{\bullet-}$  with methanol is almost negligible and has not an observable effect in the process. Following the same pattern, in Fig. 5.23 are plotted the transient absorption signals after 100  $\mu$ l methanol addition in air and oxygen saturated atmosphere. The calculated lifetimes are summarized in Table 5.8. The half-lifetime of the photogenerated holes when oxygen is present in higher concentrations is shorter than in air, leading to the conclusion that the reaction of oxygen with methanol is negligible.

#### 6.5.2 Sub-band gap excitation with UV(A) light

The absorption coefficient (Fig. 4.7) and diffuse reflectance (Fig. 4.5) measurements exhibit a very low light absorption from 400 to 320 nm. The photocatalytic experiments presented in Fig. 5.1 showed that even though the absorption was very low, evolution of  $H_2$  can be detected when the photocatalyst was irradiated with light of 350 nm (see Fig. 4.5). Therefore, in the results section the measurements for laser flash photolysis with 351 nm were presented and will be discussed next.

##### 6.5.2.1 No sacrificial reagents

Laser flash photolysis measurements were carried out in argon in order to evaluate the system when no sacrificial reagent was present. The process followed for purging the cuvette of the desired gas is exactly the same as for the previous experiments.

The transient absorption spectrum of bare  $\text{NaTaO}_3$  measured in Ar shows absorption intensity in the whole range of measured wavelengths (400 to 890 nm) (see Fig. 5.24). However, three peaks can be differentiated at 450, 690 and 890 nm. These signals are very difficult to isolate because they overlap extensively. For the evaluation of these three peaks a derivative spectroscopy method can be employed. This is an analytical technique of great utility for extracting both qualitative and quantitative information from spectra composed by unresolved bands <sup>160</sup>.

The absorption spectrum of a material is the superposition of several rather wide and closely placed absorption bands. Because of this, the total spectral curve has a complex form and some points either do not manifest at all or are displayed as weakly expressed bends, inflexions, shoulders or protrusions <sup>161</sup>. Tabular values are usually satisfactory for bands which occur well apart in the spectrum and the wavelength positions can be assigned with precision. However, if two bands are not separated and mutual overlapping occurs, the characteristics of one or both tend to be obscured. The work of Vandebelt *et al.* <sup>161</sup> investigate the effects produced by the overlapping of bands in spectra, including specially the apparent changes in wavelength produced by combination of two bands. This is done by plotting symmetrical band outlines at different intervals of separation, adding the ordinates of each and observing the summation spectra obtained. The work of Giese *et al.* <sup>162</sup> proposed a method of spectroscopic measurement designated as derivative spectrophotometry. Using this method, it can be evidenced the behavior of the derivatives of hypothetical overlapping absorption bands. The spectra in Fig. 5.24 was extrapolated in order to obtain more data points to work with, and the fitting to a Gauss mathematical function was carried out <sup>161</sup>.

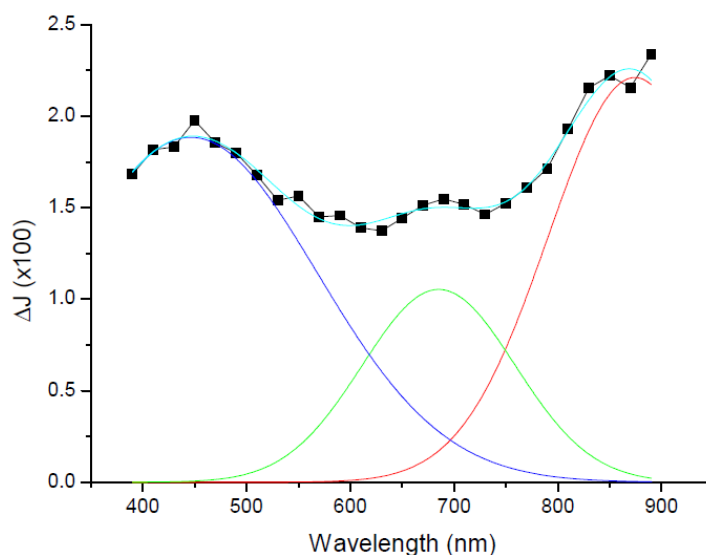


**Figure 6.10:** Fitting of the extrapolated transient absorption spectra (Fig. 5.24) for bare  $\text{NaTaO}_3$  in Ar to a Gauss function.

As shown in Fig. 6.10 there are in fact three different peaks or shoulders in the transient absorption spectrum of sodium tantalate. However, as it has already been explained, the shoulder at 690 nm is very difficult to evaluate because it overlaps with the two broader bands at 450 and 870 nm. Therefore, the assignment of this band to a determined chemical reaction or photocatalytic process is not possible with the obtained data.

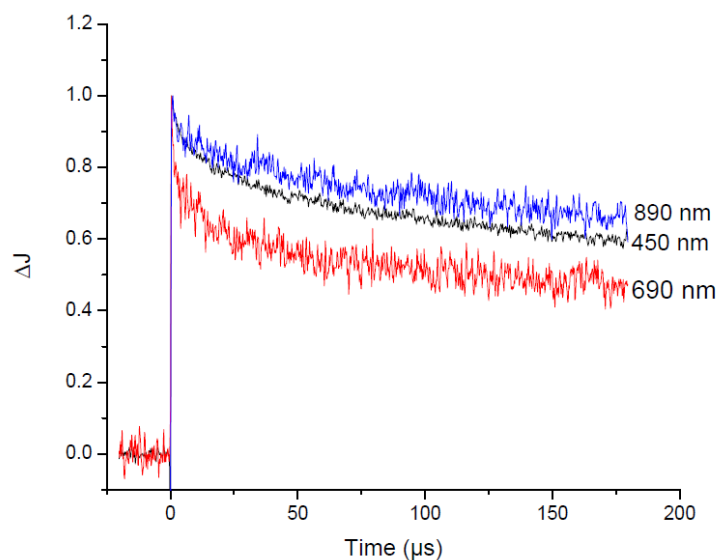


**Figure 6.11:** Normalized transient absorption signals (Fig. 5.25) for bare NaTaO<sub>3</sub> in Ar at 450, 690 and 890 nm.

Fig. 6.11 shows the normalized transient absorption signals for the bare photocatalyst at 450, 690 and 890 nm. As it can be observed, the signals present slightly different decay behavior. The signal at 690 nm exhibits a faster initial decay than the signals at 450 and 890 nm. The fact that the decays are different might be due to the fact that the overlapping peaks do not belong to the same species. If different species can be present it is acceptable that have different kinetics if they take place in different reactions.

### 6.5.2.2 Electron scavengers

As it can be observed from the results of measurements performed in presence of electron scavengers (see section 5.3.2.2), such as air, molecular oxygen purging and lanthanum doping, there is no big difference between the calculated  $t_{2/3}$  of the photogenerated charge carriers. The presence of electron scavengers does not alter the shape, height or decay if compared to the signals obtained with no scavenger. This may be an effect of the deep trapping of the electrons in the defect energy levels (explained later), where they become less reactive.

### 6.5.2.3 Hole scavengers

As Fig. 5.34 and Fig. 5.35 show, measurements using methanol as hole scavenger, in different amounts were performed. The amount of methanol has an important effect in the hole trapping process. When the sample was excited with a 248 nm wavelength, the half-

lifetime of the photogenerated holes becomes shorter with increasing methanol concentration (see Table 5.5). However, this is not the case when a 351 nm laser excitation wavelength was used. The addition of small amounts of methanol, increases slightly the  $t_{2/3}$  of the photogenerated electrons as it can be observed in Table 5.15. A very big difference can be seen after the addition of 100  $\mu$ l of methanol. In this case, the lifetime of the electrons increases drastically and the signal intensity becomes also higher (see Fig. 5.35). This can be an evidence that the signals obtained when irradiating with 351 nm belong to the photogenerated electrons, as the lifetime increases with increasing methanol addition.

#### 6.5.2.4 Electron trapping in mid-gap states

As it has already been explained in this work,  $\text{NaTaO}_3$  has a wide band gap of 4.0 eV (see Fig. 4.5). The irradiation with a wavelength of 351 nm corresponds to an energy of 3.5 eV which is lower than the band gap. According to this, the photogenerated electrons do not have enough energy to reach the conduction band of the material. However, small transient absorption signals (almost ten times smaller than for irradiation with 248 nm) have been measured throughout the spectrum in the range from 400 to 890 nm. A scheme of the proposed mechanism is illustrated in Fig. 6.12.

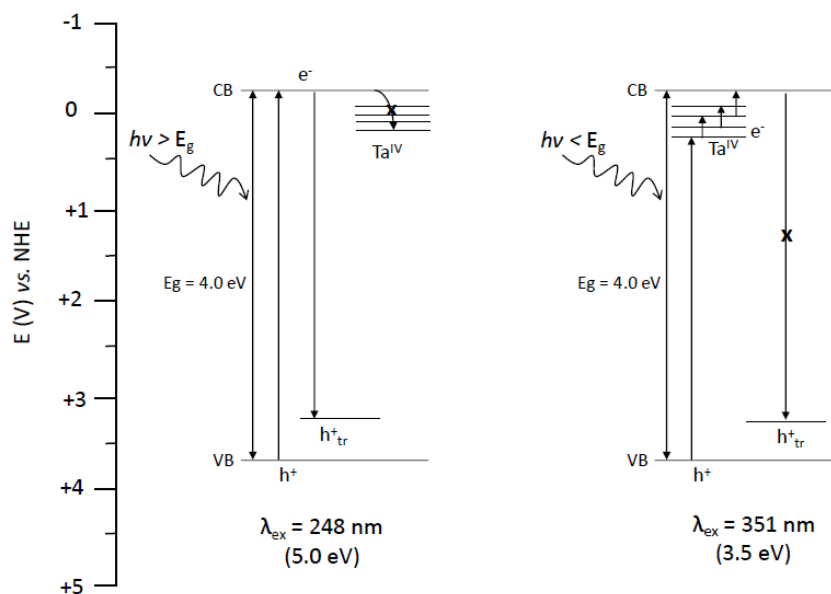


**Figure 6.12:** Scheme of the proposed process of electron trapping by surface defects.

All metal oxides present surface defects already before irradiation. For titanium dioxide, these surface defects are mainly oxygen vacancies and Ti(III) ions<sup>163</sup>. These surface defects are located in discrete energy levels within the band gap. More specifically below the conduction band as it has been reported by several studies<sup>164,165</sup>. Upon irradiation with a 248 nm wavelength (5.0 eV) the photogenerated electrons migrate to the conduction band where they can undergo reduction reactions or can recombine with the photogenerated

holes. The relaxation of the electrons in the conduction band to the defect trap states is thermodynamically not as favorable as the recombination because of their higher energy level. Therefore, by irradiation with an energy greater than the band gap only one transient absorption signal could be measured, which corresponded to the photogenerated holes.

On the other hand, when the material was irradiated with a 351 nm laser excitation wavelength (3.5 eV), the photogenerated electrons do not have the sufficient energy to reach the conduction band. These electrons can, however, be trapped in the energy levels of the surface defects, that in sodium tantalate could be Ta<sup>IV</sup> species. These species have been detected by the EPR measurements presented in this work as well (Fig. 5.2). The fact that there can be a distribution of energy levels due to defects depending on the environment, makes possible that also a distribution of transitions from the energy levels of the defects to the conduction band can be observed. Therefore, the measurements performed with 351 nm laser excitation exhibit a continuous distribution of transient absorption signals throughout the whole spectrum (see Fig. 5.24 and Fig. 5.25).

It has to be noted, that for the electrons to be trapped in the defect levels, the latter have to be empty first. This is possible if water is adsorbed on the semiconductor surface, which can never be completely excluded. The proposed mechanism is similar to the mechanism proposed by Hashimoto *et.al*<sup>166-171</sup>. They observed that when Fe(III) or Cu(II) nanoclusters are grafted onto the surface of titanium dioxide, the electrons in the valence band can be excited to these clusters via an interfacial charge transfer (IFTC) process under visible light irradiation. In this case, the transient absorption signals obtained with 351 nm excitation would belong to the photogenerated electrons. The  $t_{2/3}$  of the photogenerated charge carriers was found to be much longer than the  $t_{1/2}$  of the photogenerated holes with 248 nm (see Table 5.9). It can be said then, that the electrons are deeply trapped in the defect energy levels.

Irradiation with different laser excitation wavelengths implies different light penetration depths, and different number of irradiated particles. Calculations of these parameters have been made in order to understand better the two proposed systems. It has been determined in the work of Ivanova<sup>18</sup> the absorption coefficients ( $\theta$ ) of bare NaTaO<sub>3</sub> in solution for different wavelengths. For a 250 nm excitation wavelength,  $\alpha = 1.1922$  L/g·m and for 350 nm  $\alpha = 0.0757$  L/g·cm. In this thesis the materials were used in its powdered form, therefore the density of the material has been used to transform to an absorption coefficient in solids. The density of bare NaTaO<sub>3</sub> was determined using a sodium tantalate single crystal which was grown by the Institute of Crystal Growth located in Berlin. This single crystal was weighted and immersed in water and the determined density was found to be 7.4 g/cm<sup>3</sup>. With this information the light penetration depth of an excitation with 250 nm was found to be 1  $\mu$ m, whilst for an excitation with 350 nm is 18  $\mu$ m. Assuming particles of 175 x 175 nm the irradiated area and volume are calculated and with this, the number of irradiated particles can be determined. For 250 nm  $2.77 \cdot 10^{10}$  and for 350 nm  $4.98 \cdot 10^{11}$  irradiated particles. Calibration using ferrioxalate actinometry has been performed for both

wavelengths and for 248 nm, the pulse energy resulted in 16 mJ which lead to a very high number of photons:  $2 \cdot 10^{16}$  photons. The actinometry performed for the 351 nm excitation wavelength lead however to a lower pulse energy of 2.7 mJ which corresponds to  $4.77 \cdot 10^{15}$  generated photons.

With all the calculations above, it can be said that the systems with the two laser excitation wavelengths are very different between them. When a 248 nm irradiation is used, a very high number of photons are created that penetrate only 1  $\mu\text{m}$  into the powders. Therefore, around  $7 \cdot 10^5$  photons are used per particle. For a laser excitation wavelength of 350 nm, the number of created photons is lower but the penetration depth and the number of irradiated particles is higher than for 248 nm. Therefore, less photons per particle are used (approx.  $9 \cdot 10^3$ ). When the sample is irradiated with light of 248 nm the observed signal at 310 nm belongs to the photogenerated holes, whilst when the sample is excited with 351 nm the three observed signals at 450, 690 and 890 nm belong to the photogenerated electrons.

#### 6.5.2.5 Two-photon absorption process

Another explanation can be found for the transient absorption measurements observed with a 351 nm laser excitation wavelength, which cannot be excluded. The work of Ohtani *et al.*<sup>172</sup>, suggested that when titanium dioxide was irradiated with light-pulses of near band gap energy, an anomalous rapid decay could be observed while this was not the case of over band gap irradiation. Furube *et al.*<sup>173</sup> investigated the recombination dynamics of photogenerated charge carriers in several  $\text{TiO}_2$  photocatalytic powders and showed that the electron/hole recombination kinetics depended strongly on the crystal structure of the  $\text{TiO}_2$  powders. Ohtani<sup>172</sup> evidenced a discrepancy between the results of both works because the difference in wavelengths of the pump pulse. Furube used a 390 nm pump pulse, which corresponds roughly to the band gap of anatase  $\text{TiO}_2$  (3.2 eV) and Ohtani employed a 310 nm light with an energy much higher than the energy gap of anatase.

In this work, two different laser excitation wavelengths have been used. As it has already been established in Fig. 6.1, the band gap of  $\text{NaTaO}_3$  is 4.0 eV. The first laser excitation pump pulse used is 248 nm which has an energy of 5.0 eV (over the band gap of sodium tantalate) and the second laser excitation wavelength is 351 nm which has an energy of 3.5 eV (less than the band gap of sodium tantalate). It has to be noted that following the diffuse reflectance absorption measurements presented on Fig. 4.5 no absorption was expected when sodium tantalate was irradiated by a pump pulse with a wavelength longer than 310 nm (4.0 eV). However, appreciable absorption was observed at  $>310$  nm pumping. One of the possible reasons for this absorption is that a two photon absorption process occurs in  $\text{NaTaO}_3$ .

Two-photon absorption (TPA) is a nonresonant nonlinear process that occurs for photons with energy less than the semiconductor energy gap  $E_g$  but greater than  $E_g/2$  as it was

described by Laughton *et al.*<sup>174</sup>. For this range of photon energies, there is very little absorption of light due to the absorption of single photons.

However, when a semiconductor is irradiated by an intense beam of light, an electron can be excited from the valence band to the conduction band by the absorption of two photons. This excitation occurs via an intermediate virtual state. This virtual state can be a state in the valence band, the conduction band or some other band, although the transition probability is the highest when the energy difference between the states is the smallest, that is when the intermediate state lies closest to the upper valence band or lowest conduction band<sup>175</sup>. In Fig. 6.13 is represented a scheme of the proposed two-photon absorption process. For the measurements done under excitation with a 248 nm wavelength the  $t_{1/2}$  was calculated for the photogenerated holes. However, the excitation with a longer wavelength (351 nm) leads to the formation of longer-lived photogenerated charge carriers and therefore  $t_{2/3}$  has to be calculated. The reason for the shorter lifetime of the holes with the 248 nm wavelength can be explained by means of the number of photogenerated charge carriers.

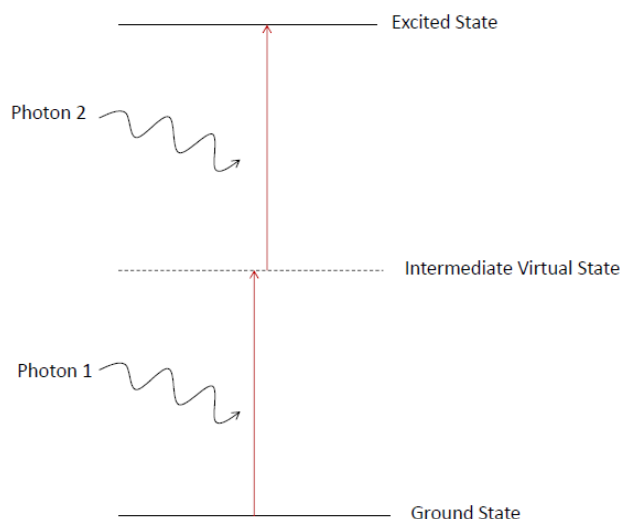


**Figure 6.13:** Scheme of the proposed two-photon absorption (TPA) process.

In order to evaluate if a two-photon absorption process is taking place, a dependency of the absorption with the laser intensity has to be observed<sup>176</sup>. At the same time, by exciting the sample with 351 nm much less photons are absorbed per particle, therefore it is unlikely that a two-photon process takes place.





## 7. Conclusions

In this work, bare and La-doped NaTaO<sub>3</sub> powders synthesized by the company H.C. Stark, using a solid state reaction have been successfully characterized using different analytic and electrochemical methods. Thanks to this characterization, the underlying mechanisms that occur upon light excitation with different wavelengths could be proposed and better understood.

With the electrochemical measurements performed in this thesis, the energetic position of the conduction and valence band of NaTaO<sub>3</sub> have been determined. Using the Mott-Schottky method it was observed that the presence of lanthanum shifts the conduction band edge to more negative potentials, reaching its maximum with the 0.83 wt.% La doping. This sample presented the most negative conduction band position of the investigated powders and as it was shown in the laser flash experiments, the longest lifetime of the photogenerated charge carriers. This work demonstrates that the signal decay and therefore photocatalytic activity using NaTaO<sub>3</sub> powders is affected to some extent by the doping of the materials with lanthanum within the synthetic process, and by the presence or absence of sacrificial reagents in the system. The use of different laser excitation wavelengths is evidenced as well.

The modification of bare NaTaO<sub>3</sub> with different amounts of lanthanum lead to different effects in the performance of the material. Among the three lanthanum dopings, *i.e.*, 0.57, 0.83 and 1.11 wt.% of La used in this work, 0.83 wt.% La reveals a longer lifetime of the photogenerated charge carriers when laser excitation was carried out with a 248 nm wavelength, which corresponds to a greater energy than the band gap of NaTaO<sub>3</sub>. Therefore, it can be said, that 0.83 wt.% La is the best dopant concentration of all three, and the separation of the photogenerated charge carriers in the depletion layer is much more effective.

The presence of electron scavengers (*i.e.* air, molecular oxygen, Pt) when irradiating the samples with 248 nm has different impacts on the signal decay of the material. Air and purging with molecular oxygen decrease the half-lifetime of the photogenerated charge carriers, which can be explained by the formation of a superoxide O<sub>2</sub><sup>•-</sup>. This radical is formed by the reaction of electrons with oxygen; which at the same time can react with photogenerated holes, therefore reducing their half-lifetime.

The effect of the photodeposition of noble metal islands has been evaluated as well in this thesis. For that purpose, 0.1 wt.% of Pt was photodeposited on NaTaO<sub>3</sub>. The addition of platinum to the undoped material drastically increases the half-lifetime of the photogenerated charge carriers, evidencing that the observed signal belongs to photogenerated holes. If lanthanum was already present in the sample, the addition of Pt has different effects. For low and high lanthanum concentrations (0.57 and 1.11 wt.% La), the half-lifetime of the holes increases as well but in a more discrete way than for the bare

material. This can be explained by an increase of the specific surface area of the material and a better charge carrier separation and due to the lanthanum character of electron scavenger with help of the Pt particle. If the optimal lanthanum concentration is already achieved, the presence of Pt on the surface does not help increase the lifetime of the holes; on the contrary, too many electron scavengers can act as recombination centers.

The presence of hole scavengers was investigated by the addition of different amounts of methanol, ethanol, 2-propanol and tert-butanol to the undoped NaTaO<sub>3</sub>. In all cases, the half-lifetime of the photogenerated holes decreases linearly with increasing methanol concentration. This leads to the conclusion that the observed signal at 310 nm obtained when the sample was irradiated with a 248 nm laser pulse, belongs to the photogenerated holes.

In this thesis, signals for photogenerated electrons were observed as well using laser flash photolysis with UV light. The measurements performed using a 248 nm laser excitation wavelength correspond to an energy of 5.0 eV which is greater than the band gap (4.0 eV) and leads to a sufficient energy for the photogenerated electrons to reach the conduction band of the material. The results obtained with this wavelength manifest, that the signal measured at 310 nm belongs to the photogenerated holes. On the other hand, measurements performed with 351 nm laser excitation wavelength, correspond to an energy of 3.5 eV which is lower than the band gap and therefore, the photogenerated electrons do not have sufficient energy to reach the conduction band. However, absorption can be measured throughout the whole spectrum. This can be explained by the surface defects present in the surface of metal oxides. These surface defects can be located in a discrete distribution of energy levels within the band gap, and more specifically below the conduction band. The photogenerated electrons have sufficient energy to reach these surface defect energy levels and get trapped. It has to be noted that the addition of electron scavengers does not exhibit any effect of the signals and that the calculated lifetime of the photogenerated charge carriers is much longer than the lifetime for the photogenerated holes. These effects evidence that the signals measured using 351 nm excitation belong to the photogenerated electrons and that those electrons are deeply trapped and become less reactive. The addition of hole scavengers does increase the lifetime of the electrons. The irradiation of a photocatalyst with a sub-band gap energy can be helpful in the future design of visible light-driven semiconductors. Introducing mid-gap states within the band gap may improve the efficiency of some of the materials with wide band gaps that may not be useful with visible light.

Within this thesis it has been demonstrated the effects of lanthanum doping in the conduction band edge and in the lifetime of photogenerated charge carriers for NaTaO<sub>3</sub>.

Fig. 7.1 shows a scheme of the main proposed processes discussed in this work. After the irradiation of the sample with UV light with an energy greater than the band gap (248 nm), electrons and holes are created. The photogenerated electrons, migrate to the conduction band where can undergo different reactions: they may react with molecular

oxygen to build a superoxide radical, or if there is a noble metal island, they may get trapped by it. At the same time, the photogenerated holes present on the valence band, may react with the molecular oxygen as well, generating more superoxide radicals, or if there is any methanol on the photocatalyst surface, the holes will oxidize the alcohol molecule and inject an electron into the conduction band to form  $\text{Ta}^{\text{IV}}$  (current doubling).

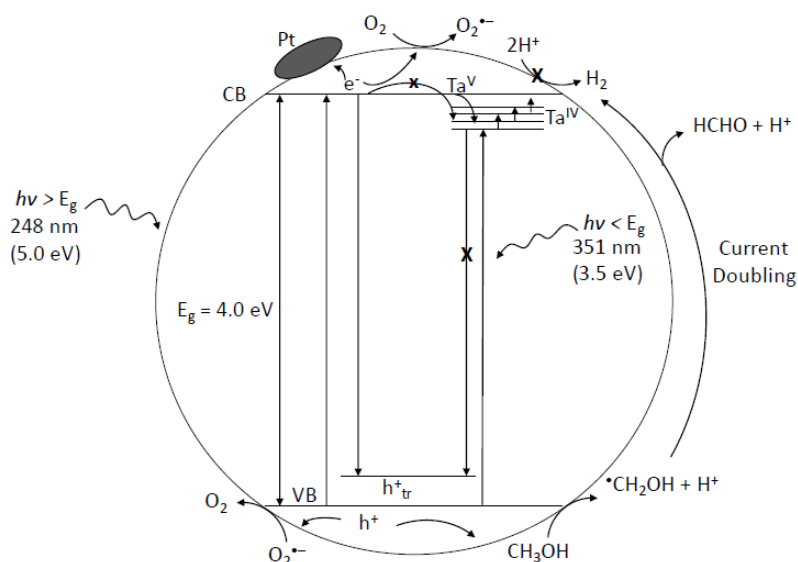


**Figure 7.1:** Scheme of the main proposed processes in this thesis.

If on the contrary, the sample is irradiated with an energy lower than the band gap of the material (351 nm), the electrons will not have enough energy to reach the conduction band and will be deeply trapped in some mid-gap states below the conduction band and become very unreactive. The recombination reactions are represented as well.

Electron paramagnetic resonance (EPR) measurements have been carried out as well and evidence of the formation of  $\text{Ta}^{\text{IV}}$  has been found. Fig. 5.2 shows signals that belong to electrons near the conduction band which could be  $\text{Ta}^{\text{IV}}$  species (electrons in the conduction band are not paramagnetic).

The overall quantum yield has been determined for the hydrogen evolution when the sample was irradiated with a light of 350 nm and was found to be 0.97%.



## 8. Bibliography

1. Dorian, J. P., Franssen, H. T. & Simbeck, D. R. Global challenges in energy. *Energy Policy* **34**, 1984–1991 (2006).
2. Zheng, X. J., Wei, L.F., Zhang, Z.H., Jiang, Q.J., Wei, Y.J., Xie, B. & Wei, M.B. Research on photocatalytic H<sub>2</sub> production from acetic acid solution by Pt/TiO<sub>2</sub> nanoparticles under UV irradiation. *Int. J. Hydrogen Energy* **34**, **22**, 9033–9041 (2009).
3. Crabtree, G. W. & N.S. Lewis. Solar energy conversion. *Phys. Today* 37–42 (2007).
4. Mu, Y., Zheng, X., Yu, H. & Zhu, R. Biological hydrogen production by anaerobic sludge at various temperatures. *Int. J. Hydrogen Energy* **31**, **6**, 780–785 (2006).
5. Maeda, K. Photocatalytic water splitting using semiconductor particles: History and recent developments. *J. Photochem. Photobiol. C Photochem. Rev.* **12**, **4**, 237–268 (2011).
6. Chen, X., Shen, S., Guo, L. & Mao, S. S. Semiconductor-based photocatalytic hydrogen generation. *Chem. Rev.* **110**, **11**, 6503–6570 (2010).
7. Becquerel, A. E. Recherches sur les effets de la radiation chimique de la lumiere solaire au moyen des courants electriques. *Comptes Rendus l'Academie des Sci.* 145–149 (1839).
8. Honda, K. & Fujishima, A. Electrochemical photolysis of water at a semiconductor electrode. *Nature* **238**, 37–38 (1972).
9. Krol, R. Van de & Grätzel, M. *Photoelectrochemical Hydrogen Production*. Springer, Cambridge (Massachusetts) (2012).
10. Bard, A. J. Photoelectrochemistry. **207**, 139–144 (1980).
11. Bard, A. J. Photoelectrochemistry and heterogeneous photocatalysis at semiconductors. *J. Photochem.* 59–75 (1979).
12. Bolton, J. R., Strickler, S. J. & Connolly, J. S. Limiting and realizable efficiencies of solar photolysis of water. *Nature* **316**, 495–500 (1985).
13. Memming, R. *Semiconductor Electrochemistry*. (Wiley VCH Verlag GmbH, 2001).
14. Maeda, K. & Domen, K. New non-oxide photocatalysts designed for overall water splitting under visible light. *J. Phys. Chem. C* **111**, **22**, 7851–7861 (2007).
15. Bard, A. J. Design of Semiconductor Photoelectrochemical Systems for Solar Energy Conversion. *J. Phys. Chem. C* **86**, **2**, 172–177 (1982).
16. Goodeve, C. F. & Kitchener, J. a. Photosensitisation by titanium dioxide. *Trans. Faraday Soc.* **34**, 570 (1938).

17. Kudo, A. & Miseki, Y. Heterogeneous photocatalyst materials for water splitting. *Chem. Soc. Rev.* **38**, 253–278 (2009).
18. Ivanova, I. Photocatalytic water splitting in sodium tantalate suspensions. (Gottfried Wilhelm Leibniz Universität of Hannover, 2014).
19. Meissner, D., Memming, R., Kastening, B. & Bahnemann, D. Fundamental problems of water splitting at cadmium sulfide. *Chem. Phys. Lett.* **127**, **5**, 419–423 (1986).
20. Asahi, R., Morikawa, T., Ohwaki, T., Aoki, K. & Toga, Y. Photocatalyst sensitive to visible light-response. *Science* **295**, 627–627 (2002).
21. Maruska, H. P. & Ghosh, A. K. Transition-metal dopants for extending the response of titanate photoelectrolysis anodes. *Sol. Energy Mater.* **1**, **3-4**, 237–247 (1979).
22. Salvador, P. Analysis of the physical properties of TiO<sub>2</sub>-Be electrodes in the photoassisted oxidation of water. *Sol. Energy Mater.* **6**, **2**, 241–250 (1982).
23. Henrich, V. E. & Cox, P. A. *The surface science of metal oxides*. (Cambridge University Press, 1994).
24. Howe, R. F. & Grätzel, M. EPR study of hydrated anatase under UV irradiation. *J. Phys. Chem.* **91**, **14**, 3906–3909 (1987).
25. Kato, H., Asakura, K. & Kudo, A. Highly efficient water splitting into H<sub>2</sub> and O<sub>2</sub> over lanthanum-doped NaTaO<sub>3</sub> photocatalysts with high crystallinity and surface nanostructure. *J. Am. Chem. Soc.* **125**, **10**, 3082–3089 (2003).
26. Kudo, A., Kato, H. & Nakagawa, S. Water splitting into H<sub>2</sub> and O<sub>2</sub> on new Sr<sub>2</sub>M<sub>2</sub>O<sub>7</sub> (M=Nb and Ta) photocatalysts with layered perovskite structures: Factors affecting the photocatalytic activity. *J. Phys. Chem. B* **104**, **3**, 571–575 (2000).
27. Yamakata, A., Ishibashi, T., Kato, H., Kudo, A. & Onishi, H. Photodynamics of NaTaO<sub>3</sub> catalysts for efficient water splitting. *J. Phys. Chem. B* **107**, **51**, 14383–14387 (2003).
28. Rajeshwar, K. *Fundamentals of Semiconductor Electrochemistry and Photoelectrochemistry*. (Wiley-VCH, 2002)
29. Morrison, S. R. *Electrochemistry at semiconductor and oxidized metal electrodes*. (Plenum Press, 1980).
30. Beranek, R. (Photo)electrochemical methods for the determination of the band edge positions of TiO<sub>2</sub>-based nanomaterials. *Adv. Phys. Chem.* **2011**, 1–20 (2011).
31. Pleskov, Y. V. & Gurevich, Y. Y. *Semiconductor Photoelectrochemistry*. (Plenum, 1986).
32. Smith, R. A. *Semiconductors*. (Cambridge University Press, 1959).

33. Tauc, J., Grigorovic, R. & Vancu, A. Optical properties and electronic structure of amorphous germanium. *Phys. Status Solidi* **15**, 627–637 (1966).
34. Basu, P. K. *Theory of optical processes in semiconductors: bulk and microstructures*. (Clarendon Press, 1997).
35. Gärtner, W. W. Depletion-layer photoeffects in semiconductors. *Phys. Rev.* **116**, 84–87 (1959).
36. Butler, M.A. & Ginley, D.S. Prediction of flatband potentials at semiconductor-electrolyte interfaces from atomic electronegativities. *J. Electrochem. Soc.* **125**, **2**, 228–232 (1978).
37. Nozik, A. J. & Memming, R. Physical chemistry of semiconductor-liquid interfaces. *J. Phys. Chem.* **100**, **31**, 13061–13078 (1996).
38. Bott, A. W. Practical Problems in voltammetry 3: reference electrodes for voltammetry. *Current Separations* **14**, **2**, 64–68 (1995).
39. Linsebigler, A. L., Lu, G. & Yates, J. T. Photocatalysis on TiO<sub>2</sub> surfaces: principles, mechanisms, and selected results. *Chem. Rev.* **95**, **3**, 735–758 (1995).
40. Maeda, K. & Domen, K. *Topics in Current Chemistry*. (Springer, 2011).
41. Litter, M. I. Heterogeneous photocatalysis - Transition metal ions in photocatalytic systems. *Appl. Catal. B: Environmental* **23**, **2-3**, 89–114 (1999).
42. Eastman, D. E. Photoelectric work functions of transition, rare-earth, and noble metals. *Phys. Rev. B* **2**, 1–2 (1970).
43. Chiarello, G. L., Aguirre, M. H. & Selli, E. Hydrogen production by photocatalytic steam reforming of methanol on noble metal-modified TiO<sub>2</sub>. *J. Catal.* **273**, **2**, 182–190 (2010).
44. Kato, H. & Kudo, A. Photocatalytic water splitting into H<sub>2</sub> and O<sub>2</sub> over various tantalate photocatalysts. *Catal. Today* **78**, **1-4**, 561–569 (2003).
45. Fox, M. A. & Dulay, M. T. Heterogeneous photocatalysis. *Chem. Rev.* **93**, **1**, 341–357 (1993).
46. Ranjit, K. T. & Viswanathan, B. Photocatalytic reduction of nitrite and nitrate ions over doped TiO<sub>2</sub> catalysts. *J. Photochem. Photobiol. A Chem.* **107**, **1-3**, 215–220 (1997).
47. Choi, W., Lee, J., Kim, S., Hwang, S. Lee, M.C. & Lee, T.C. Nano Pt particles on TiO<sub>2</sub> and their effects on photocatalytic reactivity. *Journal of Industrial Engineering and Chemistry* **9**, **1**, 96–101 (2003).
48. Hwang, S., Lee, M. C. & Choi, W. Highly enhanced photocatalytic oxidation of CO on titania deposited with Pt nanoparticles: Kinetics and mechanism. *Appl. Catal. B Environ.* **46**, **1**, 49–63 (2003).

49. Hufschmidt, D., Bahnemann, D., Testa, J. J., Emilio, C. a. & Litter, M. I. Enhancement of the photocatalytic activity of various TiO<sub>2</sub> materials by platinisation. *J. Photochem. Photobiol. A Chem.* 148, **1-3**, 223–231 (2002).
50. Tung, R. T. Schottky-Barrier formation at single-crystal metal-semiconductor interfaces. *Phys. Rev. Lett.* **52**, 461–464 (1984).
51. Ohtani, B. Titania Photocatalysis beyond Recombination: A Critical Review. *Catalysts* 3, **4**, 942–953 (2013).
52. Bahnemann, D. W. *Aquatic and surface photochemistry*. (Lewis Publisher, 1994).
53. Bahnemann, D. W. *The handbook of environmental chemistry, environmental photochemistry. Part III* (Springer, 1995).
54. Hoffmann, M. R., Martin, S. T., Choi, W. & Bahnemann, D. W. Environmental applications of semiconductor photocatalysis. *Chem. Rev.* 95, 69–96 (1995).
55. Bahnemann, D., Henglein, A. & Spanhel, L. Detection of the intermediates of colloidal TiO<sub>2</sub>-catalysed photoreactions. *Faraday Discuss. Chem. Soc.* 78, 151–163 (1984).
56. Mohamed, H. H. & Bahnemann, D. W. The role of electron transfer in photocatalysis: Fact and fictions. *Appl. Catal. B Environ.* 128, 91–104 (2012).
57. Duonghong, D., Ramsden, J. & Grätzel, M. Dynamics of interfacial electron transfer processes in colloidal semiconductor systems. *Am. Chem. Soc.* 104, **11**, 2977–2985 (1981).
58. Grätzel, M. & Frank, A. J. Interfacial electro-transfer reactions in colloidal semiconductor dispersions. Kinetic analysis. *J. Phys. Chem.* 86, 15, 2964–2967 (1982).
59. Bahnemann, D., Henglein, A., Lillie, J. & Spanhel, L. Flash photolysis observation of the absorption spectra of trapped positive holes and electrons in colloidal TiO<sub>2</sub>. *J. Phys. Chem.* 88, **4**, 709–711 (1984).
60. Tamaki, Y., Furube, A., Murai, M., Hara, K., Katoh, R. & Tachiya, M. Dynamics of efficient electron-hole separation in TiO<sub>2</sub> nanoparticles revealed by femtosecond transient absorption spectroscopy under the weak-excitation condition. *Phys. Chem. Chem. Phys.* 9, **12**, 1453–1460 (2007).
61. Hagfeldt, A. & Grätzel, M. Light-induced redox reactions in nanocrystalline systems. *Chem. Rev.* 95, **1**, 49–68 (1995).
62. Kamat, P. V. Photochemistry on nonreactive and reactive (semiconductor) surfaces. *Chem. Rev.* 93, **1**, 267–300 (1993).
63. Bahnemann, D. W., Hilgendorff, M. & Memming, R. Charge carrier dynamics at TiO<sub>2</sub> particles: reactivity of free and trapped holes. *J. Phys. Chem. B* 101, **21**, 4265–4275 (1997).



64. Yang, X. & Tamai, N. How fast is interfacial hole transfer? In situ monitoring of carrier dynamics in anatase TiO<sub>2</sub> nanoparticles by femtosecond laser spectroscopy. *Phys. Chem. Chem. Phys.* **3**, 3393–3398 (2001).
65. Mohamed, H. H. & Bahnemann, D. W. The role of electron transfer in photocatalysis: Fact and fictions. *Appl. Catal. B Environ.* **128**, 91–104 (2012).
66. Henderson, M. A surface science perspective on TiO<sub>2</sub> photocatalysis. *Surf. Sci. Rep.* **66**, 6–7, 185–297 (2011).
67. Schneider, J., Matsuoka, M., Takeuchi, M., Zhang, J., Horiuchi, Y., Anpo, M. & Bahnemann, D.W. Understanding TiO<sub>2</sub> photocatalysis: mechanisms and materials. *Chem. Rev.* **114**, **19**, 9919–9986 (2014)
68. Jaeger, C. D. & Bard, A. J. Spin trapping and electron spin resonance detection of radical intermediates in the photodecomposition of water at TiO<sub>2</sub> particulate systems. *J. Phys. Chem.* **83**, **24**, 3146–3152 (1979).
69. Anpo, M., Shima, T. & Kubokawa, Y. ESR and photoluminescence evidence for the photocatalytic formation of hydroxyl radicals on small TiO<sub>2</sub> particles. *Chem. Lett.* **14**, 1799–1802 (1985).
70. Wardmann, P. Reduction potentials of one-electron couples involving free radicals in aqueous solution. *J. Phys. Chem. Ref. Data* **18**, **4**, 1637–1755 (1989).
71. Bredow, T. & Jug, K. SINDOL study of photocatalytic formation and reactions of OH radicals at anatase particles. *J. Phys. Chem.* **99**, **1**, 285–291 (1995).
72. Imanishi, a, Okamura, K. T., Ohashi, N., Nakamura, R. & Nakato, Y. Mechanism of water photooxidation reaction at atomically flat TiO<sub>2</sub> rutile(110) and (100) surfaces: dependence on solution pH. *J. Amer. Chem. Soc.* **129**, **37**, 11569 (2007).
73. Salvador, P. On the nature of photogenerated radical species active in the oxidative degradation of dissolved pollutants with TiO<sub>2</sub> aqueous suspensions: a revision in the light of the electronic structure of adsorbed water. *J. Phys. Chem. C* **111**, **45**, 17038–17043 (2007).
74. Shapovalov, V., Stefanovich, E. V & Truong, T. N. Nature of the excited states of the rutile TiO<sub>2</sub> (110) surface with adsorbed water. *Surf. Sci.* **498**, L103–L108 (2002).
75. Ji, Y. F., Wang, B. & Luo, Y. Location of trapped hole on rutile TiO<sub>2</sub> (110) surface and its role in water oxidation. *J. Phys. Chem. C* **116**, **14**, 7863–7866 (2012).
76. Hug, G. L. *Optical spectra of nonmetallic inorganic transient species in aqueous solution*. (US Dept. of Commerce, Bureau of Standards).
77. Lawless, D., Serpone, N. & Meisel, D. Role of OH radicals and trapped holes in photocatalysis. A pulse radiolysis study. *J. Phys. Chem.* **95**, **13**, 5166–5170 (1991).
78. Zawadzki, P. Absorption spectra of trapped holes in anatase TiO<sub>2</sub>. *J. Phys. Chem. C* **117**, **17**, 8647–8651 (2013).

79. Bredow, T. Jug, K. Theoretical investigation of water adsorption at rutile and anatase surfaces. *Surf. Sci.* 327, **3**, 398–408 (1995).
80. Kowalski, P. M., Camellone, M. F., Nair, N. N., Meyer, B. & Marx, D. Charge localization dynamics induced by oxygen vacancies on the titania TiO<sub>2</sub> (110) surface. *Mater. Sci.* 2, (2010).
81. Di Valentin, C., Pacchioni, G. & Selloni, A. Electronic structure of defect states in hydroxylated and reduced rutile TiO<sub>2</sub> (110) surfaces. *Phys. Rev. Lett.* **97**, (2006).
82. Grätzel, M. *Heterogeneous photochemical electron transfer reactions*. (CRC Press, 1988).
83. Peiró, A. M., Colombo, C., Doyle, G., Nelson, J., Mills, A. & Durrant, J.R. Photochemical reduction of oxygen adsorbed to nanocrystalline TiO<sub>2</sub> films: A transient absorption and oxygen scavenging study of different TiO<sub>2</sub> preparations. *J. Phys. Chem. B* 110, **46**, 23255–23263 (2006).
84. Rothenberger, G., Moser, J., Grätzel, M., Serpone, N. & Sharma, D. K. Charge carrier trapping and recombination dynamics in small semiconductor particles. *J. Am. Chem. Soc.* 107, 26, 8054–8059 (1985).
85. Furube, A., Asahi, T., Masuhara, H., Yamashita, H. & Anpo, M. Direct observation of a picosecond charge separation process in photoexcited platinum-loaded TiO<sub>2</sub> particles by femtosecond diffuse reflectance spectroscopy. *Chem. Phys. Lett.* 336, **5-6**, 424–430 (2001).
86. Anpo, M. & Takeuchi, M. The design and development of highly reactive titanium oxide photocatalysts operating under visible light irradiation. *J. Catal.* 216, **1-2**, 505–516 (2003).
87. Kawai, T. & Sakata, T. Photocatalytic hydrogen production from liquid methanol and water. *J. Chem. Soc. Chem. Commun.* 694–695 (1980).
88. Chen, J., Ollis, D. F., Rulkens, W. I. M. H. & Bruning, H. Photocatalyzed oxidation of alcohols and organochlorides in the presence of native TiO<sub>2</sub> and metallized TiO<sub>2</sub> suspensions. Part I: Photocatalytic activity and pH influence. *Water Research.* 33, **3**, 661–668 (1999).
89. Chen, J., Ollis, D. F., Rulkens, W. H. & Bruning, H. Photocatalyzed oxidation of alcohols and organochlorides in the presence of native TiO<sub>2</sub> and metallized TiO<sub>2</sub> suspensions. Part (II): Photocatalytic mechanisms. *Water Research.* 33, **3**, 669–676 (1999).
90. Jitputti, J., Suzuki, Y. & Yoshikawa, S. Synthesis of TiO<sub>2</sub> nanowires and their photocatalytic activity for hydrogen evolution. *Catal. Commun.* 9, **6**, 1265–1271 (2008).
91. Ekambaram, S. Photoproduction of H<sub>2</sub> and O<sub>2</sub> from water using semiconductors in presence of sacrificial reagent. *J. Alloys Compd.* 448, **1-2**, 238–245 (2008).

92. Rosseler, O., Shankar, M.V., Karkmaz-Le, M.D., Schmidlin, L., Keller, N. & Keller V. Solar light photocatalytic hydrogen production from water over Pt and Au/TiO<sub>2</sub> (anatase/rutile) photocatalysts: Influence of noble metal and porogen promotion. *J. Catal.* 269, **1**, 179–190 (2010).
93. Kandiel, T. a., Dillert, R., Robben, L. & Bahnemann, D. W. Photonic efficiency and mechanism of photocatalytic molecular hydrogen production over platinized titanium dioxide from aqueous methanol solutions. *Catal. Today* 161, **1**, 196–201 (2011).
94. Highfield, Z., Chen, M.H., Nguyen, P.T. & Chen, Z. Mechanistic investigations of photo-driven processes over TiO<sub>2</sub> by in-situ DRIFTS-MS: Part 1-platinization and methanol reforming. *Energy & Environmental Science* 2, **9**, 991-1002 (2009).
95. Wang, C. Y., Pagel, R., Bahnemann, D. W. & Dohrmann, J. K. Quantum yield of formaldehyde formation in the presence of colloidal TiO<sub>2</sub>-based photocatalysts: Effect of intermittent illumination, platinization, and deoxygenation. *J. Phys. Chem. B* 108, **37**, 14082–14092 (2004).
96. Tamaki, Y., Furube, A., Murai, M., Hara, K., Katoh, R. & Tachiya, M. Direct observation of reactive trapped holes in TiO<sub>2</sub> undergoing photocatalytic oxidation of adsorbed alcohols: evaluation of the reaction rates and yields. *J. Am. Chem. Soc.* 128, **2**, 416–417 (2006).
97. Lillie, J., Beck, G. & Henglein, A. Pulse radiolysis and polarography. Halfwave potentials for the oxidation and reduction of short-lived organic radicals at the mercury electrode. *Berichte der Bunsen-Gesellschaft* 458–465 (1971).
98. Memming, R. *Semiconductor electrochemistry*. (Wiley VCH Verlag GmbH, 1994).
99. Hykaway, N., Sears, W. M., Morisaki, H. & Morrison, S. R. Current-doubling reactions in titanium dioxide photoanodes. *J. Phys. Chem.* 90, **25**, 6663–6667 (1986).
100. Nakabayashi, S., Komuro, S., Aoyagi, Y. & Kira, A. Transient grating method applied to electron-transfer dynamics at a semiconductor/liquid interface. *J. Phys. Chem.* 91, **7**, 1696–1698 (1987).
101. Panayotov, D. A., Burrows, S. P. & Morris, J. R. Photooxidation mechanism of methanol on rutile TiO<sub>2</sub> nanoparticles. *J. Phys. Chem. C* 116, **11**, 6623–6635 (2012).
102. Mohamed, H. H., Mendive, C. B., Dillert, R. & Bahnemann, D. W. Kinetic and mechanistic investigations of multielectron transfer reactions induced by stored electrons in TiO<sub>2</sub> nanoparticles: a stopped flow study. *J. Phys. Chem. A* 115, **11**, 2139–2147 (2011).
103. Mohamed, H. H., Dillert, R. & Bahnemann, D. W. *Kinetic and mechanistic investigations of the light induced formation of gold nanoparticles on the surface of TiO<sub>2</sub>*. (Wiley-VCH 2012).

104. Kudo, A. & Kato, H. Effect of lanthanide-doping into NaTaO<sub>3</sub> photocatalysts for efficient water splitting. *Chem. Phys. Lett.* 331, **5-6**, 373–377 (2000).
105. Kato, H. & Kudo, A. Water splitting into H<sub>2</sub> and O<sub>2</sub> on alkali tantalate photocatalysts ATaO<sub>3</sub> (A=Li, Na and K). *J. Phys. Chem. B* 105, **19**, 4285–4292 (2001).
106. Yamakata, A., Ishibashi, T., Kato, H., Kudo, A. & Onishi, H. Photodynamics of NaTaO<sub>3</sub> catalysts for efficient water splitting. *J. Phys. Chem. B* 107, **51**, 14383–14387 (2003).
107. Murphy, D. M. *Electron paramagnetic resonance (EPR) of polycrystalline oxide systems*. (Wiley-VCH, 2009).
108. Brunauer, S., Emmet, P. H. & Teller, E. Adsorption of gases in multimolecular layers. *J. Am. Soc.* 60, **2**, 309–319 (1938).
109. Wang, C. Y., R.Pagel, Bahnemann, D. W. & Dohrmann, J. K. Quantum yield of formaldehyde formation in the presence of colloidal TiO<sub>2</sub>-based photocatalysts: Effect of intermittent illumination, platinization and deoxygenation. *J. Phys. Chem. B* 108, **37**, 14082–14092 (2004).
110. Kirk, a. D. & Namasivayam, C. Errors in ferrioxalate actinometry. *Anal. Chem.* 55, **14**, 2428–2429 (1983).
111. Hatchard, C. G. & Parker, C. a. A new sensitive chemical actinometer. II. potassium ferrioxalate as a standard chemical actinometer. *Proc. R. Soc. A Math. Phys. Eng. Sci.* 235, **12**, 518–536 (1956).
112. Rabek, J. F. *Experimental methods in photochemistry and photophysics. Part 2*. (John Wiley and Sons, 1982).
113. Krishnan, R. R., Vinodkumar, R., Rajan, G., Gopchandran, K. G. & Mahadevan Pillai, V. P. Structural, optical, and morphological properties of laser ablated ZnO doped Ta<sub>2</sub>O<sub>5</sub> films. *Mater. Sci. Eng. B* 174, **1-3**, 150–158 (2010).
114. Dobal, P. S., Katiyar, R. S., Jiang, Y., Guo, R. & Bhalla, A. S. Raman scattering study of a phase transition in tantalum pentoxide. *J. Raman Spectrosc.* 31, **12**, 1061–1065 (2000).
115. Baumanis, C. & Bahnemann, D. W. TiO<sub>2</sub> thin film electrodes: correlation between photocatalytic activity and electrochemical properties. *J. Phys. Chem. C* 112, **48**, 19097–19101 (2008).
116. Schoonman, J. Donor densities in TiO<sub>2</sub> photoelectrodes. *J. Electrochem. Soc.* 128, **5**, 1154 (1981).
117. Macdonald, I. R., Rhydderch, S., Holt, E., Grant, N., Storey, J.M.D. & Howe, R.F. EPR studies of electron and hole trapping in titania photocatalysts. *Catal. Today* 182, **1**, 39–45 (2012).

118. Schneider, J. & Bahnemann, D. Undesired role of sacrificial reagents in photocatalysis. *J. Phys. Chem. Lett.* **4**, 20, 3479–3483 (2013).
119. Binnewies, M. *Allgemeine und Anorganische Chemie*. (Elsevier GmbH, 2004).
120. Lin, W.-H., Cheng, C., Hu, C.-C. & Teng, H. NaTaO<sub>3</sub> photocatalysts of different crystalline structures for water splitting into H<sub>2</sub> and O<sub>2</sub>. *Appl. Phys. Lett.* **89**, 211904 (2006).
121. Kanhere, P., Nisar, J., Tang, Y., Pathak, B., Ahuja, R., Zheng, J. & Zhong, C. Electronic structure, optical properties, and photocatalytic activities of LaFeO<sub>3</sub> – NaTaO<sub>3</sub> solid solution. *J. Phys. Chem. C* **116**, 43, 22767–22773 (2012).
122. Li, Z. H., Chen, G. & Liu, J. W. Electron structure and optical absorption properties of cubic and orthorhombic NaTaO<sub>3</sub> by density functional theory. *Solid State Commun.* **143**, 6-7, 295–299 (2007).
123. Li, Z. H., Chen, G. & Liu, J. W. Electron structure and optical absorption properties of cubic and orthorhombic NaTaO<sub>3</sub> by density functional theory. *Solid State Commun.* **143**, 6-7, 295–299 (2007).
124. Jana, P., Montero, C., Pizarro, P., Coronado, J.M., Serrano, D.P., O'Shea, V.A. Photocatalytic hydrogen production in the water/methanol system using Pt/RE:NaTaO<sub>3</sub> (RE = Y, La, Ce, Yb) catalysts. *Int. J. Hydrogen Energy* **39**, 10, 5283–5290 (2014).
125. Shannon, R. B. Revised effective ionic radii and systematic studies of interatomic distances in halides and chalcogenides. *Acta Crystallography A* **32**, 751–767 (1976).
126. Ito, S., Chen, P., Comte, P., Nazeeruddin, M.K., Liska, P., Péchy, P. & Grätzel, M. Fabrication of screen-printing pastes from TiO<sub>2</sub> powders for dye-sensitized solar cells. *Prog. Photovoltaics Res. Appl.* **15**, 7, (2007).
127. McCann, J.F., Handley, L. J. The photochemical effect at a p-GaP electrode. *Nature* **283**, 843–845 (1980).
128. Salvador, P. Hole diffusion length in n-TiO<sub>2</sub> single crystals and sintered electrodes: Photoelectrochemical determination and comparative analysis. *J. Appl. Phys.* **55**, 2977–2985 (1984).
129. Feng, X., Shankar, K., Paulose, M. & Grimes, C. A. Tantalum-doped titanium dioxide nanowire arrays for dye-sensitized solar cells with high open-circuit voltage. *Angew. Chemie* **48**, 8239–8242 (2009).
130. Cheng, X. F., Leng, W.H., Liu, D.P., Xu, Y.M., Zhang, J.Q. & Cao, C.N. Electrochemical preparation and characterization of surface-fluorinated TiO<sub>2</sub> nanoporous film and its enhanced photoelectrochemical and photocatalytic properties. *J. Phys. Chem. C* **112**, 23, 8725–8734 (2008).

131. Weber, M. F. & Dingnam, M. J. Splitting water with semiconducting photoelectrodes- Efficiency considerations. *Int. J. Hydrogen Energy* 11, **4**, 225–232 (1986).
132. Bolton, J. R., Strickler, J. S. & Connolly, J. S. Limiting and realizable efficiencies of solar photolysis of water. *Nature* 316, 495–500 (1985).
133. Murphy, A. B., Barnes, P.R.F., Randeniya, L.K., Plumb, I.C., Grey, I.E., Horne, M.D. & Glasscock, J.A. Efficiency of solar water splitting using semiconductor electrodes. *Int. J. Hydrogen Energy* 31, 14, 1999–2017 (2006).
134. Hurum, D. C., Agrios, A. G. & Gray, K. A. Explaining the enhanced photocatalytic activity of Degussa P25 mixed-phase TiO<sub>2</sub> using EPR. *J. Phys. Chem. B* 107, **19**, 4545–4549 (2003).
135. Shkrob, I. A. & Sauer, M. C. Hole scavenging and photo-stimulated recombination of electron hole pairs in aqueous TiO<sub>2</sub> nanoparticles. *J. Phys. Chem. B* 108, **33**, 12497–12511 (2004).
136. Berger, T., Sterrer, M., Diwald, O. & Knözinger, E. Light-induced charge separation in anatase TiO<sub>2</sub> particles. *J. Phys. Chem. B* 109, **13**, 6061–6068 (2005).
137. Berger, T., Diwald, O., Knözinger, E., Sterrer, M. & Yates, J. T. UV induced local heating effects in TiO<sub>2</sub> nanocrystals. *Phys. Chem. Chem. Phys.* 8, **15**, 1822–1826 (2006).
138. Green, J., Carter, E. & Murphy, D. M. An EPR investigation of acetonitrile reactivity with superoxide radicals on polycrystalline TiO<sub>2</sub>. *Res. Chem. Intermed.* 35, 145–154 (2009).
139. Rabani, J., Yamashita, K., Ushida, K., Stark, J. & Kira, A. Fundamental reactions in illuminated titanium dioxide nanocrystallite layers studied by pulsed laser. *J. Phys. Chem. B* 102, **10**, 1689–1695 (1998).
140. Serpone, N., Lawless, D., Khairutdinov, R. & Pelizzetti, E. Subnanosecond relaxation dynamics in TiO<sub>2</sub> colloidal sols (Particle sizes R<sub>p</sub>=1.0-13.4nm). Relevance to heterogenous photocatalysis. *J. Phys. Chem.* 99, **45**, 16655–16661 (1995).
141. Colombo, D. P. & Bowman, R. M. Does interfacial charge transfer compete with charge carrier recombination? Afemtosecond diffuse reflectance investigation of TiO<sub>2</sub> nanoparticles. *J. Phys. Chem.* 100, **47**, 18445–18449 (1996).
142. Martin, S. T., Herrmann, H., Choi, W. & Hoffmann, M. R. Time-resolved microwave conductivity. Part 1. TiO<sub>2</sub> photoreactivity and size quantization. *J. Chem. Soc. Faraday Trans.* 90, 3315–3322 (1994).
143. Maruyama, M., Iwase, A., Kato, H., Kudo, A. & Onishi, H. Time-resolved infrared absorption study of NaTaO<sub>3</sub> photocatalysts doped with alkali earth metals. *J. Phys. Chem. C* 113, **31**, 13918–13923 (2009).

144. Machida, M., Yabunaka, J. & Kijima, T. Efficient photocatalytic decomposition of water with the novel layered tantalate  $\text{RbNdTa}_2\text{O}_7$ . *Chem. Commun.* 1939–1940 (1999).
145. Machida, M., Yabunaka, J. & Kijima, T. Synthesis and photocatalytic properties of layered perovskite tantalates,  $\text{RbLnTa}_2\text{O}_7$  (Ln=La, Pr, Nd and Sm). *Chem. Mater.* 12, **3**, 812–817 (2000).
146. Machida, M., Yabunaka, J., Kijima, T. & Matsushima, S. Electronic structure of layered tantalates photocatalysts,  $\text{RbLnTa}_2\text{O}_7$  (Ln=La, Pr, Nd and Sm). *Int. J. Inorg. Mater.* 3, **6**, 545–550 (2001).
147. Machida, M., Murakami, S. & Kijima, T. Photocatalytic property and electronic structure of lanthanide tantalates,  $\text{LnTaO}_4$  (Ln=La, Ce, Pr, Nd and Sm). *J. Phys. Chem. B* 105, **16**, 3289–3294 (2001).
148. Machida, M., Miyazaki, K., Matsushima, S. & Arai, M. Photocatalytic properties of layered perovskite tantalates,  $\text{MLnTa}_2\text{O}_7$  (M=Cs, Rb, Na, and H; Ln = La, Pr, Nd, and Sm). *J. Mater. Chem.* 13, 1433 (2003).
149. Zhang, Z., Wang, C.-C., Zakaria, R. & Ying, J. Y. Role of particle size in nanocrystalline  $\text{TiO}_2$ -based photocatalysts. *J. Phys. Chem. B* 102, **52**, 10871–10878 (1998).
150. Zhang, L., Mohamed, H. H., Dillert, R. & Bahnemann, D. Kinetics and mechanisms of charge transfer processes in photocatalytic systems: A review. *J. Photochem. Photobiol. C Photochem. Rev.* 13, **4**, 263–276 (2012).
151. Ahmed, L. M., Ivanova, I., Hussein, F. H. & Bahnemann, D. W. Role of platinum deposited on  $\text{TiO}_2$  in photocatalytic methanol oxidation and dehydrogenation reactions. *Hindawi* 2014, 1–9 (2014).
152. Bloh, J. Z., Dillert, R. & Bahnemann, D. W. Designing optimal metal-doped photocatalysts: correlation between photocatalytic activity, doping ratio, and particle size. *J. Phys. Chem. C* 116, **48**, 25558–25562 (2012).
153. Fujishima, A., Zhang, X. & Tryk, D.A.  $\text{TiO}_2$  photocatalysis and related surface phenomena. *Surf. Sci. Rep.* 63, **12**, 515–582 (2008).
154. Tarasevich, M. R., Sadkowsk, a & Yeager, E. Oxygen Electrochemistry. *Compr. Treatise Electrochem.* 301 (1983).
155. Zalas, M. & Laniecki, M. Photocatalytic hydrogen generation over lanthanides-doped titania. *Sol. Energy Mater. Sol. Cells* 89, **2-3**, 287–296 (2005).
156. Zielińska, B., Borowiak-Palen, E. & Kalenczuk, R. J. Photocatalytic hydrogen generation over alkaline-earth titanates in the presence of electron donors. *Int. J. Hydrogen Energy* 33, **7**, 1797–1802 (2008).

157. Patsoura, A., Kondarides, D. I. & Verykios, X. E. Photocatalytic degradation of organic pollutants with simultaneous production of hydrogen. *Catal. Today* 124, **3-4**, 94–102 (2007).
158. K.P.C. Vollhardt, N.E. Schore, K. P. *Organische chemie*. (Wiley VCH Verlag GmbH & Co. KGaA, 2005).
159. Gao, R., Safrany, A. & Rabani, J. Fundamental reactions in TiO<sub>2</sub> nanocrystallite aqueous solutions studied by pulse radiolysis. *Radiat. Phys. Chem.* 65, **6**, 599–609 (2002).
160. Rojas, F. S., Ojeda, C. B. & Pavon, J. M. Derivative ultraviolet-visible region absorption spectrophotometry and its analytical applications. *Talanta* 35, 753–761 (1988).
161. Vandenberg, J. M. & Henrich, C. Spectral anomalies produced by the overlapping of absorption bands. *Appl. Spectrosc.* 7, 4, 171–176 (1953).
162. Giese, A. & French, C. The analysis of overlapping spectral absorption bands by derivative spectrophotometry. *Appl. Spectrosc.* 9,2, 78-96 (1955).
163. Liu, H., Ma, H.T., Li, X.Z., Wu, M. & Bao, X.H. The enhancement of TiO<sub>2</sub> photocatalytic activity by hydrogen thermal treatment. *Chem. Phys.* 50, **1**, 39–46 (2003).
164. Thompson, T. L. & Yates, J. T. Surface science studies of the photoactivation of TiO<sub>2</sub>--new photochemical processes. *Chem. Rev.* 106, **10**, 4428–4453 (2006).
165. Ghosh, A. K., Wakim, F. G. & Addiss, R. R. Photoelectronic processes in rutile. *Phys. Rev.* 184, 979–988 (1969).
166. Irie, H., Miura, S., Kamiya, K. & Hashimoto, K. Efficient visible light-sensitive photocatalysts: Grafting Cu(II) ions onto TiO<sub>2</sub> and WO<sub>3</sub> photocatalysts. *Chem. Phys. Lett.* 457, **1-3**, 202–205 (2008).
167. Irie, H., Kamiya, K., Shibamura, T., Miura, S., Tryk, D.A., Yokoyama, T. & Hashimoto, K. Visible light-sensitive Cu(II)-grafted TiO<sub>2</sub> photocatalysts: activities and X-ray absorption fine structure analyses. *J. Phys. Chem. C* 113, **24**, 10761–10766 (2009).
168. Liu, M., Inde, R., Nishikawa, M., Qiu, X., Atarashi, D., Sakai, E., Nosaka, Y., Hashimoto, K. & Miyauchi, M. Enhanced photoactivity with nanocluster-grafted titanium dioxide photocatalysts. *ACS Nano* 8, **7**, 7229–7238 (2014).
169. Liu, M., Qiu, X., Miyauchi, M. & Hashimoto, K. Cu(II) oxide amorphous nanoclusters grafted Ti<sup>3+</sup> self-doped TiO<sub>2</sub>: An efficient visible light photocatalyst. *Chem. Mater.* 23, **23**, 5282–5286 (2011).
170. Liu, M., Qiu, X., Miyauchi, M. & Hashimoto, K. Energy-level matching of Fe(III) ions grafted at surface and doped in bulk for efficient visible-light photocatalysts. *J. Am. Chem. Soc.* 135, **27**, 10064–10072 (2013).



171. Liu, M., Qiu, X., Hashimoto, K. & Miyauchi, M. Cu(II) Nanocluster-grafted, Nb-doped TiO<sub>2</sub> as an efficient visible-light-sensitive photocatalyst based on energy-level matching between surface and bulk states. *J. Mater. Chem. A.* **2**, 13571-13579 (2014).
172. Noguchi, H., Ohtani, B. & Uosaki, K. Effect of excitation wavelength on ultra-fast electron/hole recombination in titanium(IV) oxide powders irradiated by femtosecond laser pulses. *Chem. Lett.* **34**, **5**, 694-695 (2005).
173. Furube, A., Asahi, T., Masuhara, H., Yamashita, H. & Anpo, M. Direct observation of a picosecond charge separation process in photoexcited platinum-loaded TiO<sub>2</sub> particles by femtosecond diffuse reflectance spectroscopy. *Chem. Phys. Lett.* **336**, **5-6**, 424-430 (1999).
174. Laughton, F. R., Marsh, J. H., Barrow, D. A. & Portnoi, E. L. The two-photon absorption semiconductor waveguide autocorrelator. *J. Quantum Electron.* 838-845 (1994).
175. Spector, H. N. Two-photon absorption in semiconducting quantum-well structures. *Phys. Rev. B* **35**, 5876-5879 (1987).
176. Alfassi, Z., Bahnemann, D. W. & Henglein, A. Photochemistry of colloidal metal sulfides. 3 photoelectron emission from CdS and CdS-ZnS Co-colloids. *J. Phys. Chem.* **86**, **24**, 4656-4657 (1982).



## Curriculum vitae

### Personal data

---

Name: María Pilar

Date of birth: 08.02.1985

Surnames: Esteban Mollá

Place of birth: Valencia (Spain)

### Education

---

07/2011-11/2016

PhD Student at the Institute of Technical Chemistry, Leibniz University of Hannover: “Laser Flash Photolysis and EPR Spectroscopy Investigations of Bare and Lanthanum Doped NaTaO<sub>3</sub> Powders”

10/2010-04/2011

Internship at Continental in Hannover: “Gefahrstoffe ESH-Managementsystem”

09/2009-09/2010

Exchange student (Erasmus scholarship) at the Inorganic Chemistry Department, Leibniz University of Hannover: “Synthesis and Characterization of Silica-Based Nanocages”

09/2003-06/2009

Chemistry studies at the Universitat de València (Spain)

1992-2003

Colegio Pureza de María en Ontinyent (Spain)

## Poster presentations:

Esteban, P., Dillert, R., Bahnemann, D.W.

“Laser Flash Photolysis Studies on NaTaO<sub>3</sub>”

NanoDay, Laboratorium für Nano- und Quantenengineering (LNQE), Leibniz Universität Hannover, October 1<sup>st</sup>, 2014, Hannover, Germany.

Esteban, P., Dillert, R., Bahnemann, D.W.

“Photoelectrochemistry and Laser Flash Photolysis Studies on NaTaO<sub>3</sub>”

20<sup>th</sup> International Conference on Conversion and Storage of Solar Energy, 27 July-1<sup>st</sup> August, Berlin, Germany.